University of Cape Town

Doctoral Thesis

Interstellar Medium Properties and Star Formation in Nearby Galaxies

Author:
Roger Ianjamasimanana

Supervisors:
Prof. W. J. G. de Blok
Prof. Thomas H. Jarrett

A thesis submitted in fulfilment of the requirements for the degree of Doctor of Philosophy

in the

Department of Astronomy

May 2014

Plagiarism statement

I know the meaning of plagiarism and declare that all of the work in the document, save for that which is properly acknowledged, is my own.

Acknowledgements

First and foremost, I would like to thank the almighty God, for giving me health, strength, courage and knowledge to finish this thesis. I acknowledge fruitful guidance from my advisor, Professor Erwin de Blok. I am also grateful for Dr. Fabian Walter and Dr. George H. Heald for their useful comments and suggestions. Moreover, I would like to give great thanks to Dr. Adam Leroy for giving us the star formation rate maps of the THINGS galaxies. Other people who contributed to the achievement of this PhD thesis are also gratefully acknowledged. A special thanks also goes to Prof. Thomas H. Jarrett for funding the thesis. I am also grateful to Dr. Elisa Josiane RINDRAHARISAONA for her support and encouragement. A great thanks goes to Faraniaina RASOLOFOSON for proofreading the thesis and to Holifidy RAPANOEL for helping me with the thesis submission process. I acknowledge funding from the National Research Foundation NRF through the South African Research Chair Initiative (SARChI) bursary program. I also acknowledge support from the NRF-NWO exchange program which made my visit to the Netherlands possible. Finally, my most affectionate gratitude goes to my parents and my family members for their support and prayers.

Abstract

Name: Roger IANJAMASIMANANA
Title: Interstellar medium properties and star formation in nearby galaxies
Date: May 2014

We study the properties of the interstellar medium (ISM) of nearby galaxies from The HI Nearby Galaxy Survey (THINGS) by analyzing the shapes of their HI emission velocity profiles. We apply a stacking method to increase the signal-to-noise (S/N) of the profiles and obtain what we call a super profile. We quantify all the relevant systematic effects that could confuse the interpretation of the shapes of the super profiles. We identify a sample of 22 galaxies from THINGS that are mostly free from these effects and analyze their super profile shapes. We derive super profiles from the entire HI disks of galaxies, inside and outside the optical radius r_{25}, as a function of radius, column density, and star formation rate surface density. The super profiles can be described as the sum of a narrow and a broad Gaussian components. We associate the narrow component with the cold HI phase of the ISM and the broad component with the warm HI phase of the ISM. We find that the shapes of the super profiles correlate with star formation indicators such as metallicity, Hα and far-UV–near-UV colors. We also find that the mass fraction of the narrow component tends to be higher inside the optical radius r_{25}. In addition, the velocity dispersions of the narrow and broad components decline exponentially with radius for virtually all the analyzed galaxies. Moreover, the flux ratio or mass ratio of the narrow and broad components, which serves as an estimate of the fraction of HI gas in the cold phase, tends to decrease with radius. Our results also show that regions having higher narrow component fractions usually corresponds to regions of higher HI or total (HI+H_2) gas column density. Furthermore, the velocity dispersions of the broad and narrow components increase with increasing column density and star formation rate surface density. We have also investigated the physical mechanisms that can explain the observed width of the super profiles. These are supernova explosions (SNe), thermal effects from ultra-violet (UV) photons and magnetorotational instability (MRI). We find that SNe can explain the observed width of the super profile within the star forming disk (r_{25}) and our data implies a supernova efficiency between 0.01 and 0.1. In the outer disk, the observed width of the super profiles can be attributed to thermal effects from extragalactic background UV photons. Finally, in most cases, MRI is not sufficient to explain the width of the super profile.

Refereed publications

First-author paper:
Part of this thesis has previously appeared in the following paper:
Ianjamasimanana, R., de Blok, W. J. G., Walter, F., and Heald, G. H. 2012, AJ, 144, 96.

Co-authored paper:
Caldú-Primo, A., Schruba, A., Walter, F., Leroy, A., Sandstrom, K., de Blok, W. J. G., **Ianjamasimanana, R.**, and Mogotsi, K. M. 2013, AJ, 146, 150.

Contents

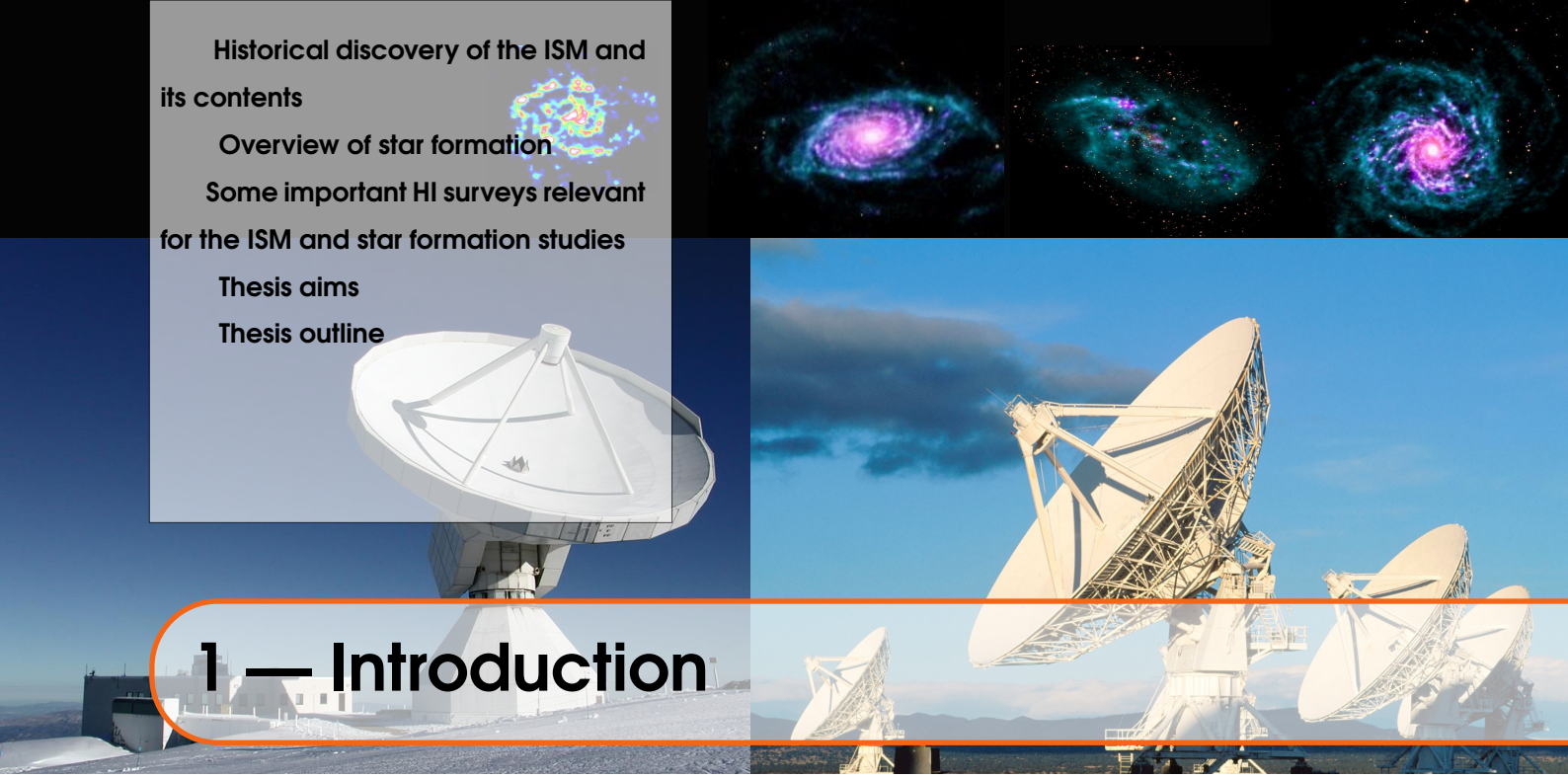

1 — Introduction

We may all have glanced at the night sky filled with utterly brilliant stars, which appear to be tiny points of light to our eyes. Astronomers have been trying their best to understand how these cosmic objects form. There are many reasons why one should be interested in the study of star formation. Basic elements for terrestrial life such as carbon, nitrogen and oxygen were produced in the cores of stars through nuclear fusion reactions. The evolution of galaxies is largely governed by the rate at which they form stars and by their stellar contents. Star formation also has a major impact on the surrounding gas and can regulate the efficiency at which gas is converted to stars. For small galaxies, star formation can easily shape the structure and distribution of their gas content. Star formation involves many different physical and chemical mechanisms, which are not yet fully understood. To shed light on the process of star formation, it is important to look at the properties of the birthplace of stars: the interstellar medium (ISM). In this thesis, we will make use of high-resolution observational data of nearby galaxies to study the connection between the properties of their ISM and star formation.

1.1 Historical discovery of the ISM and its contents

Before giving a general overview of the current understanding of the ISM content, we will begin by giving a short summary of the evolution of our understanding of the ISM. The following historical overview is based on Lecture notes by Dr. Michiel Hogerheijde titled "Overview of the Interstellar Medium", which can be found at `http://www.strw.leidenuniv.nl/~michiel/ismclass.html`. The ISM was once thought to be a vacuum. The great advance towards the discovery that the ISM is not

empty, started from the catalogue of nebulae (originally known as objects that appear as faint patches of light in the sky) by Herschel in 1800, followed later by the pioneering spectroscopic observations of Huggins in 1860s. Huggins reported that some nebulae have stellar-like spectra while others have gaseous-like spectra. This served as an early indication of the presence of gaseous components in the ISM. However, the first conclusive evidence of the existence of matter in the ISM was provided by Hartmann when he discovered narrow lines of singly-ionized calcium in the spectrum of the binary star δ Orionis (Hartmann, 1904). The lines did not show the periodic Doppler shift expected from the orbital motion of stars in a binary system. This led Hartmann to assume that the lines arose from cold absorbing gas which lies between us and the binary star. The existence of the narrow *stationary lines*, as they were called at that time, was confirmed by subsequent observers but the idea of their interstellar origin was not immediately accepted. From a theoretical viewpoint, Eddington (1926), in his effort to answer the question of whether there is *an appreciable quantity of matter* in regions between stars, supported the hypothesis put forward by Hartman and made a further claim that the interstellar hydrogen molecule ought to be abundant in the ISM. Hartmann's suggestion was robustly substantiated by Plaskett and Pearce in the 1930s (e.g. Plaskett and Pearce, 1930) when they compared the radial velocities of the *stationary* lines with those of the *ordinary* stellar lines.

In line with the above observational discoveries, a new type of *stationary* absorption lines was discovered by Heger in 1922. The lines appeared to be broader than stellar atomic lines and showed no shift in wavelength. These lines are nowadays known as diffuse interstellar bands (DIBs) whose origins remain unknown, though there are more than 500 of such lines discovered so far (e.g. McCall and Griffin, 2013). It is generally assumed that they are caused by molecular species such as polycyclic aromatic hydrocarbon cations, linear carbon-chain radicals, fullerenes or excited hydrogen. Thus, the first realization of the existence of matters in the ISM started out from the effects they have on stellar-light. In the next section, we will summarize some important discoveries of the contents of the ISM, with a particular emphasis on the components that are mostly relevant for the current thesis.

Cosmic rays

In 1912, *cosmic rays* are discovered by Viktor Franz Hess. He took an electroscope on a balloon flight and measured the amount of radiations as a function of altitude. He found that there is a considerable increase in the level of radiation from an altitude of about 700 m. This led him to conclude that the radiation was coming from outer-space. Hess's findings were confirmed by Robert Millikan who coined the term "cosmic ray" in 1925. Cosmic rays are very high energy particles with energy of

the order of GeV to EeV. They are thought to be charged particles accelerated by shock waves from supernova explosions or by magnetic fields. Due to their high energy, cosmic rays can easily ionize their surrounding gas and therefore can help regulate the rate of star formation.

Dust

In 1919, Barnard published his catalogue of "Dark markings" on the sky (Barnard, 1919). These were regions in the sky that appeared to be dark in his photographic images. Barnard was certain that most of these dark areas were caused by matter obscuring the light between the stars and the observer. He, however, did not rule out the possibility that they could be starless regions in the sky as first suggested by William Herschel in 1785. The idea that there is obscuring matter in interstellar space was first suggested by Mr. Ranyard in 1894. In the *Knowledge* journal of which he was the editor, he wrote: "The dark vacant areas or channels running north and south, in the neighborhood of [θ Ophiuchi] at the center .... seem to me to be undoubtedly dark structures, or absorbing masses in space, which cut out the light from the nebulous or stellar region behind them". The dark markings of Barnard are known today as dark nebulae, which are clouds of dust and gas blocking or absorbing light from nearby stars. These clouds shine brightly in the infrared spectrum. They are usually the sites of active star formation.

The year 1930 also marks a great step forward to the understanding of the ISM components when Trumpler found evidence of interstellar extinction by comparing the angular diameter distance ($r = D/\theta$) and luminosity distance ($r = \sqrt{(L/4\pi f)}$) of about 100 open clusters. Under the assumption of a constant luminosity L and a constant physical size D, he expected the two distance estimates to be equal on average. Instead, he found the photometric distance to be systematically larger for more distant clusters. He attributed it as a result of a systematic dimming of the light from the clusters. It is now understood that the extinction of starlight is caused by dust grains (Draine, 2003). These are solid particles of submicron size and make up about 1% by mass of the baryonic components of the ISM. Dust grains can absorb, scatter and polarise light passing through them. They also re-radiate the absorbed light in the infrared. Thus, they can protect gas in their vicinity against ionizing radiation from nearby young stars. Dust grains also act as catalysts for the formation of molecules in the ISM. For example, hydrogen molecules, i.e. the raw material for star formation, can be efficiently formed through grain-surface reaction (Cazaux and Spaans, 2004). Thus, dust grains play an important role in star formation processes by protecting and helping the formation of molecular clouds.

Molecules

In 1937–1940, the first interstellar molecules were discovered. These include the diatomic radicals CH and CN (Adams, 1941; McKellar, 1940; Swings and Rosenfeld, 1937) and the positive ion CH^+ (Douglas and Herzberg, 1941). The basic spectroscopic approach for identifying a particular molecular line is by matching the spectrum of a particular molecule obtained in the laboratory with the spectral lines from cosmic objects. Aided by the rapid advance of space-based and ground-based observation techniques starting from the late 1960s, more than a hundred interstellar molecules have been discovered through their electronic, rotational, vibrational or ro-vibrational transitions. These range from a simple diatomic molecules such as CO (carbon monoxide) and H_2 to very complex organic molecules like cyanopolyyne (e.g. $HC_{11}N$ discovered by Bell et al., 1997) and ethyl formate (e.g. C_2H_5OCHO detected by Belloche et al., 2009). Nowadays, the hunt for new interstellar molecules continue including the search for prebiotic molecules to understand the origin of life on Earth and to investigate whether life could exist elsewhere in the Universe.

H_2 is the most abundant molecule in the Universe and constitutes most of the mass of interstellar molecular gas clouds from which stars are formed. Observations indicate a tight connection between the inferred amount of H_2 per unit area and the rate of star formation (e.g. Bigiel et al., 2008). Observations of H_2 thus provide great diagnostics for the properties of molecular gas clouds (dynamical state, amount and spatial distribution), which are crucial for the understanding of star formation processes. H_2 was detected by Carruthers (1970), in the far-ultra violet (FUV) absorption line of the star ξ Persei through rocket observations. The detections were confirmed later by the *Copernicus* Satellite observations (e.g. Spitzer et al. (1973).

Despite the relative importance of H_2 as mentioned previously, direct observations of this molecule are rather difficult. Observations through the allowed electronic transitions of H_2 in the Lyman and Werner bands require space-based instruments and, due to extinction by dust, cannot probe high density regions where most H_2 forms. In addition, H_2 does not have a permanent electric dipole moment and thus no allowed dipole transitions exists. The electric and rotational-vibrational quadrupole transition lines of H_2 are intrinsically weak and occur at the infrared-part of the electromagnetic spectrum (mostly in the near-infrared, NIR) that are difficult to observe with ground-based instruments due to the effects of the Earth's atmosphere. H_2 also has a high excitation temperature (e.g. the 0–0 S(0) transition at 28.18 μm requires an excitation temperature of $\sim$ 500 K). Typical temperature in molecular clouds are usually low ($\sim$ 10 to 50 K) to excite H_2 transitions. Therefore, except in regions

exposed to UV radiations or in shocked regions (where collisional excitations are more frequent; see e.g. Sternberg and Neufeld, 1999), direct observations of H_2 are difficult. CO is the second most abundant molecule in the Universe. It has a permanent dipole electric moment and emits radiation in the millimeter radio spectrum. Hence, observations of CO do not suffer from dust extinction and can probe high-density regions. The excitation temperature of CO is also low (5-15 K) to allow excitations under typical molecular cloud conditions. CO was first discovered in the Orion nebula through its rotational transition at 2.6 mm (CO $J = 1 \rightarrow 0$) by Wilson et al. (1970). So far, this transition and the CO $J = 2 \rightarrow 1$ rotational transition at 1.3 mm has mostly been used to infer the distribution and amount of H_2 in the ISM owing to the difficulty of directly detecting H_2.

The 21 cm line of atomic hydrogen (HI)

Another great advance in the knowledge of the ISM was the discovery of the 21 cm hyperfine line of atomic hydrogen (HI). The existence of this line in space was first predicted by van de Hulst in 1945. The first detection of the line was made by Ewen and Purcell in 1951 at a frequency of 1420.40575 MHz. The line originated from the Milky Way galaxy. This was the first detection of an astronomical line in the radio-frequency band and opened the field of radio astronomy. The detection was later confirmed by Dutch astronomers Muller and Oort (1951) and by Australian astronomers at CSIRO in Sydney. Two years after the discovery of Ewen and Purcell, the 21 cm line was detected in the Magellanic Clouds by Kerr and Hindman (1953). This marks the first detection of the 21 cm line from an extra-galactic object. The basic physics behind the emission of hydrogen line at a wavelength of λ =21 cm is summarized as follows. For this we will refer to Griffiths (2004).

When a particle pass from a higher energy state to a lower energy state, a photon can be emitted with an energy equal to the energy difference between the two states. A hydrogen atom is composed of one proton (positive charge) and one electron (negative charge) in its orbital. The proton and electron both have an intrinsic angular momentum spin $s = \frac{1}{2}$ and therefore, have a magnetic dipole moment. Due to the presence of magnetic fields created by the motion of these charged particles, the electron and the proton can only spin in a direction parallel or anti-parallel to their magnetic dipole moments. Their spin quantum numbers can either be $m_s = -\frac{1}{2}$ (sometimes called *spin-up*, $\uparrow$) or $m_s = +\frac{1}{2}$ (*spin-down,* $\downarrow$). The hydrogen atom can therefore occupy four states in its ground state. These are $\uparrow\uparrow$, $\uparrow\downarrow$, $\downarrow\uparrow$, $\downarrow\downarrow$, where the first arrow in each state represent the direction of the spin of the proton and the second arrow represent that of the electron. The total angular momentum spin has two possible values F = 0 or F = 1 and therefore has two eigenstates. These two states are known as *triplet* and *singlet*. In the triplet

state, the magnetic moments of the electron and proton are pointing in the same direction (parallel) and corresponds to a higher energy level. However, in the singlet state, which corresponds to a lower energy level, the magnetic moments of the two particles are anti-parallel. When an atomic hydrogen is excited into the triplet state (e.g. due to collisions), it will eventually go back to its lowest possible energy level (the singlet state). The energy difference between the F=1 and F=0 state is $\Delta E = 5.88 \times 10^{-6}\ eV$, which corresponds to a frequency ν=1420.4 MHz (λ=21 cm). So the transition from F=1 to F=0 state will result in an emission of a photon at λ=21 cm. This so-called *spin-flip* or *hyperfine* transition is a magnetic dipole transition (forbidden line) and is very rare. The hydrogen atom can stay in the triplet state for 10 million years. Although the transition is rare, hydrogen atoms are very abundant in the Universe, which makes the 21 cm line easily detectable. A schematic representation of the hyperfine transition of atomic hydrogen is shown below.

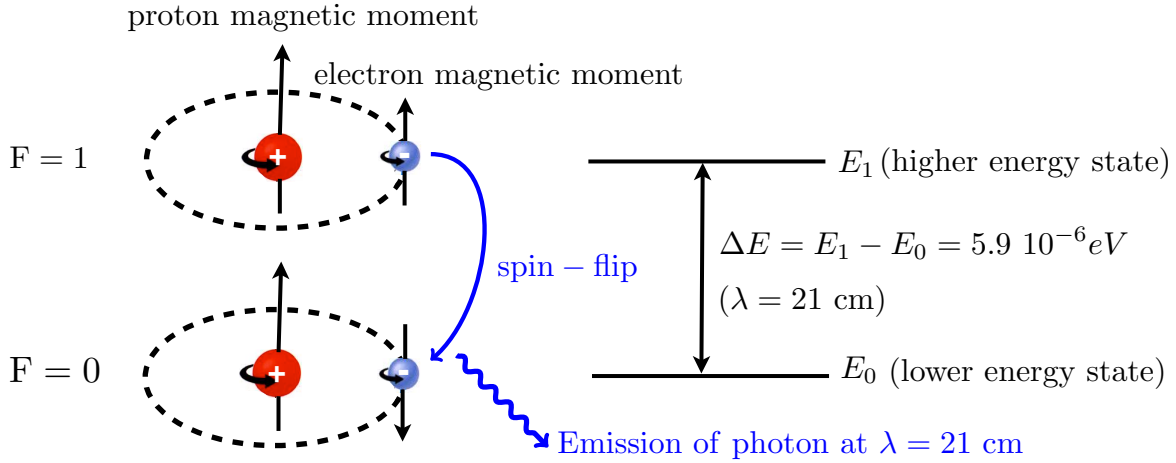

Ionized gas

So far, we have reported the discovery of the neutral atomic and molecular species of the ISM, i.e. the cooler components of the ISM (T $\lesssim 10^4$ K). Evidence of the existence of a hot gas component (T $\gtrsim 10^5$ K) in the ISM comes from the detection of OVI UV absorption line by the Copernicus satellite (Jenkins and Meloy, 1974; Rogerson et al., 1973). Other ionized lines, in support of the existence of hot gas in the ISM, were also detected by the Copernicus satellite and other satellites such as the Far Ultraviolet Spectroscopic Explorer (FUSE) or the Hubble Space Telescope (HST). The discovery of soft X-ray (0.2–2 keV) sources in the 1960s-1970s (e.g. Giacconi et al., 1962) also provided the evidence of hot gas in the ISM. Hot ISM gas can also be traced though radio synchrotron emission.

Magnetic fields

The presence of magnetic fields in the ISM was first realized through the independent discoveries of polarized starlight by Hall and Mikesell (1949) and Hiltner (1949). The existence of the polarized light was interpreted by Davis and Greenstein (1951) as a result of grain alignment by magnetic fields in the Milky Way. Magnetic fields in the ISM were also revealed by the Zeeman splitting of the 21 cm line (Verschuur, 1969), synchrotron emission (Kiepenheuer, 1950) and Faraday rotation (e.g. Weisberg et al., 2004). The role of magnetic fields in star formation is still under intensive investigation. It has been suggested that magnetic fields can lead to inefficient star formation by providing support against collapse for large-scale, low-density gas clouds (Price and Bate, 2009). Magnetic fields were also found to be able to suppress the fragmentation of molecular cloud cores, which encourage the formation of single-star systems and prevent the formation of small stellar clusters (Myers et al., 2013). However, magnetic fields can encourage collapse through the so-called magnetic braking (Seifried et al., 2011).

In summary, the ISM is composed of gas in various forms (ionized, atomic or molecular), dust, radiation, cosmic rays and magnetic fields. The complex interactions between them have a large influence on the gas properties and the rate at which galaxies form stars. In the following, we will give an overview of the connection between gas phases and star formation.

1.2 Overview of star formation

Observational overview

Observations of both nearby and high-redshift galaxies have greatly contributed to the knowledge of star formation, yet the controlling physical processes are not fully understood. The first-generation of stars is believed to form from primordial light elements, mostly made up of hydrogen ($\sim$74% by mass). These primordial stars first produced heavy elements (heavier than beryllium) within their core and expelled them to the ISM. These heavy elements facilitate the formation of the succeeding generation of stars which further enrich the chemical compositions of the ISM through mass loss events. Present-day star formation is believed to be a result of gravitational collapse of dense molecular clouds. Evidence for this comes from observations of the Milky Way galaxy where most star formation happens in the so-called Giant molecular clouds (GMCs) primarily in the molecular form and composed mostly of H_2 gas, having sizes $\sim$10-100 pc and masses of $10^{5-6} M_\odot$.

Star formation and the phases of the ISM

As mentioned in the previous section, gas in the ISM can exist in a molecular, atomic or ionized phase. The atomic phase of the ISM is mostly in the form of HI. Since the early work of Clark (1965), HI has been known to exist in two phases, known as the Cold Neutral Medium (CNM) and the Warm Neutral Medium (WNM). Clark (1965) first suggested that HI must exist in two thermal phases in order to explain the difference in the HI line widths seen in emission and absorption. The narrow absorption spectra were assumed to be caused by a cold HI component of the ISM (the CNM) with a temperature of $\sim$ 100 K, whereas the broad emission spectra arose from a warm component with a temperature as high as 10^4 K (the WNM). The existence of these two components was later confirmed by Radhakrishnan et al. (1972) using interferometric observations of HI emission and absorption spectra towards 35 extragalactic sources situated at intermediate and high Galactic latitude. The CNM and the WNM are known to coexist in pressure equilibrium over a narrow range of pressure (Wolfire et al., 2003). The CNM dominates at high densities and pressures, whereas the WNM prevails at low densities and pressures. The CNM and the WNM have been identified in the Milky Way, in nearby dwarfs, and spiral galaxies by comparing HI seen in emission and absorption as well as from observations of HI emission alone. For HI emission analysis, which is also the topic of this thesis, the identification of these two components can be done by identifying narrow and broad HI velocity profiles, expected from the CNM and the WNM, respectively. In fact, if the velocity profiles are only thermally-broadened, a CNM and WNM with a temperature of 100 K and 800 K, will have a velocity FWHM of $\sim$2.2 and $\sim$ 6.2 km s^{-1}, respectively. However, the observed widths of the HI velocity profiles tend to be always larger than the expected thermal widths of the CNM and the WNM due to other effects (e.g. bulk motion of gas along the line-of-sight, inclination), which broaden velocity profiles.

The connection between the phases of the ISM and star formation has been the subject of a number of investigations. Star formation is found to be more closely linked to the molecular phase of the ISM. Observations of spiral galaxies indicate a strong correlation between the surface density of star formation and the surface density of molecular gas and little-to-no correspondence with the surface density of atomic gas (Bigiel et al., 2008) at least within the star forming disks. However, gravitational-instability analyses reveal correlations between star formation and the transition from atomic to molecular phase (Krumholz et al., 2011) and also from warm atomic (i.e. the WNM) to cold atomic (i.e. the CNM) phase (de Blok and Walter, 2006; Schaye, 2004).

Identification of the CNM and WNM through HI line emission and analyses of their connection with star formation were pioneered by Young and Lo (1996, 1997) and Young et al. (2003). They analyzed the HI emission velocity profiles of seven nearby dwarf galaxies. By fitting these profiles with Gaussian components, they found evidence for a broad component with a dispersion ranging from about 8 to 13 km s^{-1} as well as a much narrower component with a dispersion ranging from 3 to 5 km s^{-1}. These velocity dispersions are larger than the predicted thermal line widths for the CNM and the WNM, showing that other energy sources are also playing a role in broadening the line profiles. Moreover, they found that the narrow component shows a clumpy distribution and tends to be located near star formation regions, whereas the broad component shows a more ubiquitous distribution. Because of the similarities of the observed properties of these two components with those of the CNM and WNM in M 31 and in the Milky Way, they associated the narrow component with the CNM and the broad component with the WNM phases of the ISM. A similar study was made by de Blok and Walter (2006) for the Local Group dwarf galaxy NGC 6822. They also found narrow and broad HI components with mean velocity dispersions of 4 km s^{-1} and 8 km s^{-1}, respectively. Here also, the narrow component is usually located near star forming regions, whereas the broad component tends to be found along every line of sight. Braun (1997) analyzed HI emission of 11 nearby spiral galaxies and found what he called a high brightness filamentary network (HBN) of HI emission which he associated with the CNM and a diffuse low brightness emission which he identified with the WNM. The HBN dominates inside the optical radius r_{25} where it accounts for 60-90 % of the HI emission, whereas the diffuse component dominates outside this radius. By averaging spectra with peak brightness temperature higher than 4σ within annular ellipses in his sample, he found that the combined spectra were characterized by a narrow Gaussian core superposed on broad Lorentzian wings. The width of the narrow line cores allowed Braun (1997) to give an upper limit of 300 K for the HBN. Braun (1997) also found that the kinetic temperature of the HBN increases with increasing radius and interpreted this as a result of the decrease in the mid-plane thermal pressure towards the outer disks.

The CNM as a possible precursor to H_2

As mentioned previously, CO has so far been the commonly used tracer of H_2 for star formation analysis. Although CO is easily detected at mm-wavelengths for normal spiral galaxies, low mass, low metallicity galaxies present a challenge for CO observations due to the metallicity dependence of the CO content. As mentioned in a recent paper by Elmegreen et al. (2013), CO has not yet been

detected in galaxies with metallicity (O/H) lower than 20% of the solar value. Given this observational challenge, alternative ways have been proposed to map the distribution of H_2 gas in low-metallicity galaxies. One of these is through dust measurements and assuming a reasonable gas-to-dust ratio (Sandstrom et al., 2013). Another promising way is to look at possible connections between HI and H_2 as was originally done by Young and Lo (1996, 1997) and Young et al. (2003). They found that the sites of SF tend to be associated with regions of clumpy CNM. This was also confirmed by a similar work by de Blok and Walter (2006). Theoretical work by Schaye (2004) also demonstrated the connection between the CNM and H_2. He found that the transition to the CNM is accompanied by a large increase in the H_2 fraction. Indeed, if the CNM is the precursor of H_2 then the detection of this component would give valuable information about the gas-phase of the ISM that is closely linked to star formation. Moreover, if regions of CNM can be associated with regions containing CO then mapping the former component would be another way to infer the distribution of molecular gas in low-metallicity galaxies (Warren et al., 2012).

Theoretical overview

The following overview is based on a paper by Leroy et al. (2008) and a review by Larson (2003). Theoretically, the conditions for large-scale star formation are often explained in terms of the Toomre Q (Toomre, 1964) parameter. It determines the stability of a differentially rotating fluid against gravitational collapse, and is defined as

$$Q(R) = \frac{\kappa(R) C_s(R)}{\pi G \Sigma}; \tag{1.1}$$

where R is the radius; κ(R) is the epicyclic frequency; $C_s(R)$ is the sound speed; G is the gravitational constant and Σ is the surface density. The sound speed C_s is proportional to the velocity dispersion (a measure of disordered motion) of the particles in the fluid. The term velocity dispersion, often symbolized as σ, will be used many times in this thesis. The fluid will be unstable against gravitational collapse if $Q < 1$. Thus, conditions that favor instability will be a higher surface density, lower velocity dispersion and lower epicyclic frequency. To predict the location of gas clouds susceptible to gravitational collapse in a galaxy, some theoretical models treat the disk of the galaxy as composed of a two-component fluid, consisting of stars and gas (Elmegreen, 1995; Jog, 1996; Jog and Solomon, 1984; Rafikov, 2001; Wang and Silk, 1994; Yang et al., 2007), while others do not include the stellar contributions to the gravitational instability (e.g. de Blok and Walter, 2006; R. C. Kennicutt, 1989; Martin and J. R. C. Kennicutt, 2001; Schaye, 2004). For the former case, Q will be a combination of Q_s

and Q_g, where Q_s denotes the Q parameter for the stellar component and Q_g, that of the gas component. The stellar components can be divided into different subgroups as different stellar populations can have different dynamics and thus different Q parameter (Rafikov, 2001). The gas component can also be subdivided according to their temperature and density. The denser ($n \gtrsim 10$ cm^{-3}) and colder (T<100 K) gas components are usually used in a Q criterion analysis as they have lower velocity dispersions and higher surface densities and therefore they are susceptible to gravitational collapse and to form stars. A study by Schaye (2004), which investigates the stability of disk galaxies embedded in dark halos demonstrated that the presence of the CNM is critical for star formation to occur. Schaye (2004) showed that the transition from the CNM to the WNM, which occurs at a critical surface density and accompanied by the drop in the thermal velocity dispersion (making $Q < 1$), triggers gravitational instability on a range of scale.

The conversion of gas into stars involves many complex physical processes and is still not yet well-understood. It is set by the balance between the inward force of gravity which induces collapse and any outward forces that counteract it. The self-gravity of gas clouds can be enhanced by different triggering mechanisms acting on different scales. On large scales, processes such as galaxy-collisions or interactions dominate. When two galaxies collide or interact, their gas can be strongly compressed. The gas then becomes dense enough to be self-gravitating and eventually form stars. Evidence of this was found for a number of interacting or colliding galaxies which often show higher levels of star formation tracers compared to isolated galaxies (Hummel, 1980; Hummel, 1981; R. C. Kennicutt et al., 1987; Solomon and Sage, 1988). Stephan's Quintet (Stephan, 1877) is among the famous example of interacting galaxies having a starburst region and a number of star formation sites associated with collisions of gas from different galaxies (e.g. Guillard et al., 2012; Xu et al., 1999). On small scales (kpc scales or on the scales of molecular clouds , clumps ($\sim$ 1pc) or cores ($\sim$ 0.1pc)), star formation feedback (e.g. shock waves due to supernovae explosions), ambipolar diffusion (Mouschovias, 1991), expansion of bubbles or shells (Dewangan et al., 2012) are among the proposed triggering mechanisms for star formation. The opposing forces include those from thermal-pressure, turbulence, rotation and magnetic fields and these may also act on different scales (Larson, 2003).

1.3 Some important HI surveys relevant for the ISM and star formation studies

The 21 cm line has successfully been used as a mapping tool for the distribution and kinematics of the atomic hydrogen. It has also been used to infer the matter distribution in galaxies. HI has been mapped through surveys of a pre-selected galaxy sample (targeted survey) or by means of observations of a large volume of space in the sky (blind survey). This thesis will make use of the HI line emission in nearby galaxies to study the interplay between gas and star formation. We will summarize below some of the major past, current and future HI surveys.

Some major targeted HI surveys include the Westerbork HI Survey of Spiral and Irregular Galaxies (WHISP; Swaters et al., 2002; van der Hulst et al., 2001) with a sample of $\sim$ 375 galaxies, The HI Nearby Galaxy Survey (THINGS, Walter et al., 2008), which includes 34 nearby dwarf and spiral galaxies, the Faint Irregular Galaxies GMRT Survey (FIGGS; Begum et al., 2008), which includes a sample of 47 faint ($M_B \sim -13$) irregular dwarf galaxies, the Very Large Array Imaging of Virgo Galaxies in Atomic Gas (VIVA; Chung et al., 2009) with a total sample of 53 galaxies, which include 48 spiral and five irregular galaxies, the Local Irregulars That Trace Luminosity Extremes The HI Nearby Galaxy Survey (LITTLE THINGS; Hunter et al., 2012), which is a survey of 37 dwarf irregular and 4 blue compact dwarf galaxies, the Westerbork Hydrogen Accretion in LOcal GAlaxieS (HALOGAS; Heald et al., 2011) survey, which observed 22 nearby spiral galaxies, the ATLAS^{3D} (Serra et al., 2012) HI survey of 166 nearby early-type galaxies brighter than M_K=-21.5, and the Very Large Array survey of Advanced Camera for Surveys Nearby Galaxy Survey Treasury galaxies (VLA-ANGST; Ott et al., 2012), which mapped HI line emission in 29 nearby dwarf galaxies.

Major blind surveys of HI include the HI Parkes All Sky Survey (HIPASS; Barnes et al., 2001; Meyer et al., 2004; Wong et al., 2006; Zwaan et al., 2004) which detected 5317 HI sources in the southern and northern sky, the Galex Arecibo SDSS survey (GASS; Catinella et al., 2012; Catinella et al., 2010; Catinella et al., 2013) with a sample of $\sim$ 800 galaxies in the redshift range $0.025<z<0.05$, the Arecibo Legacy Fast ALFA (ALFALFA; Giovanelli et al., 2005), an on-going HI survey which aims at covering a volume of $\sim$7000 deg^2 and when complete, will detect more than 30 000 objects out to a redshift of $z\sim0.06$, and the blind survey of the Ursa Major region conducted by Wolfinger et al. (2013), which covers a volume of 480 deg^2.

Future generation of radio telescopes such as the Meer-Karoo Array Telescope (MeerKAT; Booth et

al., 2009), the Australian Square Kilometre Array Pathfinder (ASKAP; Johnston et al., 2008), the single-dish Five-hundred-meter Aperture Spherical radio Telescope (FAST; Nan et al., 2011) and eventually the Square Kilometre Array (SKA) will push the limit of the current radio telescopes capabilities forward in terms of sensitivity, spacial resolution, sky-coverage and redshift range. Examples of future HI surveys are the Widefield ASKAP L-Band Legacy All-sky Blind SurveY (WALLABY), which is expected to detect about 600 000 galaxies out to a redshift of z = 0.26 (Duffy et al., 2012), the Deep Investigation of Neutral Gas Origins (DINGO), which will potentially detect about 100 000 galaxies out to z = 0.43 (Duffy et al., 2012), the MeerKAT HI Observations of Nearby Galactic Objects: Observing Southern Emitters (MHONGOOSE), which will target 30 nearby galaxies to very low column densities, the MeerKAT HI Survey of Fornax, which is a sensitive (column density limit $\sim 10^{18}\mathrm{cm}^{-2}$) survey of the Fornax cluster, the Looking At the Distant Universe with the MeerKAT Array (LADUMA) HI survey, which aims at studying the evolution of cosmic HI gas over time and will detect HI out to z$\sim$ 1.

These surveys play an important role in our understanding of the structure of the ISM and the physical processes that lead to star formation.

1.4 Thesis aims

The goal of this thesis is to study the properties of the ISM of nearby galaxies and their connections with star formation. We aim to identify the CNM and WNM of the ISM in a large sample of nearby galaxies. Some of the open questions we want to address in this thesis include 1) How does the CNM/WNM ratio vary among galaxies? 2) How does the CNM/WNM ratio vary as a function of galactic radius? 3) What are the interplay between star formation and the gas content of galaxies? We will use high-resolution data of nearby galaxies and analyze their kinematics in order to help answer these questions.

1.5 Thesis outline

In Chapter 2, we present the data used in this thesis and our methodology to derive high-signal-to-noise (S/N) HI velocity profile, which we call super profile. In Chapter 3, we discuss possible systematic effects associated with the shapes of the super profile. In that chapter, we also describe the shapes of the super profile derived using the entire HI disk of the galaxies. In Chapter 4, we analyze the shapes

of the super profile as a function of radial positions. Chapter 5 investigates the correlations between the shapes of the super profile, gas column density and star formation. That chapter also investigates the connection between the energy of the ISM and the shapes of the super profile. We summarize our results and discuss the possibilities for future work in Chapter 6.

Data
Methodology and Data selection
Which type of data cube should be used for the current analyses?

2 — Data and Methodology

2.1 Data

We use HI data from The HI Nearby Galaxy Survey (THINGS; Walter et al., 2008). THINGS mapped the HI line emission in a sample of 34 nearby (2-15 Mpc) spiral and dwarf galaxies with the NRAO[1] Very Large Array (VLA). The THINGS sample listed in Table 1 of Walter et al. (2008) and quoted in Table 1 of this thesis spans a range of properties, with total star formation rates ranging from $\sim 10^{-3}$ to 10^{-6} $M_{\odot}$ yr^{-1}, absolute B-luminosities of -11.5 to -21.7 mag, total HI masses of (0.01—14) $\times 10^{9}$ $M_{\odot}$, and metallicities of 7.5 to 9.2 in units of [12 + log(O/H)]. With a total observing time of $\sim$500 hr in the VLA B, C and D arrays, the HI line was mapped at a spatial resolution of $\sim 6''$ (robust weighting) or $\sim 11''$ (natural weighting), respectively. NGC 4214 and M81 dwA were observed at a spectral resolution of 1.3 km s^{-1}. The rest of the galaxies were imaged at a velocity resolution of either 2.6 or 5.2 km s^{-1}. The noise and mapping parameters for the sample are given in Table 2 of Walter et al. (2008). The THINGS data have been made publicly available and can be downloaded from `http://www.mpia.de/THINGS/Data.html`.

We also use CO data from the Heterodyne Receiver Array (HERA; Schuster et al., 2004) CO-Line Extragalactic Survey (HERACLES; first maps presented by Leroy et al., 2009) to infer for the distribution of molecular hydrogen (H_2) gas in our sample and to investigate possible connection between cold HI and H_2 components. HERACLES provides maps of CO $J = 2 \rightarrow 1$ emission for

[1]The National Radio Astronomy Observatory is a facility of the National Science Foundation operated under cooperative agreement by Associated Universities, Inc.

Table 1
Properties of THINGS Sample Galaxies

Galaxy	R.A. (2000.0	Decl. (2000.0)	D	$\log(D_{25})$	m_B	M_B	Incl	P.A.	Metal.	SFR
	hh mm ss.s	dd mm ss.s	Mpc	log(0.'1)	mag	Mag	deg	deg	12+log(O/H)	$M_\odot$ yr^{-1}
1	2	3	4	5	6	7	8	9	10	11
NGC 628*	01 36 41.8	+15 47 00	7.3 [K04]	1.99	9.35	-19.97	7	20 [T08]	8.33 [M06]	1.21 [L06]
NGC 925*	02 27 16.5 [T08]	+33 34 44	9.2 [F01]	2.03	9.77	-20.04	66	287 [dB08]	8.24 [M06]	1.09 [L06]
NGC 1569	04 30 49.0	+64 50 53	2.0 [K04]	1.60	8.33	-18.12	63	112 [M05]	8.16 [S89]	0.06 [K98]
NGC 2366*	07 28 53.4 [O08]	+69 12 51	3.4 [H01]	1.64	10.51	-17.17	64	40 [O08]	7.96 [S89]	...
NGC 2403*	07 36 51.1 [T08]	+65 36 03	3.2 [F01]	2.20	8.11	-19.43	63	124 [dB08]	8.31 [M06]	0.85 [L06]
Ho II*	08 19 05.0	+70 43 12	3.4 [K04]	1.82	10.78	-16.87	41	177 [P92]	7.68 [M06]	0.07 [L06]
M81 DwA*	08 23 56.0	+71 01 45	3.6 [K04]	1.1*	16.26	-11.49	23	49 [B06]	...	...
DDO 53*	08 34 07.2	+66 10 54	3.6 [K04]	0.89	14.31	-13.45	31	132 [B06]	7.77 [M06]	0.008 [L06]
NGC 2841	09 22 02.6 [T08]	+50 58 35	14.1 [M01]	1.84	9.54	-21.21	74	153 [dB08]	8.52 [M06]	0.20 [K03]
NGC 2903*	09 32 10.1 [T08]	+21 30 04	8.9 [D00]	2.07	8.82	-20.93	65	204 [dB08]	9.12 [Z94]	...
Ho I*	09 40 32.3	+71 10 56	3.8 [K04]	1.52	13.12	-14.80	12	50 [O01]	7.54 [M06]	0.006 [L06]
NGC 2976*	09 47 15.3 [T08]	+67 55 00	3.6 [K02]	1.86	9.98	-17.78	65	335 [dB08]	8.30 [M06]	0.10 [L06]
NGC 3031	09 55 33.1 [T08]	+69 03 55	3.6 [F01]	2.33	7.07	-20.73	59	330 [dB08]	8.41 [M06]	1.06 [L06]
NGC 3077	10 03 19.1	+68 44 02	3.8 [K04]	1.73	10.16	-17.75	46	45	8.64 [S94]	0.09 [K98]
M81 DwB	10 05 30.6	+70 21 52	5.3 [K04]	1.05	14.39	-14.23	44	321	7.85 [M06]	0.005 [L06]
NGC 3184*	10 18 17.0	+41 25 28	11.1 [L02]	1.87	10.31	-19.92	16	179 [T08]	8.48 [M06]	1.43 [L06]
NGC 3198*	10 19 55.0 [T08]	+45 32 59	13.8 [F01]	1.81	9.95	-20.75	72	215 [dB08]	8.32 [M06]	0.85 [K03]
IC 2574*	10 28 27.7 [O08]	+68 24 59	4.0 [K02]	2.11	9.91	-18.11	53	56 [O08]	7.94 [M06]	0.12 [L06]
NGC 3351*	10 43 57.7	+11 42 14	10.1 [K04]	1.86	10.13	-19.88	41	192 [T08]	8.60 [M06]	0.71 [L06]
NGC 3521	11 05 48.6 [T08]	-00 02 09	10.7 [vflow]	1.92	9.21	-20.94	73	340 [dB08]	8.36 [M06]	3.34 [L06]
NGC 3621*	11 18 16.5 [T08]	-32 48 51	6.6 [F01]	1.99	9.06	-20.05	65	345 [dB08]	8.24 [M06]	2.09 [L06]
NGC 3627	11 20 15.0 [T08]	+12 59 30	9.3 [F01]	2.01	9.09	-20.74	62	173 [dB08]	8.43 [M06]	2.44 [L06]
NGC 4214*	12 15 39.2	+36 19 37	2.9 [K04]	1.83	9.91	-17.43	44	65	8.34 [S89]	0.05 [K98]
NGC 4449	12 28 11.9	+44 05 40	4.2 [K04]	1.67	8.98	-19.14	60	230 [H98]	8.32 [S89]	...
NGC 4736*	12 50 53.0 [T08]	+41 07 13	4.7 [K04]	1.89	8.54	-19.80	41	296 [dB08]	8.31 [M06]	0.43 [L06]
DDO 154*	12 54 05.9 [T08]	+27 09 10	4.3 [K04]	1.29	13.94	-14.23	66	230 [dB08]	7.54 [M06]	0.004 [L06]
NGC 4826	12 56 43.6 [T08]	+21 41 00	7.5 [K04]	2.02	8.74	-20.63	65	121 [dB08]	8.59 [M06]	0.82 [L06]
NGC 5055*	13 15 49.2 [T08]	+42 01 45	10.1 [vflow]	2.07	8.90	-21.12	59	102 [dB08]	8.42 [M06]	2.42 [L06]
NGC 5194	13 29 52.7	+47 11 43	8.0 [K04]	1.89	8.48	-21.04	42	172 [T08]	8.54 [M06]	6.05 [L06]
NGC 5236*	13 37 00.9	-29 51 57	4.5 [K04]	2.19	7.48	-20.77	24	225 [T93]	9.16 [Z94]	2.52 [K98]
NGC 5457	14 03 12.6	+54 20 57	7.4 [K04]	2.38	8.29	-21.05	18	39 [B81]	8.52 [Z94]	2.49 [K98]
NGC 6946*	20 34 52.2 [T08]	+60 09 14	5.9 [K04]	2.06	8.24	-20.61	33	243 [dB08]	8.40 [M06]	4.76 [L06]
NGC 7331	22 37 04.1 [T08]	+34 24 57	14.7 [F01]	1.96	9.17	-21.67	76	168 [dB08]	8.36 [M06]	4.20 [K03]
NGC 7793*	23 57 49.7 [T08]	-32 35 28	3.9 [K04]	2.02	9.17	-18.79	50	290 [dB08]	8.22 [M06]	0.51 [L06]

Note. — Column 1: galaxy name; galaxies with the asterisk symbols represent our selected subsample which is discussed in Section 3.2 of Chapter 3. Column 2/3: Coordinates in J2000.0. No entry: coordinates taken from NED; T08: Trachternach et al. 2008; Column 4: distances in Mpc. vflow: distances calculated from NED using Hubble flow distances (corrected for Virgo infall); dB08: de Blok et al. 2008, O08: Oh et al. 2008 K02: Karachentsev et al. 2002, K04: Karachentsev et al. 2004, H01: Hunter et al. 2001, F01: Freedman et al. 2001, L02: Leonard et al. 2002, M01: Macri et al. 2001, D00: Drozdovsky & Karachentsev 2000; Column 5: optical size (taken from LEDA; LEDA.UNIV-LYON.FR); K04: Karachentsev et al. 2004; Note: Holmberg diameter is given for M 81 dwA; Column 6: apparent blue magnitude, corrected for Galactic foreground extinction and extinction internal to the galaxy from LEDA; B06: Begum et al. 2006; Column 8: absolute B magnitude derived from Columns 6 and 4; Column 8/9: Inclination and position angle; No entry: taken from LEDA; dB08: de Blok et al. 2008, B06: Begum et al. 2006, O01: Ott et al. 2001, P92: Puche et al. 1992, O08: Oh et al. 2008, M05: Muhle et al. 2005, T08: Tamburro et al. 2008, H98: Hunter et al. 1998, T93: Tilanus & Allen 1993, B81: Bosma 1981; Column 10: metallicities. M06: Moustakas 2006, S89: Skillman et al. 1989, Z94: Zaritsky et al. 1994, S94: Storchi-Bergmann et al. 1994; Column 11: Star formation rates derived from fluxes published in the literature and corrected for the adopted distances: L06: Lee 2006, K98: Kennicutt 1998, K03: Kennicutt et al. 2003.

48 galaxies, of which 18 overlap with the THINGS sample. HERACLES observations have an angular resolution of 13″ and 2.6 km s^{-1} velocity resolution using observations with the Institut de Radioastronomie Millimiétrique (IRAM) 30 m telescope. The CO-detected galaxies have metallicities ranging from 8.25 to 9.12 in units of [12 + log(O/H)]. By using a stacking technique similar to what we apply in this thesis, HERACLES can reach a one-sigma sensitivity limit of ∼1 to 2 $M_{\odot}pc^{-2}$ and can trace CO out to 1.5 times the optical radius, r_{25}, for spirals and $3r_{25}$ for dwarfs (Schruba et al., 2012). HERACLES is a complementary survey of the THINGS, the Spitzer Infrared Nearby Galaxies Survey (SINGS; R. C Jr. Kennicutt et al., 2003), the Galaxy Evolution Explorer Nearby Galaxies Survey (GALEX NGS; Gil de Paz et al., 2007), the *Spitzer* Local Volume Legacy (LVL; Dale et al., 2009) survey so that multi-wavelength analyses are possible for a large sample of nearby galaxies to allow a more complete view of the ISM. HERACLES data can be obtained from `http://www.cv.nrao.edu/~aleroy/heracles_data/`.

To trace the distribution of star formation in our sample, we use calibrated star formation rate (SFR) surface density, Σ_{SFR}, maps derived by Leroy et al. (2008). The SFR maps were constructed from the GALEX Far-Ultraviolet and the SINGS 24μm maps, adopting the FUV-to-SFR calibration by Salim et al. (2007) and the mid-infrared-to-SFR calibration by Calzetti et al. (2007). The FUV and 24μm maps were converted to Σ_{SFR} maps using the formula:

$$\Sigma_{SFR}[M_{\odot}yr^{-1}kpc^{-2}] = (8.1 \times 10^{-2}\, I_{FUV} + 3.2^{1.2}_{0.7} \times 10^{-3}\, I_{24}) \times \cos(i), \quad (2.1)$$

where I_{FUV} and I_{24} are the intensity of the FUV and 24μm emissions in units of MJy $ster^{-1}$, respectively and i is the inclination of the galaxy. FUV (6 eV $< h\nu <$ 13.6 eV) radiation predominantly comes from hot stars of spectral type O and B in regions unobscured by dust and traces star formation on timescales of ∼100 Myr. The 24μm emission is star light re-radiated by small dust grains and traces star formation in dusty environments on timescales of ∼ 10 Myr. Leroy et al. (2008) adopted a working resolution of ∼ 5″ for the Σ_{SFR} maps, which approximately matches that of the THINGS HI data. The Σ_{SFR} maps have a sensitivity limit of $\Sigma_{SFR} = 10^{-4}\, M_{\odot}yr^{-1}kpc^{-2}$ and we only consider pixels above this value in our analysis.

2.2 Methodology and Data selection

2.2.1 Methodology

Introduction

Interferometric and single-dish radio observations of gas in galaxies are usually represented in three-dimensional (3D) cubes, having two spatial axis (right ascension and declination) and one frequency or velocity axis. These 3D cubes are usually called data cubes. Each pixel in RA and DEC in a data cube represents the spectral line or velocity profile of the observed gas, which is Doppler-shifted by the motions of the gas along the line-of-sight. The velocity profiles carry information about the amount, distribution and kinematics of the emitting gas. The work described in this chapter is an extension of my MSc. thesis, which is a pilot study on the analysis of the shapes of the HI velocity profiles of the THINGS galaxies. We also refer to Ianjamasimanana et al. (2012) for an extensive description of that work.

Profile stacking and decomposition

To analyze the shapes of the HI velocity profiles, we apply a stacking technique similar to the one commonly-used for high-redshift HI observations (e.g., Fabello et al., 2011). This technique can be used when the signal-to-noise (S/N) of the individual velocity profiles in a data cube is not high enough (as is the case for typical HI observations) to allow a pixel-by-pixel analysis of the profiles. The stacking technique makes use of a velocity field to shift each spectrum to the same reference velocity and then sums them in order to obtain high S/N spectra, which we call super profiles. We use a hermite h_3 velocity field to do the stacking. The advantage of using this type of velocity field is that it takes into account the asymmetry in the velocity profiles and thus gives a more robust estimate of the radial velocity of the peak of the profile (de Blok et al., 2008). The task SHUFFLE implemented in the Groningen Image processing System (GIPSY; van der Hulst et al., 1992) has been used to shift and sum the profiles in a data cube to obtain the super profiles. While doing the stacking, only individual profiles with peak fluxes higher than 3 times the rms noise level in the data cubes are used. This ensures that we are dealing with real signals rather than noise spikes. We have carried out a test to see if applying a higher S/N cut-off would give a more accurate super profile shape and found that the 3 times rms noise cut-off was a reasonable choice. The details of this test can be found in Appendix A of the thesis.

Following Young and Lo (1996, 1997) and de Blok and Walter (2006), we fit the super profiles

with single Gaussian and double Gaussian components. The Gaussian decompositions will allow the identification of narrow HI profiles, expected from the CNM and broad HI profiles, expected from the WNM. All parameters (dispersion, central velocity, amplitude, constant background term) are left free in the fits. The uncertainties in the data points of each super profiles are defined as

$$\sigma = \sigma_{ch.map} \times \sqrt{N_{prof}/N_{prof,beam}}, \tag{2.2}$$

where $\sigma_{ch.map}$ is the rms noise level in one channel map, N_{prof} is the number of stacked profiles at a certain velocity V, and $N_{prof,beam}$ is the number of profiles in one resolution element (i.e., the number of pixels or profiles per beam). The inverse square of these uncertainties is used as the weight during the fitting. Note that in Equation 2.2, we assume that the noise is uniform throughout each data cube. Though strictly speaking incorrect (due to the primary beam correction), this is a reasonable assumption as most of the galaxies only occupy the inner quarter or so of the area of the primary beam. The primary beam correction factors are therefore on average small.

Relevant parameters

Here we present the parameters we use throughout the thesis to characterize the shapes of the HI velocity profiles. As explained before, we fit the super profiles with a single and a double Gaussian functions. The quality of each fitting function was already assessed during the MSc thesis and is also described in Ianjamasimanana et al. (2012). In summary, based on a χ^2 analysis, the double Gaussian fit is approximately an order of magnitude better (in terms of size of residuals) than the single Gaussian fit. We have also tried three-component Gaussian fits but this did not noticeably improve the quality of the fits. The amplitude of the residuals in Figure 1 and the reduced χ^2 comparison in Figure 2 convincingly show that the super profiles are optimally described by the sum of a narrow and a broad Gaussian components. We will present the results from a single Gaussian fit to facilitate a direct comparison with previous analysis of HI velocity profiles which did not quantify the presence of multiple components of the HI gas. The single and double Gaussian functions are defined as

$$f_{1G}(v) = a_{1G} \exp\left[-0.5\left(\frac{v-\mu_{1G}}{\sigma_{1G}}\right)^2\right] + B, \tag{2.3}$$

$$f_{2G}(v) = a_n \exp\left[-0.5\left(\frac{v-\mu_n}{\sigma_n}\right)^2\right] + a_b \exp\left[-0.5\left(\frac{v-\mu_b}{\sigma_b}\right)^2\right] + B, \tag{2.4}$$

where a_{1G}, μ_{1G}, and σ_{1G} represent the fitted amplitude, the mean, and the velocity dispersion from the single Gaussian fit, respectively. For the double Gaussian fit, A_n, μ_n, and σ_n denote the amplitude,

the mean and the velocity dispersion of the narrow component, respectively. Similarly, a_b, μ_b, and σ_b represent the fitted amplitude, the mean and the velocity dispersion of the broad component, respectively. The term B represents the constant background parameter. We will use the fitted dispersion as a measure of the random motion of the HI gas (Tamburro et al., 2009). A proper measure of the gas velocity dispersion is crucial to understand the balance between gravity and the forces supporting the gas to prevent collapse. In an ideal case, it is a direct tracer of the gas kinetic temperature. In addition, it can also be used to study the shapes of dark matter halos (Olling, 1995). The line strengths or the fitted areas of the narrow and broad component profiles are defined as

$$A_n = a_n \sigma_n \sqrt{\pi}\sqrt{2}, \tag{2.5}$$

$$A_b = a_b \sigma_b \sqrt{\pi}\sqrt{2}. \tag{2.6}$$

The quantities A_n and A_b are the measure of the integrated flux of the narrow and broad components. We will use the ratio A_n/A_b as a measure of the relative amount (in terms of mass) of the narrow component with respect to the broad component. If the narrow and the broad components can be attributed to the CNM and the WNM then the A_n/A_b ratio can be used as an estimate of the mass ratio between the CNM and the WNM.

Examples of the super profiles for three galaxies are shown in Figure 1.

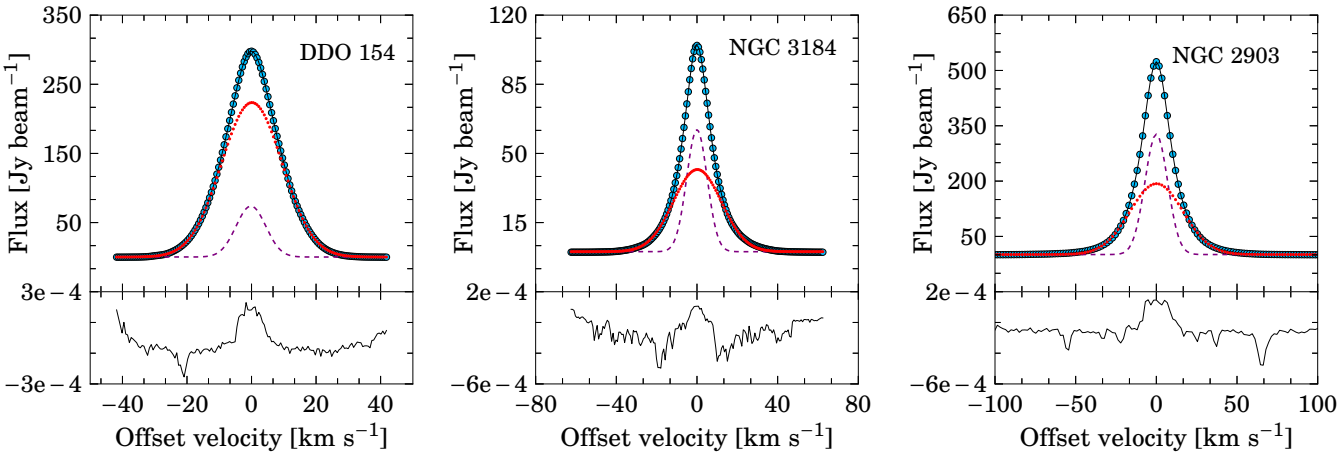

Figure 1: Example of the super profiles for three galaxies from THINGS. The bottom panel of each plot show the residuals from the fits. Filled circles indicate the data. The solid lines represent the results from the double Gaussian fitting. The dashed and the dotted lines represent the narrow and broad components required in the double Gaussian fitting.

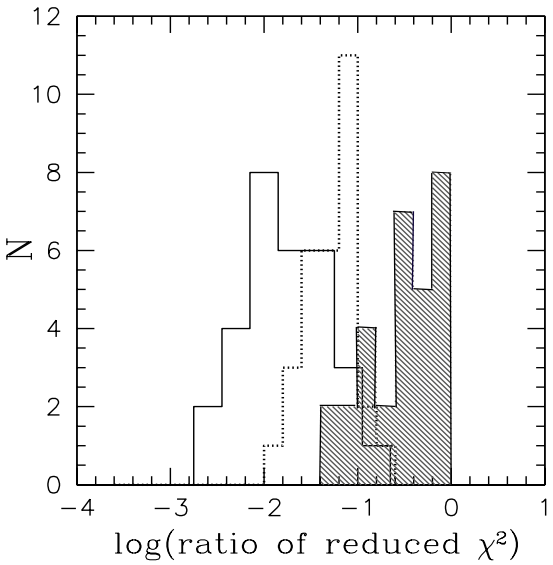

Figure 2: *Solid line histogram:* ratio of the reduced χ^2 from the triple and single Gaussian fits (χ^2_{3G}/χ^2_{1G}). *Dotted line histogram:* ratio of the reduced χ^2 from the double and single Gaussian fits (χ^2_{2G}/χ^2_{1G}). *Hatched histogram:* ratio of the reduced χ^2 from the triple and double Gaussian fits (χ^2_{3G}/χ^2_{2G}).

2.2.2 Data selection

This section demonstrates our choice of the natural-weighted residual-scaled data cube for the current analysis. THINGS provides two types of data cubes using two widely-used weighting schemes: robust weighting and natural weighting. The robust and natural cubes are each further available as residual-scaled and non-residual scaled versions. In the following, we will refer to the natural-weighted non-residual scaled cubes as NA, natural-weighted residual-scaled cube as NA-res, the robust-weighted non-residual scaled cubes as RO, and the robust-weighted residual-scaled cubes as RO-res. The choice of cube to use depends on the type of science to be carried out. The natural-weighted cubes offer the best surface brightness sensitivity but at the cost of a coarser beam size. The robust-weighted cubes give a better spatial resolution but at the expense of a decreased sensitivity. Residual scaling is aimed at obtaining correct flux densities by scaling the residual map, obtained after substracting of deconvolved components, by the ratio of the CLEAN beam to dirty beam area (Walter et al., 2008). This scaling must be applied as the restored image from a standard CLEAN algorithm implemented in radio astronomical data reduction software consists of the sum of a residual map in units of Jy per dirty beam area and a "CLEAN" component map in units of Jy per CLEAN beam area. As explained in

Rich et al. (2008), the dirty beam is usually more extended than the CLEAN beam and using the latter to determine the flux of the residuals will result in an overestimate of that flux. Therefore, a correction factor must be applied to get an accurate estimate of the flux density. However, after the scaling, the original noise properties are no longer preserved. Here we will address which type of cube best suits our analyses.

Robust-weighted data cubes vs natural-weighted data cubes

Here we compare super profile parameters derived from the natural and robust THINGS data cubes. In Figures 3, and 4, we present a comparison of the super profile parameters obtained from the robust and natural cubes. The average velocity dispersion values from the natural cubes are roughly 7% and 13% higher than those from the robust cubes for the narrow and broad components, respectively. The A_n/A_b ratio, however, only scatters around the line of equality. In Figure 4, we compare the parameters from the NA-res and RO-res cubes. As clearly seen in Figure 4, the parameters from the two cubes are very similar. We conclude that the robust and natural weighting schemes give similar super profile parameter values in the residual-scaled case, but values differ slightly for the non-residual scaled cubes.

Non-residual vs residual-scaled cubes

Here we investigate whether residual scaling, as described earlier, has an impact on the shapes of the profiles. In Figure 5, we compare super profile parameters from the NA-res and NA cubes. The narrow component velocity dispersion values from both cubes are similar. Their mean values agree within $\sim$12%. However, for the broad component, there is a systematic difference between the derived velocity dispersion values from the two cubes. The NA cubes tend to give higher σ_b value compared to the NA-res cubes. The difference is larger for higher σ_b value. The mean σ_b value from the NA cube is $\sim$27% higher than that from the NA-res cube. As a result, the σ_n/σ_b values from the NA cube are smaller. In terms of the A_n/A_b ratio, the values derived from the two cubes are similar. In Figure 6, we compare parameters from the RO-res and RO cubes. We again find similar σ_n and A_n/A_b ratio values. The mean σ_b values from the RO-res and RO differ by 16%, this is much lower than the difference found for the natural-weighted cubes. Thus, for the broad components, the effects of the residual-scaling are more important for the natural than for the robust cubes.

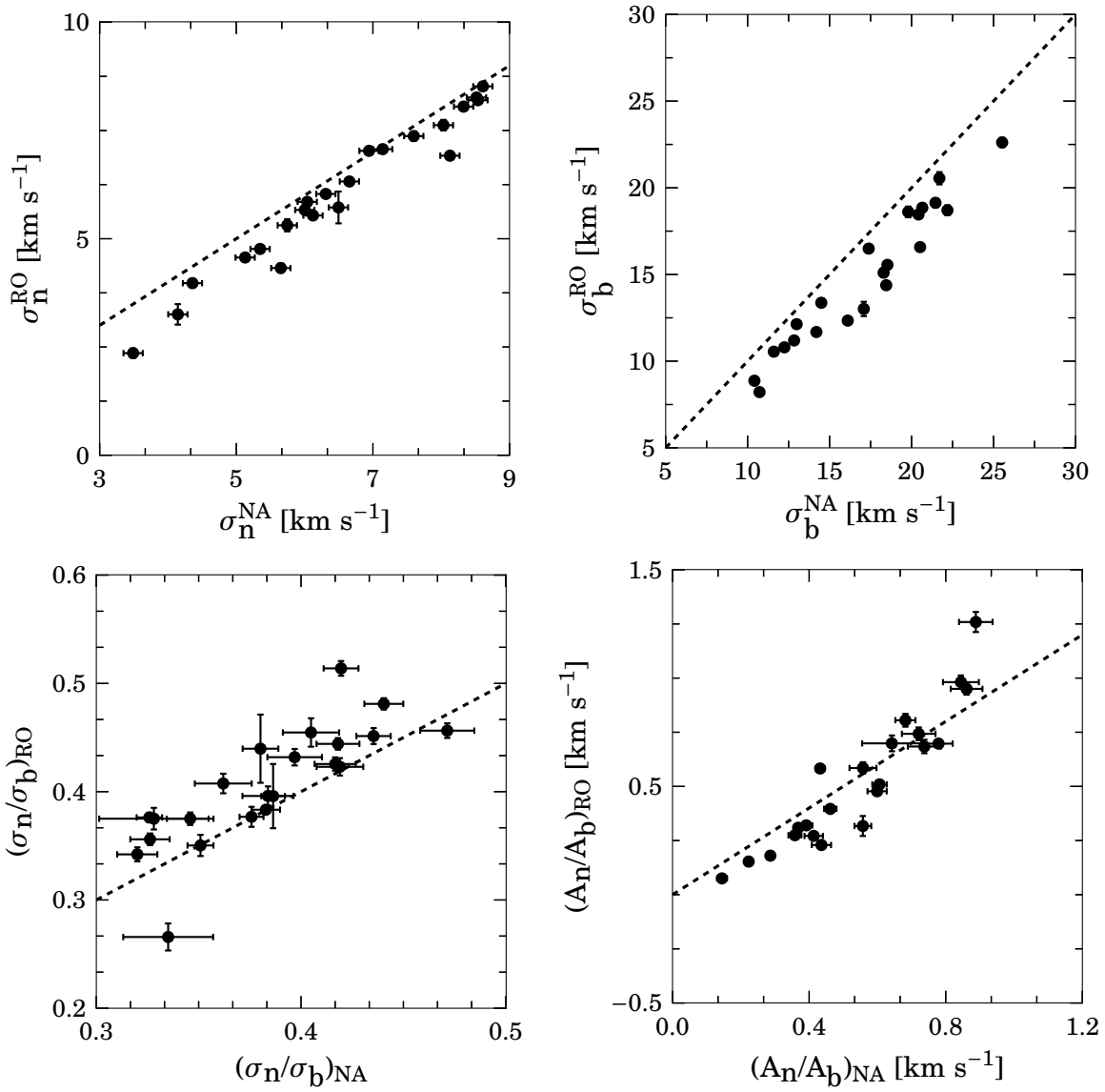

Figure 3: Comparison of super profile parameters from the NA and RO data cubes.

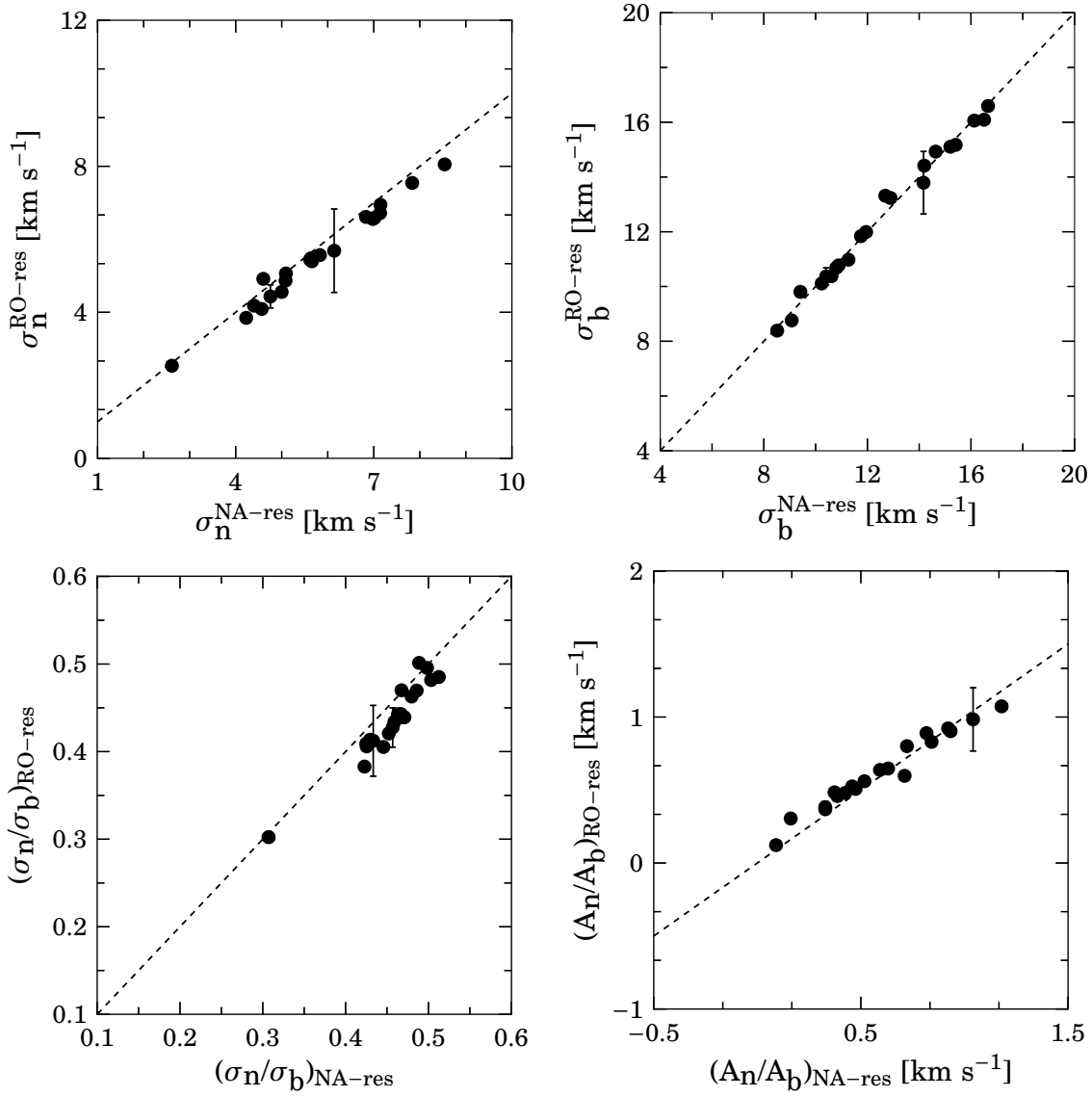

Figure 4: Comparison of super profile parameters from NA-res and RO-res data cubes.

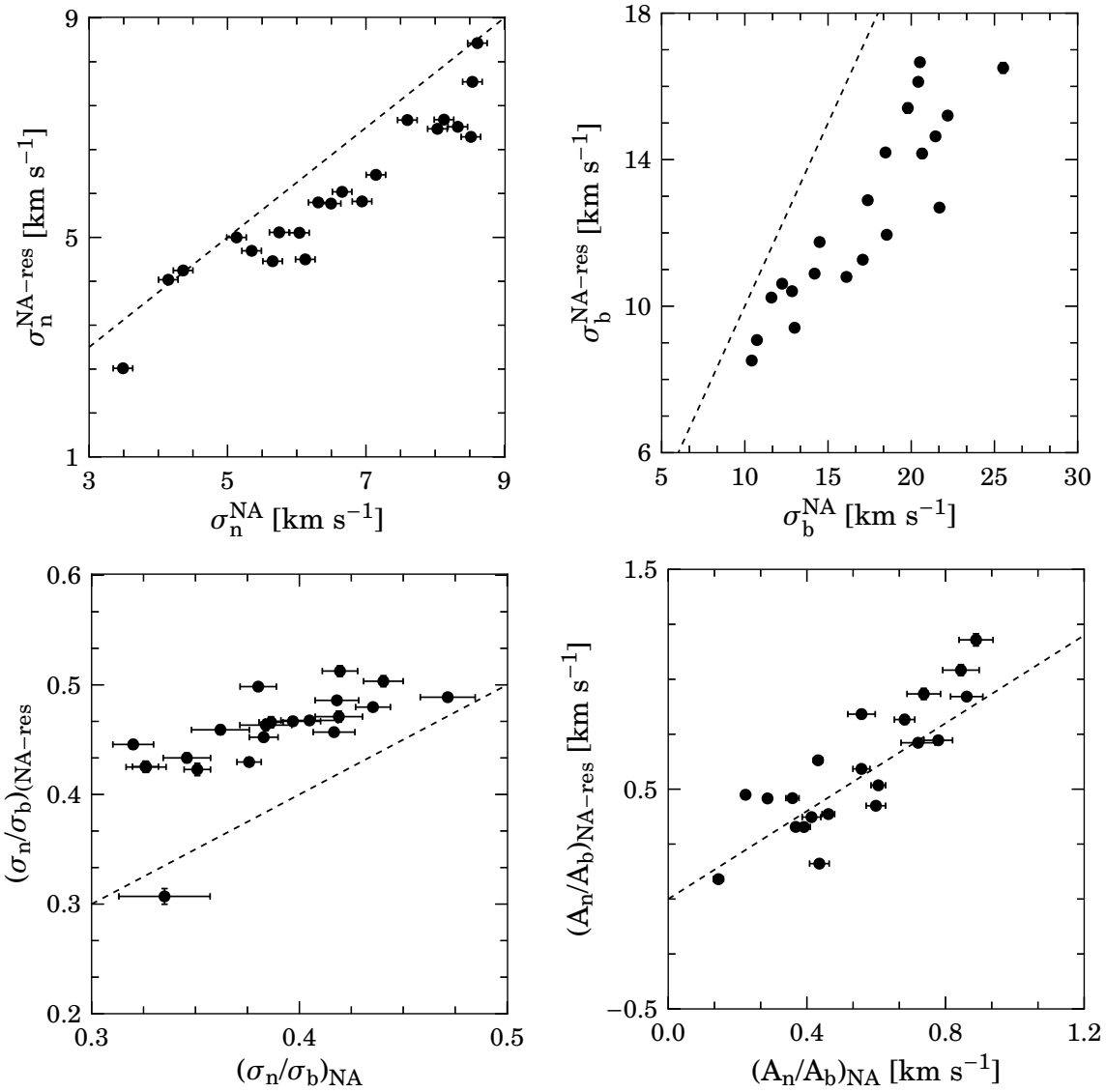

Figure 5: Super profile parameters from the NA-res and the NA data cubes.

2.3 Which type of data cube should be used for the current analyses?

In the previous section, we have shown that though the robust weighting scheme tends to give smaller velocity dispersion values compared to that of the natural one, the mean difference is only of the order of 10%. The difference becomes insignificant when the two cubes are both residual-scaled. Thus in the following, we will only use the natural-weighted data cubes, unless stated otherwise. We have also established that there seems to be a systematic difference between the super profile parameters derived from residual and non-residual scaled cubes. We therefore test which of the two types of data cube (i.e. residual vs non-residual scaled) is relevant for our purpose. To do this, we created various model data cubes using different input profile parameter values (σ_b, σ_n, A_n/A_b, a_n/a_b), for which we then

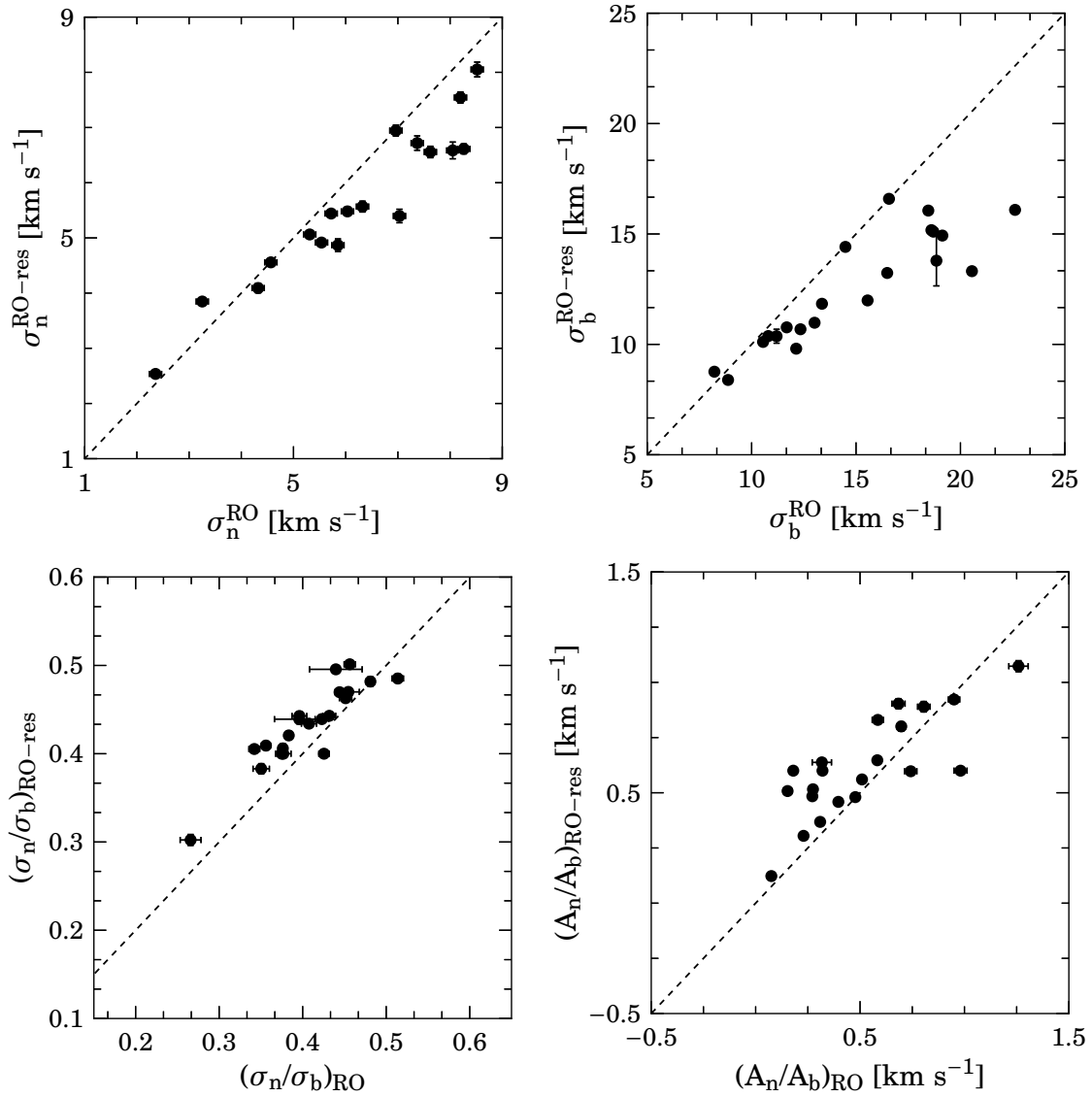

Figure 6: Comparison of the super profile parameters from the RO and RO-res cubes.

simulate a THINGS-like observation with the VLA. These artificial observations are processed and deconvolved exactly like the real THINGS observations. The aim is to see which of the residual and non-residual scaled cubes best recover the input parameters.

Table 2 and 3 illustrate the results from the various models whose input parameters are shown in bold. The conclusions can be summarized as follows. Both the residual and non-residual scaled model data cubes give similar σ_n values. However, the non-residual scaled cubes give σ_b values that are overestimated by up to $\sim 16\%$, whereas the residual-scaled ones result in σ_b similar to the input values. In addition, the non-residual scaled cubes tend to underestimate the A_n/A_b ratios, especially for lower input peak flux values (i.e. lower S/N). The derived A_n/A_b ratios from the residual-scaled cubes,

Table 2
Parameters from different set of model data cubes I

Non-residual scaled				Residual-scaled			
σ_n (km s^{-1})	σ_b (km s^{-1})	Peak flux mJy	A_n/A_b	σ_n (km s^{-1})	σ_b (km s^{-1})	Peak flux mJy	A_n/A_b
6.00	**16.00**	**10.00**	**0.60**	**6.00**	**16.00**	**10.00**	**0.60**
6.16 ± 0.04	17.89 ± 0.14	11.45	0.54 ± 0.02	6.0 ± 0.27	15.76 ± 0.85	11.12	0.59 ± 0.59
6.00	**16.00**	**5.00**	**0.60**	**6.00**	**16.00**	**5.00**	**0.60**
6.2 ± 0.09	18.39 ± 0.33	5.99	0.48 ± 0.04	6.01 ± 0.55	15.61 ± 1.72	5.54	0.6 ± 0.6
6.00	**16.00**	**2.50**	**0.60**	**6.00**	**16.00**	**2.50**	**0.60**
6.15 ± 0.22	18.45 ± 0.64	3.25	0.4 ± 0.08	6.04 ± 1.13	15.52 ± 3.56	2.75	0.62 ± 0.62
6.00	**16.00**	**10.00**	**1.00**	**6.00**	**16.00**	**10.00**	**1.00**
6.12 ± 0.04	18.15 ± 0.21	11.45	0.78 ± 0.04	6.0 ± 0.23	15.7 ± 1.14	11.12	0.93 ± 0.93
6.00	**16.00**	**5.00**	**1.00**	**6.00**	**16.00**	**5.00**	**1.00**
6.16 ± 0.08	18.62 ± 0.42	5.99	0.68 ± 0.07	6.02 ± 0.47	15.59 ± 2.33	5.54	0.95 ± 0.95
6.00	**16.00**	**2.50**	**1.00**	**6.00**	**16.00**	**2.50**	**1.00**
6.13 ± 0.19	18.29 ± 0.79	3.25	0.56 ± 0.12	6.06 ± 0.96	15.54 ± 4.86	2.75	1.0 ± 1.0
8.00	**20.00**	**10.00**	**0.60**	**8.00**	**20.00**	**10.00**	**0.60**
8.17 ± 0.06	22.19 ± 0.28	11.45	0.56 ± 0.03	7.98 ± 0.38	19.63 ± 1.35	11.12	0.61 ± 0.61
8.00	**20.00**	**5.00**	**0.60**	**8.00**	**20.00**	**5.00**	**0.60**
8.32 ± 0.12	23.35 ± 0.57	5.99	0.51 ± 0.05	7.97 ± 0.78	19.33 ± 2.67	5.54	0.62 ± 0.62
8.00	**20.00**	**2.50**	**0.60**	**8.00**	**20.00**	**2.50**	**0.60**
8.24 ± 0.25	23.48 ± 0.99	3.25	0.42 ± 0.08	7.94 ± 1.61	18.92 ± 5.26	2.75	0.62 ± 0.62
8.00	**20.00**	**10.00**	**1.00**	**8.00**	**20.00**	**10.00**	**1.00**
8.15 ± 0.05	22.65 ± 0.35	11.45	0.82 ± 0.05	7.98 ± 0.33	19.5 ± 1.79	11.12	0.96 ± 0.96
8.00	**20.00**	**5.00**	**1.00**	**8.00**	**20.00**	**5.00**	**1.00**
8.23 ± 0.1	23.77 ± 0.73	5.99	0.72 ± 0.08	7.98 ± 0.67	19.2 ± 3.57	5.54	0.98 ± 0.98
8.00	**20.00**	**2.50**	**1.00**	**8.00**	**20.00**	**2.50**	**1.00**
8.19 ± 0.19	23.39 ± 1.1	3.25	0.59 ± 0.11	7.96 ± 1.39	18.8 ± 7.09	2.75	0.99 ± 0.99

Note. — The input parameters for each models are represented in bold, whereas the derived parameters from the resulting cubes are shown in regular fonts.

however, are similar to the input values and do not depend on the input peak flux. Furthermore, for the non-residual scaled cubes, when we go from higher to lower input peak flux, the σ_n and σ_b values stay basically the same, whereas the broad component amplitude becomes higher and therefore its area also gets larger. This result in a decrease in the a_n/a_b and A_n/A_b ratios. Thus in the low S/N regime, the A_n/A_b ratio from non-residual scaled cubes can be underestimated. For example, in our model, where the S/N is ∼3.6, the A_n/A_b ratio is underestimated by up to ∼30%. For the residual-scaled cubes, the derived A_n/A_b ratios and the input values agree within ∼12% for the same S/N. To illustrate these, we show the shapes of the super profiles, the narrow and broad components in Figure 7 for a range of S/N for both the residual and non-residual scaled cubes.

Figure 8 and Figure 9 show the histograms of the single Gaussian and second moment velocity dispersions derived from the model data cubes with input constant velocity dispersion of 12 km s^{-1} and various input peak flux values. For the NA cubes, the velocity dispersions from both the single

Table 3
Parameters from different set of model data cubes II

Non-residual scaled					Residual-scaled				
σ_n (km s^{-1})	σ_b (km s^{-1})	Peak flux mJy	A_n/A_b	a_n/a_b	σ_n (km s^{-1})	σ_b (km s^{-1})	Peak flux mJy	A_n/A_b	a_n/a_b
6.00	**16.00**	**10.00**	**0.60**	**1.50**	**6.00**	**16.00**	**10.00**	**0.60**	**1.50**
6.16 ± 0.24	17.9 ± 0.87	11.45	0.54 ± 0.14	1.56 ± 0.12	6.0 ± 0.03	15.7 ± 0.1	11.06	0.59 ± 0.02	1.56 ± 0.02
6.00	**16.00**	**5.00**	**0.60**	**1.50**	**6.00**	**16.00**	**5.00**	**0.60**	**1.50**
6.2 ± 0.47	18.4 ± 1.61	5.99	0.48 ± 0.22	1.42 ± 0.2	6.01 ± 0.06	15.6 ± 0.2	5.51	0.6 ± 0.05	1.57 ± 0.04
6.00	**16.00**	**2.50**	**0.60**	**1.50**	**6.00**	**16.00**	**2.50**	**0.60**	**1.50**
6.15 ± 0.91	18.5 ± 2.67	3.25	0.4 ± 0.32	1.19 ± 0.29	6.04 ± 0.12	15.5 ± 0.37	2.73	0.62 ± 0.09	1.6 ± 0.08
6.00	**16.00**	**1.25**	**0.60**	**1.50**	**6.00**	**16.00**	**1.25**	**0.60**	**1.50**
5.97 ± 1.83	17.7 ± 3.94	1.84	0.31 ± 0.46	0.92 ± 0.42	6.13 ± 0.23	15.7 ± 0.77	1.34	0.67 ± 0.2	1.71 ± 0.17
6.00	**16.00**	**10.00**	**0.93**	**2.33**	**6.00**	**16.00**	**10.00**	**0.93**	**2.33**
6.12 ± 0.2	18.1 ± 1.12	11.45	0.78 ± 0.22	2.33 ± 0.21	6.0 ± 0.03	15.7 ± 0.13	11.06	0.93 ± 0.04	2.43 ± 0.04
6.00	**16.00**	**5.00**	**0.93**	**2.33**	**6.00**	**16.00**	**5.00**	**0.93**	**2.33**
6.16 ± 0.39	18.6 ± 2.02	5.99	0.68 ± 0.34	2.06 ± 0.31	6.01 ± 0.05	15.6 ± 0.25	5.51	0.95 ± 0.08	2.47 ± 0.07
6.00	**16.00**	**2.50**	**0.93**	**2.33**	**6.00**	**16.00**	**2.50**	**0.93**	**2.33**
6.13 ± 0.79	18.3 ± 3.22	3.25	0.56 ± 0.49	1.68 ± 0.45	6.05 ± 0.1	15.5 ± 0.5	2.73	1.0 ± 0.17	2.56 ± 0.15
6.00	**16.00**	**1.25**	**0.93**	**2.33**	**6.00**	**16.00**	**1.25**	**0.93**	**2.33**
6.01 ± 1.63	17.1 ± 4.6	1.84	0.45 ± 0.71	1.28 ± 0.64	6.1 ± 0.19	15.7 ± 1.0	1.34	1.06 ± 0.36	2.73 ± 0.32
6.00	**16.00**	**10.00**	**0.32**	**0.80**	**6.00**	**16.00**	**10.00**	**0.32**	**0.80**
6.25 ± 0.32	17.6 ± 0.65	11.45	0.31 ± 0.08	0.88 ± 0.07	5.99 ± 0.04	15.8 ± 0.08	11.06	0.31 ± 0.01	0.82 ± 0.01
6.00	**16.00**	**5.00**	**0.32**	**0.80**	**6.00**	**16.00**	**5.00**	**0.32**	**0.80**
6.33 ± 0.63	18.2 ± 1.25	5.99	0.29 ± 0.14	0.83 ± 0.12	5.99 ± 0.09	15.7 ± 0.14	5.51	0.31 ± 0.02	0.82 ± 0.02
6.00	**16.00**	**2.50**	**0.32**	**0.80**	**6.00**	**16.00**	**2.50**	**0.32**	**0.80**
6.21 ± 1.21	18.5 ± 2.14	3.25	0.24 ± 0.21	0.72 ± 0.19	6.02 ± 0.17	15.5 ± 0.27	2.73	0.32 ± 0.05	0.82 ± 0.04
6.00	**16.00**	**1.25**	**0.32**	**0.80**	**6.00**	**16.00**	**1.25**	**0.32**	**0.80**
5.91 ± 2.41	18.1 ± 3.2	1.84	0.18 ± 0.3	0.55 ± 0.27	6.13 ± 0.32	15.5 ± 0.54	1.34	0.34 ± 0.1	0.86 ± 0.08

Note. — The input parameters for each models are represented in bold, whereas the derived parameters from the resulting cubes are shown in regular fonts.

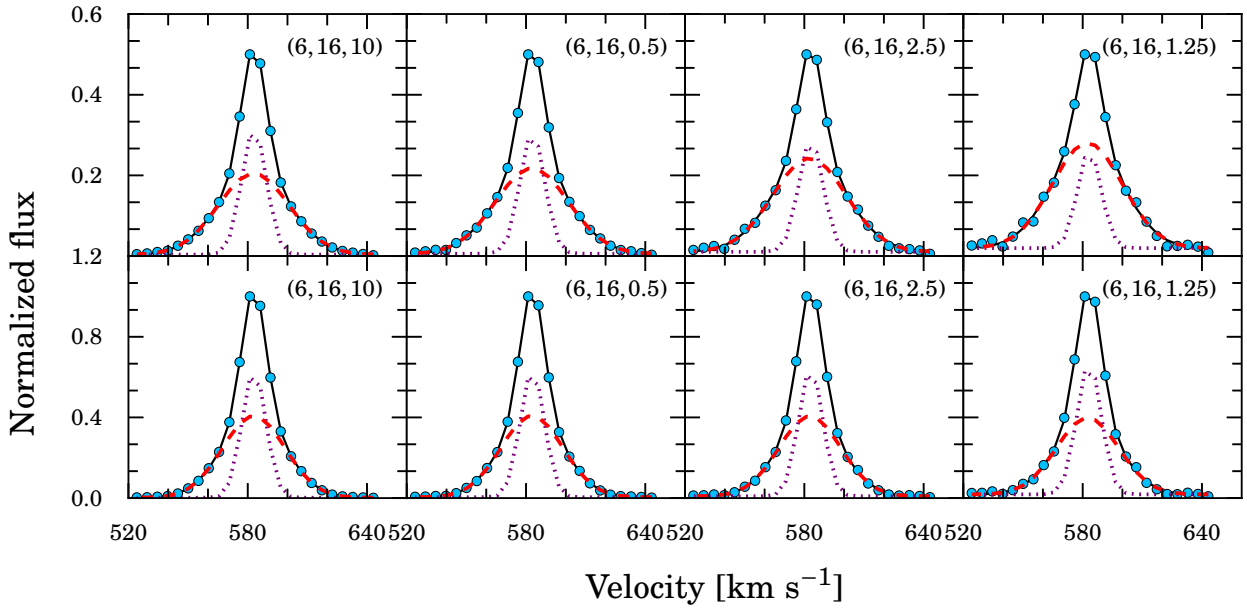

Figure 7: Synthetic super profiles from non-residual scaled cubes (top panels) and residual-scaled cubes (bottom panels). The number in each plots are the input σ_n (km s^{-1}), σ_b (km s^{-1}), and peak flux (i.e. $a_n + a_b$ in mJy) values.

Gaussian fits and second moment maps depend on the input peak flux. The derived mean velocity dispersions tend to increase from higher to lower S/N. For the lowest input peak flux, the mean single Gaussian dispersion and second moment values differ from the input dispersion by $\sim$3 and $\sim$6 km s^{-1}, respectively. For the NA-res model data cubes, the mean single Gaussian velocity dispersions are very similar to the input dispersion. We do, however, observe a steady increase in the mean second moment velocity dispersion values as we decrease the input peak flux value. The derived value differs from the input dispersion by $\sim$2 km s^{-1} for the lowest input peak flux.

The results from the simulations therefore show that residual-scaled cubes give more accurate velocity dispersion as opposed to non-residual scaled cubes, which tend to overestimate the intrinsic velocity dispersions especially in the low S/N regime. This analysis however was based on data cubes that were cleaned down to 2.5 times rms. In the following, we will explore the effect of the depth to which the data were CLEANed on the derived velocity dispersions.

Effects of cleaning on velocity dispersions

To test whether cleaning depth affects profile dispersions, we took the natural and robust non-residual scaled data cubes of NGC 3184, a face-on spiral galaxy, and cleaned down to 3.5 times rms and 1.5

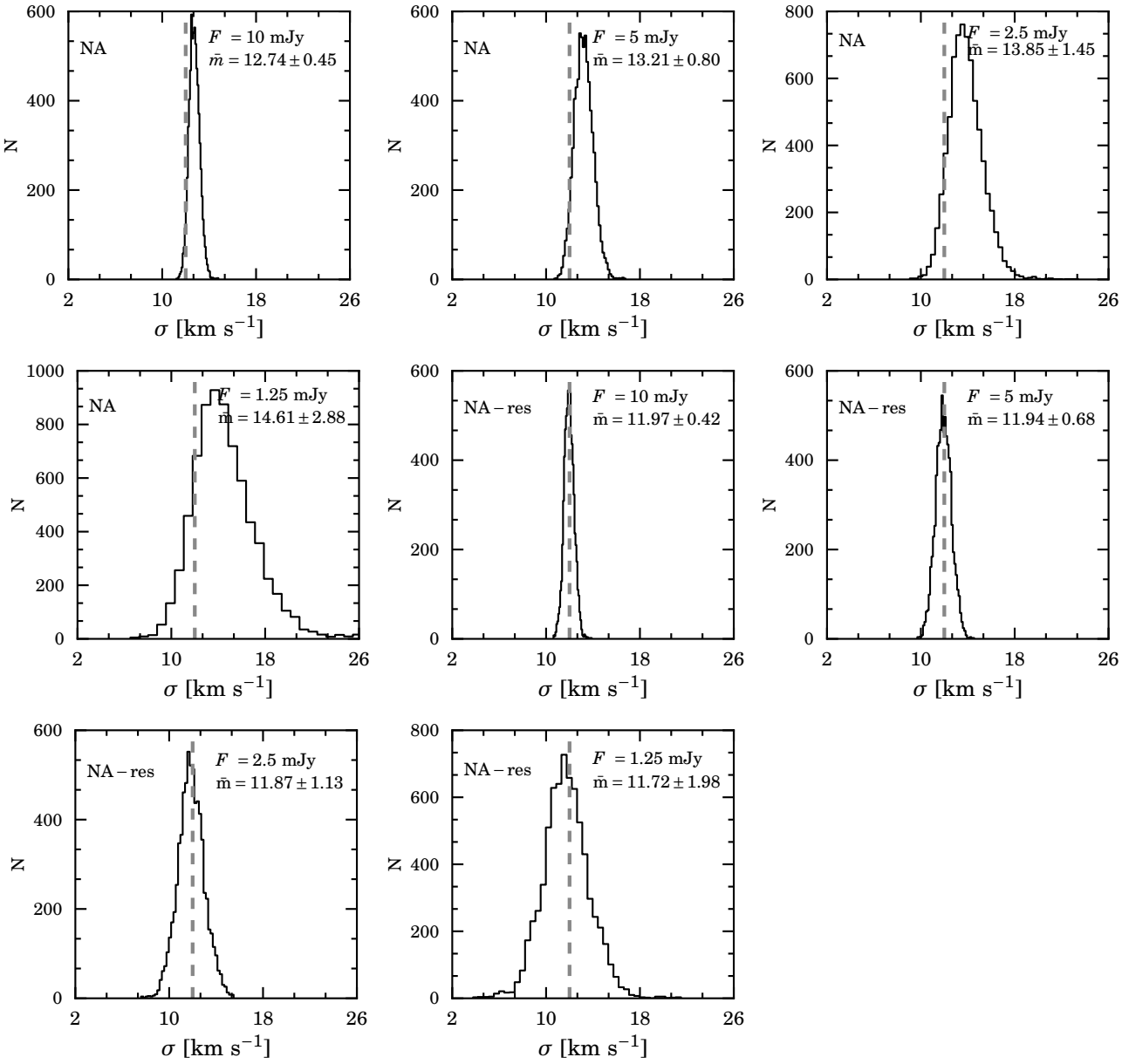

Figure 8: Histograms of single Gaussian velocity dispersions from natural non-residual (NA, first four panels) and natural residual-scaled (NA-res, last four panels) model data cubes. The numbers in each panels represent the input peak flux and the output mean velocity dispersion values. The vertical dashed lines represent the input velocity dispersion (12 km s^{-1}) used to make the models.

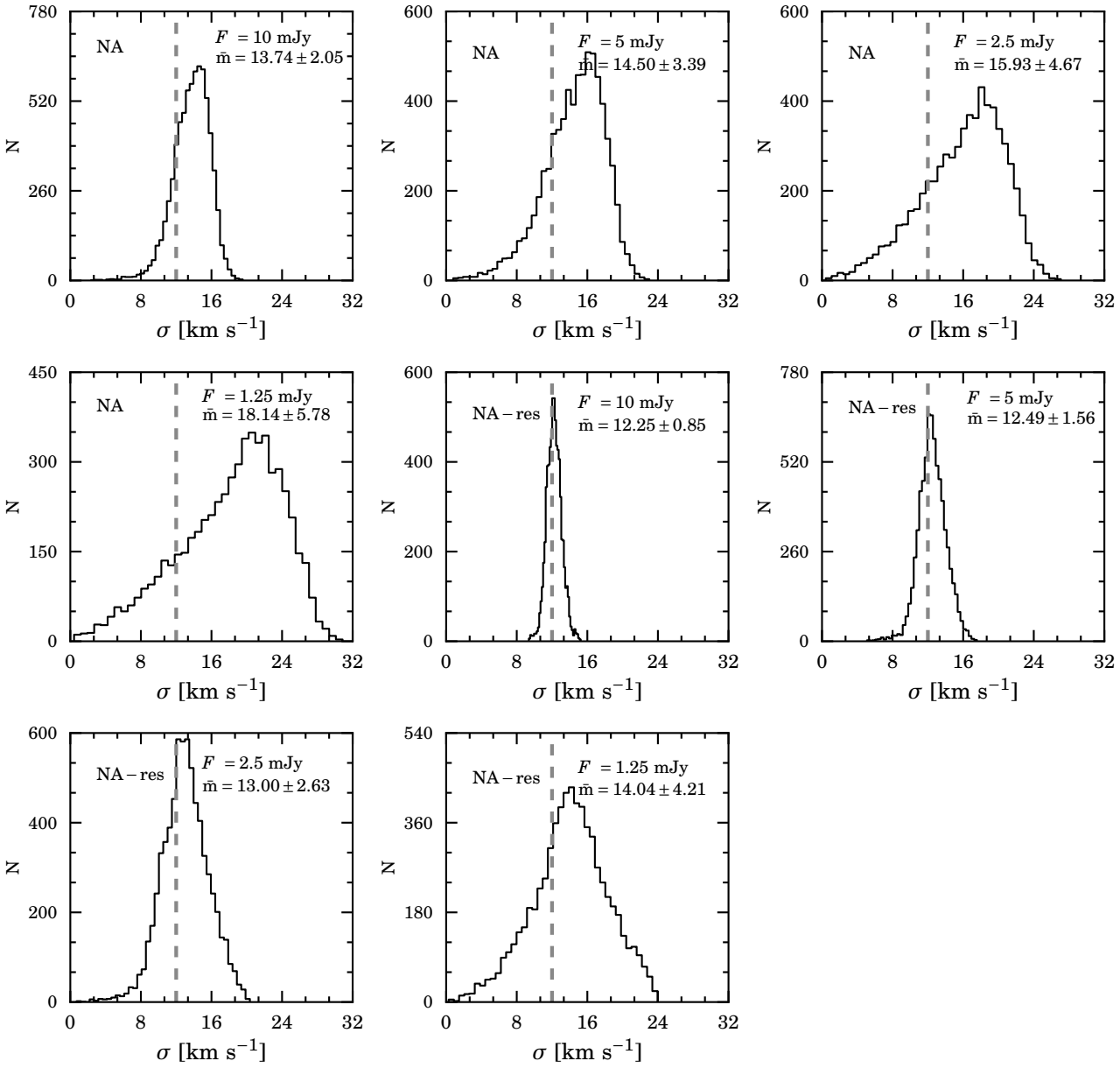

Figure 9: Histograms of second moment velocity dispersions from the natural non-residual scaled (NA, first four panels) and natural residual-scaled (NA-res, last four panels) scaled model data cubes. The numbers in each panels represent the input peak flux and the output mean velocity dispersion values. The vertical dashed lines represent the input velocity dispersion (12 km s^{-1}) used to make the models.

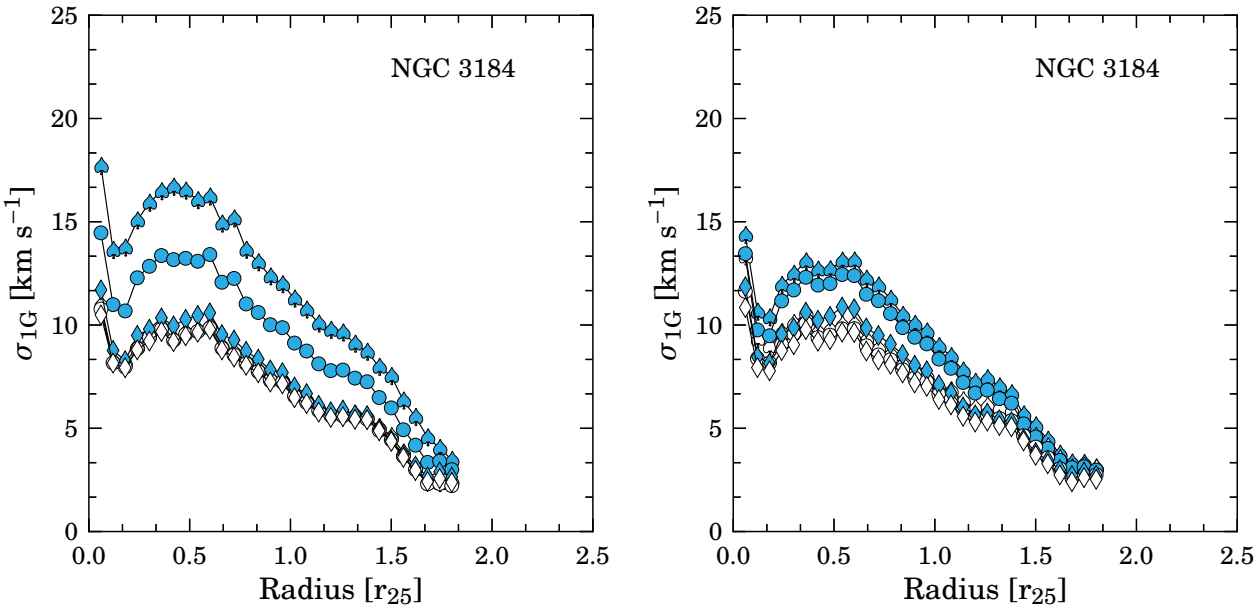

Figure 10: Radial velocity dispersion profiles of NGC 3184 using non-residual (solid symbols) and residual-scaled (open symbols) cubes. The left panels are results from natural-weighted data cubes and the right panels are from robust-weighted data cubes. Different symbols represent different cleaning level. Spade symbols: 3.5 times rms. Circle symbols: 2.5 times rms. Diamond symbols: 1.5 times rms.

times rms in addition to the already available 2.5 times rms cube. We also created residual-scaled versions of the (3.5 times rms, 2.5 times rms, 1.5 times rms) cubes. In Figure 10, we plot the radial single Gaussian velocity dispersions of NGC 3184 derived from the super profiles of the (3.5 times rms, 2.5 times rms, 1.5 times rms) cubes. It is clear that the difference between the velocity dispersions derived from the non-residual and residual-scaled cubes becomes smaller when the cubes are cleaned deeply. For the 1.5 times rms cubes, the velocity dispersion derived from the non-residual and residual-scaled cubes are identical. We show the shapes of the super profiles from the (3.5 times rms, 2.5 times rms, 1.5 times rms) cubes in Figure 11. As already shown in the previous analysis, the residual-scaling correction is much less for the robust-weighted cubes.

After demonstrating that velocity profile parameters from non-residual scaled data cubes tend to be overestimated (unless the cubes are cleaned very deeply, which is computationally expensive) we decided to use the natural-weighted residual-scaled cubes in this thesis.

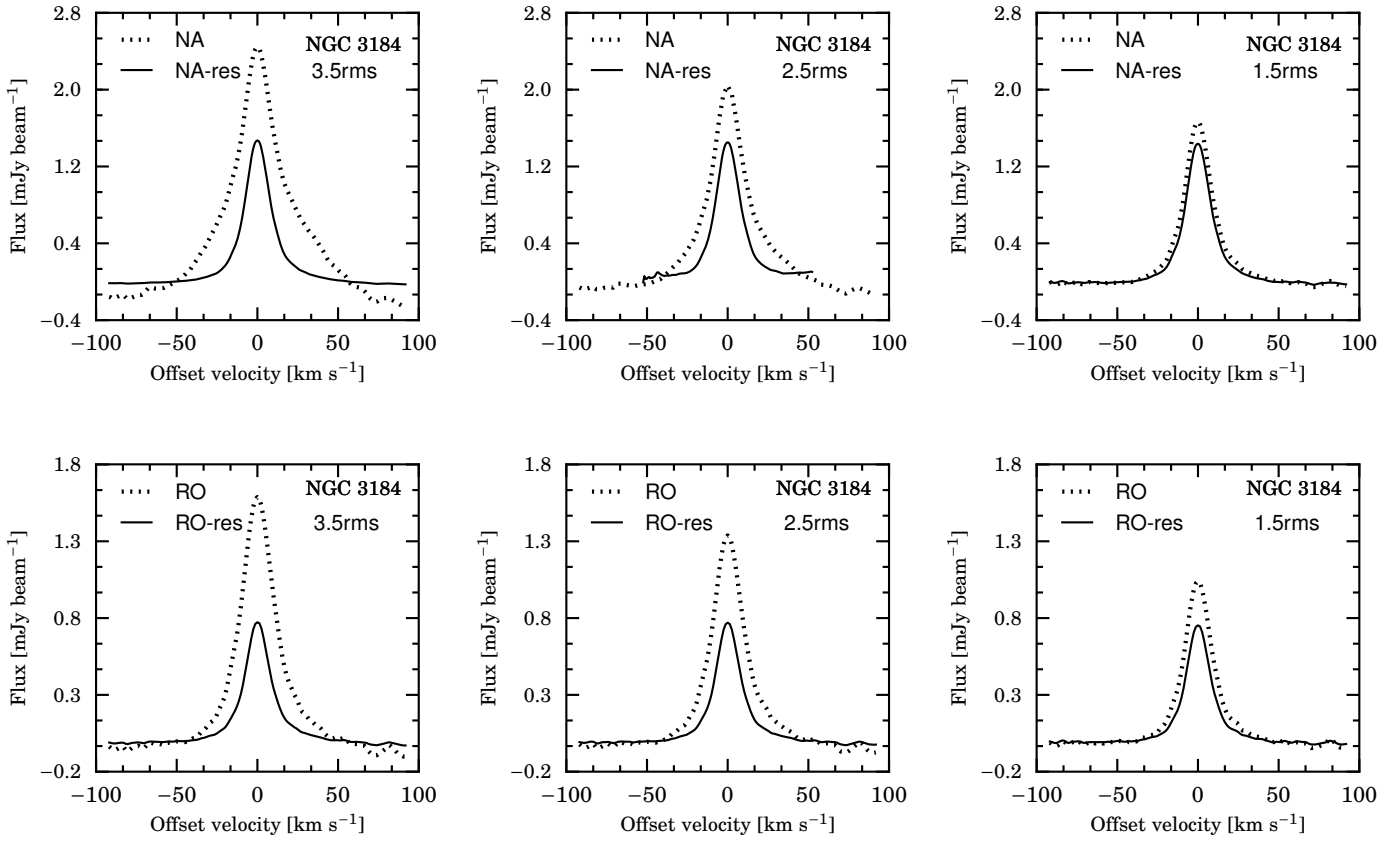

Figure 11: Super profile shapes from non-residual scaled (dotted lines) and residual-scaled (solid lines) data cubes of NGC 3184 at a radius of 0.75 r_{25}. The top panels are profiles from natural-weighted data cubes and the bottom panels are profiles from robust-weighted data cubes. From left to right, the data cubes are cleaned down to a level of 3.5 times rms, 2.5 times rms and 1.5 times rms.

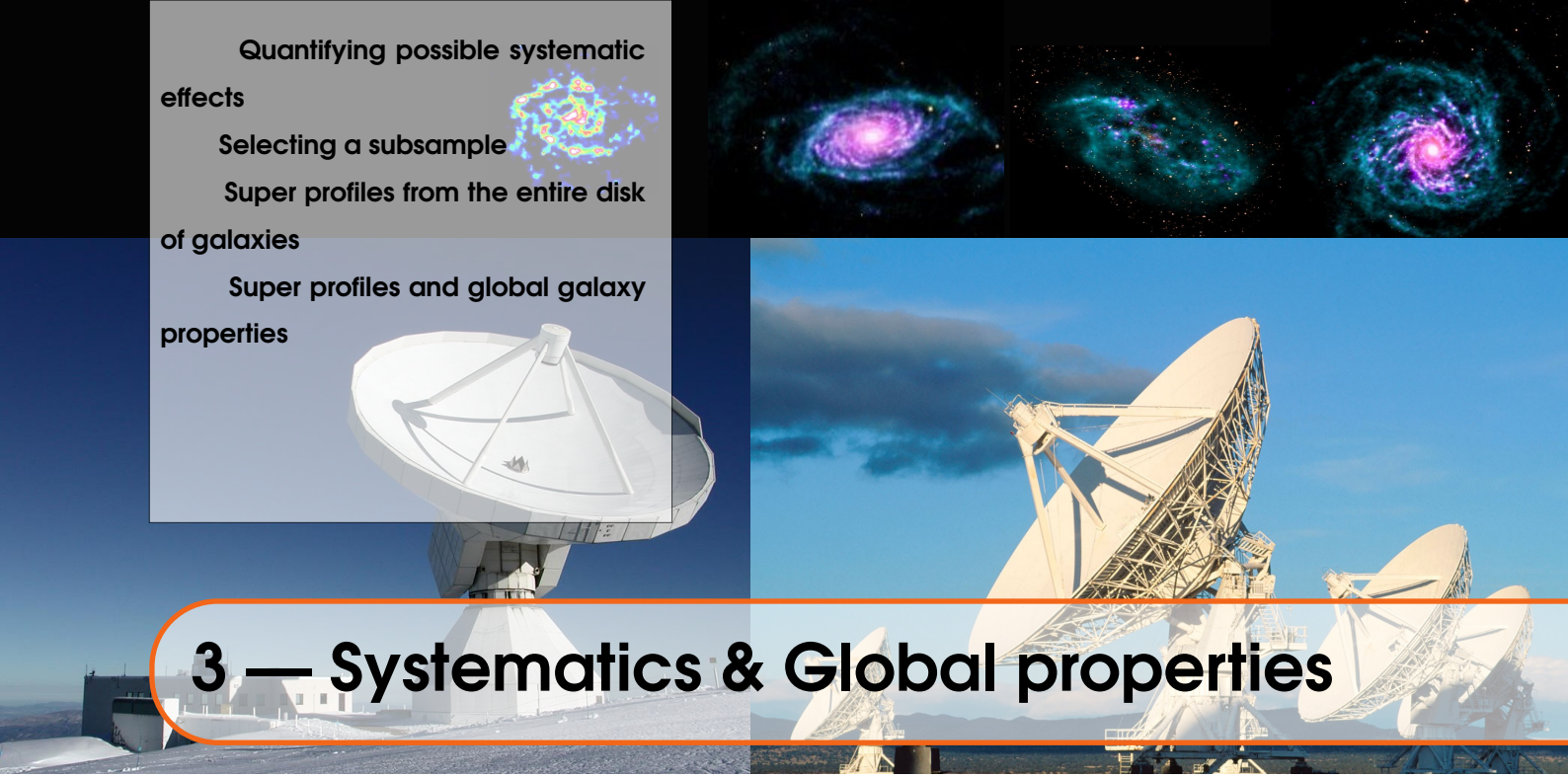

3 — Systematics & Global properties

3.1 Quantifying possible systematic effects

Despite the high S/N profile obtained with the stacking method described in the previous chapter, the analysis of this profile requires careful checks on possible systematic effects resulting from the presence of individual asymmetric profiles or the broadening due to the stacking method itself. In addition, other effects from beam-smearing, major bulk motion of gas along the line-of-sight, the presence of thick HI disks and lagging halos, the presence of lines of sight with high intensities and narrow dispersions, the resolution and inclination of the galaxy also need to be quantified as they can change the intrinsic shapes of the super profiles. Detailed discussions of these can be found in Ianjamasimanana et al. (2012). For reference, we also present these tests in this chapter. The idea is to see if the non-Gaussianity of the super profiles could be due to these effects or whether it represents the intrinsic state of the ISM.

3.1.1 Modeling the effects of resolution and inclination

The gradient in rotation velocity across the finite beam of a telescope can broaden velocity profiles. Although the THINGS galaxies have been observed at relatively high resolution, this could still affect the shapes of the profiles, especially for highly inclined galaxies.

To quantify these effects, we construct model data cubes of IC 2574 and NGC 2403 using the GIPSY task GALMOD. IC 2574 is a dwarf galaxy with a solid body rotation curve, a distance of $\sim$4 Mpc and an inclination of 53°. NGC 2403 is a well resolved, rotation dominated galaxy typical of

spirals found in the THINGS sample.

For the NGC 2403 models we use the observed position angle and inclination (63°) as given in de Blok et al. (2008). We adopt a vertical Gaussian scale height of 100 pc, a *single* component velocity dispersion of 8 km s^{-1}, a constant HI surface density and a constant rotation curve of 130 km s^{-1} (the maximum observed rotation velocity of NGC 2403). We adopt a channel spacing of 5.2 km s^{-1} as in the THINGS observations. We also create an almost identical model, but with an inclination of 80° (note that the highest inclination in our sample is 76°). We smooth these model data cubes to various resolutions and create the corresponding super profiles. We fit the artificial super profiles both with a single and a double Gaussian to see how the dispersion changes with resolution and to check whether resolution and inclination can create broad and narrow components from a single input component. We have also tested a case where the input rotation curve rises linearly up to 130 km s^{-1} at 1 kpc and flattens. The results from the constant and the linearly rising plus flat rotation curve models are identical.

For the IC 2574 models, we use the average position angle derived by de Blok et al. (2008), but assume an inclination of 63° and 80° to facilitate a direct comparison with the NGC 2403 models. Here we also use a *single* component velocity dispersion of 8 km s^{-1}, a constant HI surface density but an input rotation curve that rises linearly to 80 km s^{-1} at the edge of the HI disk. We use a channel spacing of 2.6 km s^{-1} as used by THINGS for IC 2574. We adopt a vertical Gaussian scale height of 0.1 kpc. We fit the model super profiles of the IC 2574 with both single and double Gaussians but the results of the double Gaussian decomposition are not meaningful as the super profiles are almost perfectly Gaussian. So, for the IC 2574 models, we only present the single Gaussian fitting results. We have also tested the case where the scale height is 0.5 kpc but the results are similar to the 0.1 kpc models.

Figure 12 and Table 4 summarize the model super profile parameters as a function of the resolution. It is clear that profiles become broader with decreasing resolution, and more so for a higher inclination. For example, at 11″ (the average resolution of THINGS), the difference between the velocity dispersion measured from the 80° and the 63° inclination model data cubes of NGC 2403 is $\sim 9\%$. At a resolution of 60″, the difference is $\sim 29\%$. From Figure 12, it is apparent that we do not recover the input 8 km s^{-1} dispersion even at very high resolution. This is a result of the finite channel spacing of the NGC 2403 data cubes used (5.2 km s^{-1}) in combination with the high inclination. However, for the IC 2574 models, the velocity dispersions approach the input 8 km s^{-1} value, and this is due to the smaller

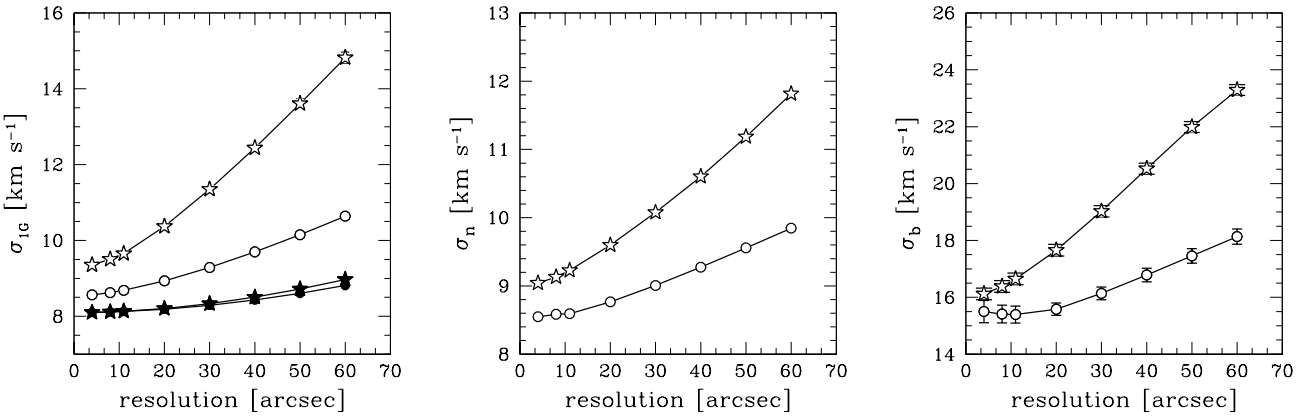

Figure 12: Super profile parameters derived from the model data cubes of IC 2574 and NGC 2403 as a function of the resolution. Solid and open symbols represent the models of IC 2574 and NGC 2403, respectively. The circle symbols represent the 63° models, whereas the star symbols represent the 80° inclination models. We only present the single Gaussian fitting results of the IC 2574 models as these profiles do not show a double Gaussian function signature. *Left panel:* single Gaussian velocity dispersion. *Middle panel:* Narrow component velocity dispersion. *Right panel*: Broad component velocity dispersion.

channel spacing used (2.6 km s^{-1}).

Figure 13 shows a selection of the modelled super profiles of NGC 2403. It is clear that resolution effects can introduce a spurious broad component. We use the ratio between the areas of the narrow and broad components A_n/A_b (i.e., the flux or mass ratio) to gauge whether any of the models resemble the data. Figure 14 shows the A_n/A_b ratio as a function of resolution. This ratio decreases with resolution, showing the increasing importance of the spurious broad component. The extremely high ratios at high resolution should not be over-interpreted. These are simply due to the fitting routine being forced to fit an almost perfectly Gaussian profile with two components. At the lowest resolution in the models, the broad component created by the low resolution accounts for $\sim 13\%$ of the total flux. In the THINGS data, the broad component accounts for up to $\sim 70\%$ of the total flux. This discrepancy also indicates that resolution effects are not solely responsible for the observed broad components. Comparison of the models and data shows that at $11''$ (the typical THINGS resolution), the resulting super profile is well fitted by a single Gaussian function. It also shows that the shape of the super profile only starts to significantly deviate from a single Gaussian at a resolution about six times worse than the THINGS resolution. In summary, models with single Gaussian input profiles are well recovered by the THINGS

Table 4
Effect of the resolution on the shapes of the super profiles

NGC 2403 models						IC 2574 models	
Resolution		Velocity dispersion			Flux ratio	Resolution	Velocity dispersion
($''$)	(pc)	σ_{1G} (km s^{-1})	σ_n (km s^{-1})	σ_b (km s^{-1})	A_n/A_b	(pc)	σ_{1G} (km s^{-1})
Inclination: 63°							
4	62	8.6	8.5	15.5	83.3	78	8.1
8	124	8.6	8.6	15.4	60.6	155	8.1
11	171	8.6	8.6	15.4	56.6	213	8.1
20	310	8.9	8.8	15.6	23.4	388	8.2
30	465	9.3	9.0	16.1	12.4	582	8.3
40	621	9.8	9.3	16.8	7.9	776	8.4
50	776	10.1	9.6	17.5	5.6	970	8.6
60	931	10.6	9.8	18.1	4.2	1164	8.8
Inclination: 80°							
4	62	9.4	9.0	16.1	9.0	78	8.1
8	124	9.5	9.1	16.4	7.7	155	8.1
11	171	9.7	9.2	16.6	6.6	213	8.1
20	310	10.4	9.6	17.7	4.0	388	8.2
30	465	11.4	10.0	19.0	2.6	582	8.3
40	621	12.5	10.6	20.5	1.8	776	8.5
50	776	13.6	11.2	21.9	1.4	970	8.7
60	931	14.9	11.8	23.3	1.2	1164	9.0

Note. — σ_{1G}: Velocity dispersion derived from one-component Gaussian fit. σ_n: Velocity dispersion of the narrow component. σ_b: Velocity dispersion of the broad component. A_n/A_b: Ratio of the fluxes or masses associated with the narrow and broad components. Here, only the single Gaussian results of the IC 2574 models are shown.

resolution.

The previous test investigated whether double components can be spuriously created using single component input models. We now investigate whether input double components can be recovered from limited resolution models. We use the 63° inclination model of NGC 2403 described before. Recall that this model assumes a filled HI disk with a Gaussian velocity dispersion of 8 km s^{-1}. We will here refer to this as the broad component model. We also construct a second set of cubes, assuming a 4 km s^{-1} dispersion and disks that are only partially filled (we assume 20%, 40%, 60% and 80% area filling factors). We refer to these as the narrow component models. We add each of the narrow component models to the broad component model, smooth the resulting cubes to different resolutions and then derive the corresponding super profiles. The narrow component models are scaled to give input A_n/A_b ratios equal to unity in the regions where both narrow and broad components are present.

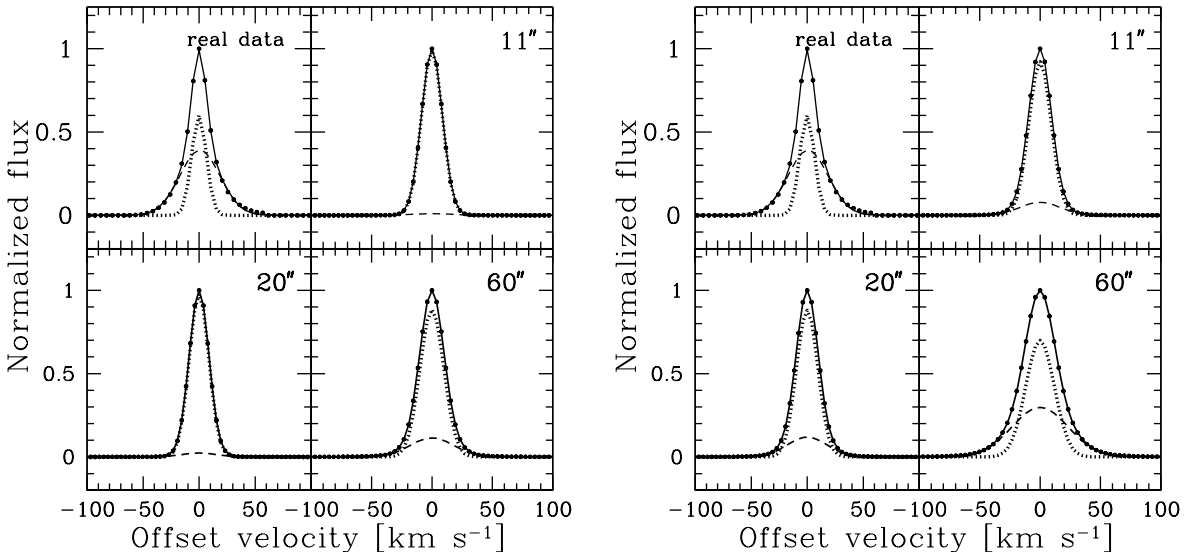

Figure 13: Observed and simulated super profiles of NGC 2403 derived after smoothing the model data cubes to the resolution indicated on the plots. The left and right panels represent the results from the model data cubes of NGC 2403 with input inclination of 63° and 80°, respectively. The dotted and the dashed lines represent the narrow and broad components required in the double Gaussian fitting. The solid lines represent the results of the double Gaussian fitting.

Figure 15 shows the measured narrow and the broad components velocity dispersions derived from the smoothed models, as a function of resolution. At high resolution, the super profile shapes are sensitive to area filling factor of the narrow component. As we increase the number of narrow profiles in the disk, the super profiles' narrow and broad component velocity dispersions approach the input dispersions of the narrow and broad component disks, respectively. At low resolutions, the super profile parameters become insensitive to the narrow component filling factor. The models thus show that at the THINGS resolution we are able to recover the presence of narrow and broad components from the models.

3.1.2 Effect of high intensity profiles

Another possible explanation for the non-Gaussianity could be that the shapes of the super profiles are dominated by a few lines of sight with high intensities and narrow dispersions. This implies some correlation between peak brightness of the input profiles and velocity dispersion. To test this, we create super profiles using the 50% brightest and 50% faintest (in terms of peak brightness) profiles in each galaxy.

We compare the parameters of the faint and the bright super profiles of each galaxy in Figure 16.

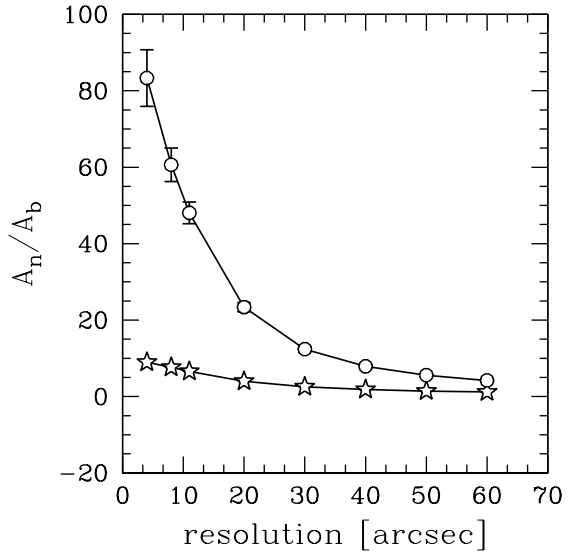

Figure 14: Flux ratio of the narrow and broad components, A_n/A_b, derived from the model data cubes of NGC 2403 as a function of the resolution. The open circle and star symbols represent the 63° and the 80° inclination models, respectively.

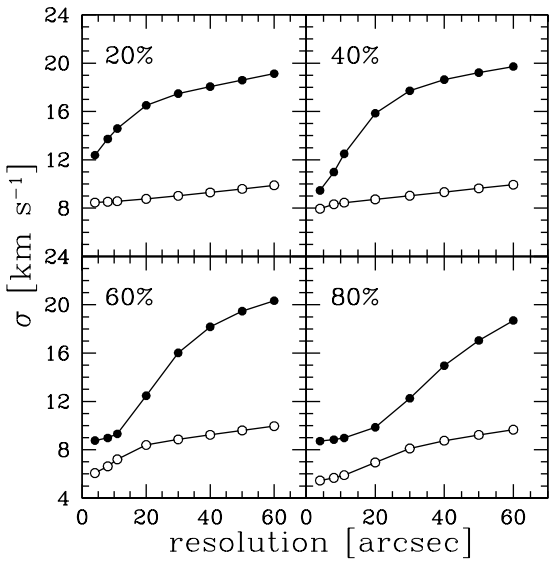

Figure 15: Velocity dispersions derived from the modelled narrow and broad disk models (see Section 3.1) as a function of the resolution. Open circles represent the narrow component. Filled circles represent the broad component. The percentage indicates the narrow profile disk filling factor.

Most velocity dispersion points scatter around the line of equality. However, four high dispersion galaxies systematically deviate. These are NGC 2841, NGC 3521, NGC 3627 and NGC 925 (in order from highest to lowest difference). This may indicate some kind of bulk motion of gas caused by, e.g., interaction or tidal effects in these galaxies. In terms of area, the faint super profiles show A_n/A_b ratios that tend to be smaller than those of the bright super profiles. The mean difference between the bright and faint A_n/A_b ratios is $\sim$36%. As most of the faint profiles are found in the outer disks of the galaxies, this seems to indicate that the A_n/A_b ratio in the outer HI disks is smaller than in the inner disks. On the whole though, it is clear that the dispersions of the super profiles of the bright and faint parts are not significantly different.

As an additional test, we also create super profiles by normalizing individual profiles by their peak intensity before summing them. This way, any possible effects of a small number of bright input profiles are removed. Figure 16 shows that, in terms of velocity dispersion, the normalized super profiles are very similar to the original ones. The correlation coefficient is $R^2 \simeq 0.99$ for both the narrow and the broad components. In terms of area, the A_n/A_b ratios derived from the normalized super profiles tend to be smaller than those from the original super profiles. The difference between the mean values is, however, only $\sim$1.3%. In summary, the shapes of the super profiles are not dominated by high intensity, narrow dispersion input profiles.

3.1.3 Effect of radial motions

A net radial motion in one direction will create an asymmetric tail in the velocity profiles. More specifically, for a given radial motion, the location of the tail with respect to the profile depends on the spatial position of the profile: a radial motion causing a tail on the high-velocity side of a profile that is located on one side of the major axis of the galaxy, will create a tail on the low-velocity side of the profile when it is located on the opposite side of the major axis. See Warner et al. (1973) and van der Kruit and Allen (1978) for a detailed discussion of these kind of patterns typically observed in velocity fields and profiles.

Figure 17 shows examples of super profiles extracted from the opposite sides of the major axes of a number of galaxies. These are overplotted on top of the overall super profiles of these galaxies. We use an unambiguous definition of sides corresponding to their position angle (PA). One side of the galaxy is chosen as the one with an average position angle of 90° with respect to the receding semi-major axis (denoted as the PA+90° side); the other side has an average PA of 270° with respect to the receding

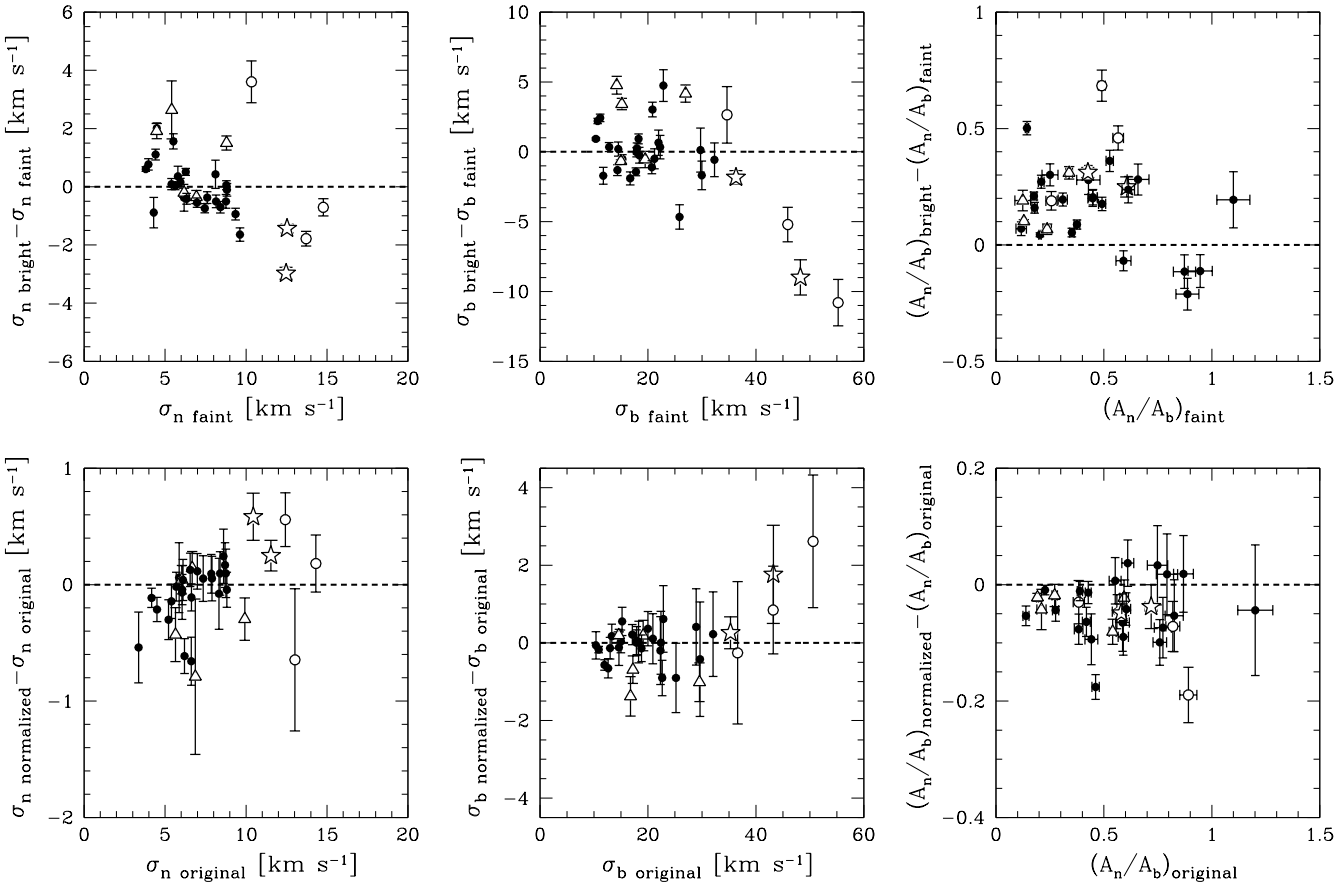

Figure 16: *Top panel:* comparison of super profile parameters derived from the faint and bright parts of galaxies. *Bottom panel:* comparison of super profile parameters from the normalized and the original super profiles. The triangle shaped symbols represent interacting or disturbed galaxies (NGC 3031, NGC 4449, NGC 5194, NGC 5457, NGC 3077). The open circle symbols represent galaxies with star bursts or mild AGN activity (NGC 1569, NGC 3521, NGC 3627). The star symbols indicate non-interacting galaxies that have an anomalously high velocity dispersion (NGC 7331, NGC 2841). The rest of the galaxies are represented by the filled circle symbols.

semi-major axis (the PA+270° side). We show in Figure 18 a histogram of the difference between the velocity dispersion derived from the opposite sides with respect to the major axes of each galaxy. For about 90% of the studied galaxies, the difference is less than 1.5 km s^{-1}. There are four galaxies with higher velocity dispersion differences. These are NGC 3031, NGC 3077 (both interacting), NGC 4826 (counter-rotating HI disk) and NGC 7331. The latter has the highest inclination (76°) in the sample and the difference in velocity dispersion for this galaxy may be a projection effect. The velocity dispersion comparison presented above only works if the distortion due to radial motions is asymmetric. Therefore, we also measure the skewness of each of the super profiles on the opposite sides of the major axis. We fit the super profiles with a Gauss-Hermite h_3 function. The skewness coefficient is defined as $4\sqrt{3}h_3$ and the results are shown in Figure 19. The apparent trend visible in the figure is mostly caused by highly inclined, interacting or disturbed, as well as starburst galaxies. It is possible that these galaxies suffer from radial motions, and thus they will not be part of our subsequent analysis. The remaining outliers have very symmetrical profiles with only some faint extended wings showing up at levels well below 20% of the peak intensity. While these affect the skewness, they contain negligible flux, and have no impact on the dispersions or flux ratios.

In the following, we develop simple models to understand how radial motions affect the shapes of the super profiles. We do this by creating models which have different ratios of rotation and radial motions. We construct a model data cube of NGC 2403 using the GIPSY task GALMOD. NGC 2403 is a well-resolved, rotation-dominated galaxy, and in some respects typical of spirals found in the THINGS sample. We use the observed position angle and inclination (63°) as given in de Blok et al. (2008). We adopt a vertical Gaussian scale height of 100 pc, a *single* component velocity dispersion of 8 km s^{-1}, a constant HI surface density and a constant rotation curve of 130 km s^{-1} (the maximum observed rotation velocity of NGC 2403). We adopt a channel spacing of 5.2 km s^{-1} as in the THINGS observations. We create four new model data cubes by adding outward radial motions of 5, 10, 15, and 20 km s^{-1} respectively to the original model (thus shifting the input profiles in velocity).

For each of the 5, 10, 15 and 20 km s^{-1} model data cubes, we randomly choose 20%, 40%, 60%, 80% of the profiles and add these to the original NGC 2403 model (which contains no radial motions). We thus create 16 data cubes with different fractions of the disk area containing asymmetric profiles with different amounts of radial motion. We smooth these model data cubes to the THINGS 11″ resolution. The velocity fields derived from the combined, smoothed cubes are then used to shuffle profiles and derive the corresponding super profiles, which we then fit with single Gaussian functions.

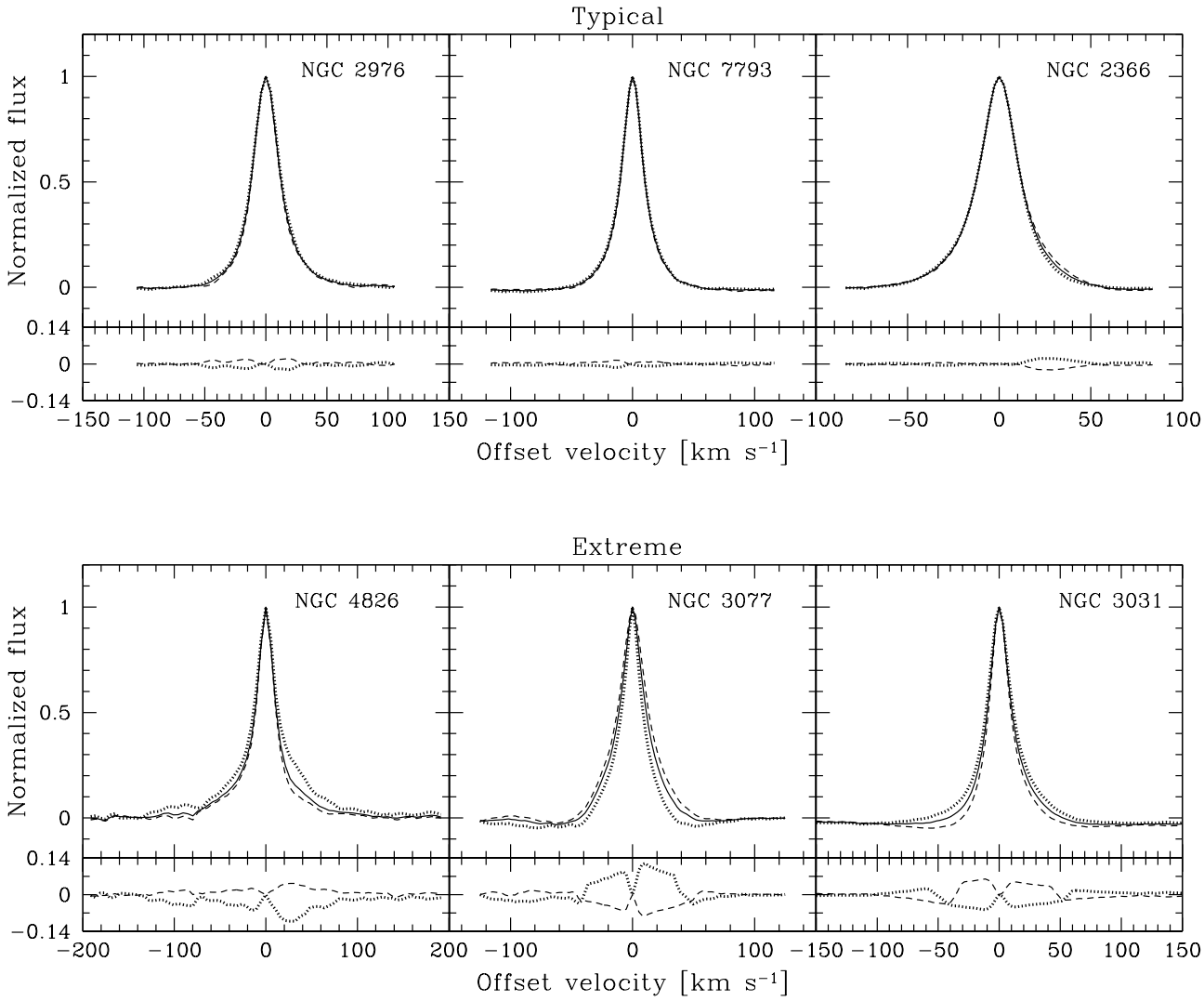

Figure 17: Super profiles extracted from the opposite sides of the major axes of each galaxy. The super profiles from the two halves of each galaxy are represented as dashed and dotted lines. The overall super profiles are represented by the solid lines. At the bottom of each panel is the difference between the super profiles from the two sides and the total super profiles. Note that the super profiles are normalized to their peak values.

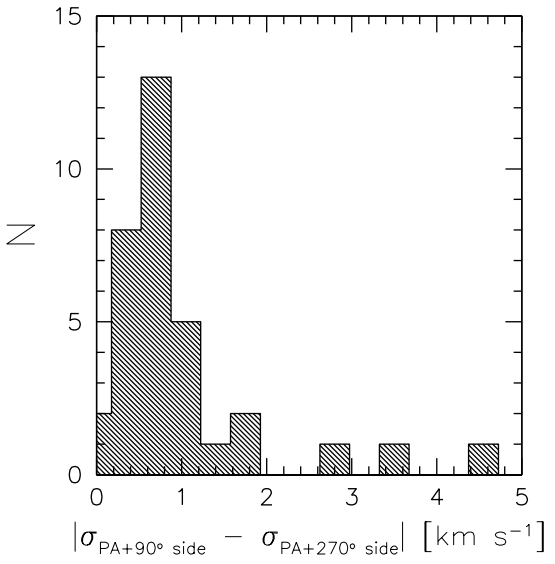

Figure 18: Histogram of the difference between the velocity dispersion derived from the opposite sides of the major axis, where PA+90° side refers to the position corresponding to a position angle (PA) of 90° with respect to the PA of the receding major axis and PA+270° side is the position corresponding to a PA offset of 270° from the receding major axis.

Figure 20 shows the resulting velocity dispersions (as measured with a single Gaussian) as a function of the input expansion velocities. As expected, the velocity dispersions increase with increasing expansion velocities. The increase is steeper as we increase the fraction of gas with non-zero expansion velocities. We see that a radial motion of 5 km s^{-1} causes only minimal broadening, independent of the area coverage. The most extreme model with 20 km s^{-1} radial motions and 80% area coverage has a super profile that is broadened by $\sim 23\%$. Large-scale non-circular motions of this magnitude are rare in disk galaxies, and mostly only found in the central parts of barred galaxies. We can compare this with the work by Trachternach et al. (2008) who used harmonic decompositions of the velocity fields of the THINGS galaxies to quantify the non-circular motions there. They found a median amplitude of all non-circular motions of $\tilde{A}_r = 6.7 \pm 5.9$ km s^{-1}. Of their 18 analyzed galaxies, 17 have $\tilde{A}_r \lesssim 10$ km s^{-1} and only one has $\tilde{A}_r > 20$ km s^{-1}.

Finally, we again use the original model of NGC 2403 (i.e. without radial motions) described previously and add it to the 5, 10, 15 and 20 km s^{-1} model data cubes (i.e. those with radial motions and different disk area coverage) but now we assume that the profiles with radial motions have an amplitude that is 30% of that of the profiles without radial motions. This choice will allow the non-

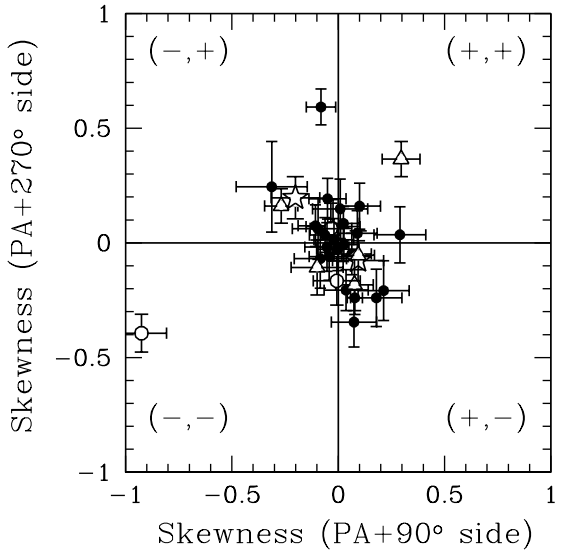

Figure 19: Skewness (defined as $4\sqrt{3}h_3$, where h_3 is the third coefficient of the Gauss-Hermite function) of the super profiles derived from the opposite sides of the major axis. *PA*+90° *side*: position corresponding to a position angle (PA) of 90° with respect to the PA of the receding major axis. *PA*+270° *side:* position corresponding to a PA offset of 270° from the receding major axis. The three outlying galaxies are, from left to right, NGC 1569, DDO 53 and NGC 3031. The plus and minus signs represent the signs of the skewness parameters. The triangle shaped symbols represent interacting or disturbed galaxies (NGC 3031, NGC 4449, NGC 5194, NGC 5457, NGC 3077). The open circle symbols represent galaxies with star bursts or mild AGN activity (NGC 1569, NGC 3521, NGC 3627). The star symbols indicate non-interacting galaxies that have an anomalously high velocity dispersion (NGC 7331, NGC 2841). The rest of the galaxies are represented by the filled circle symbols.

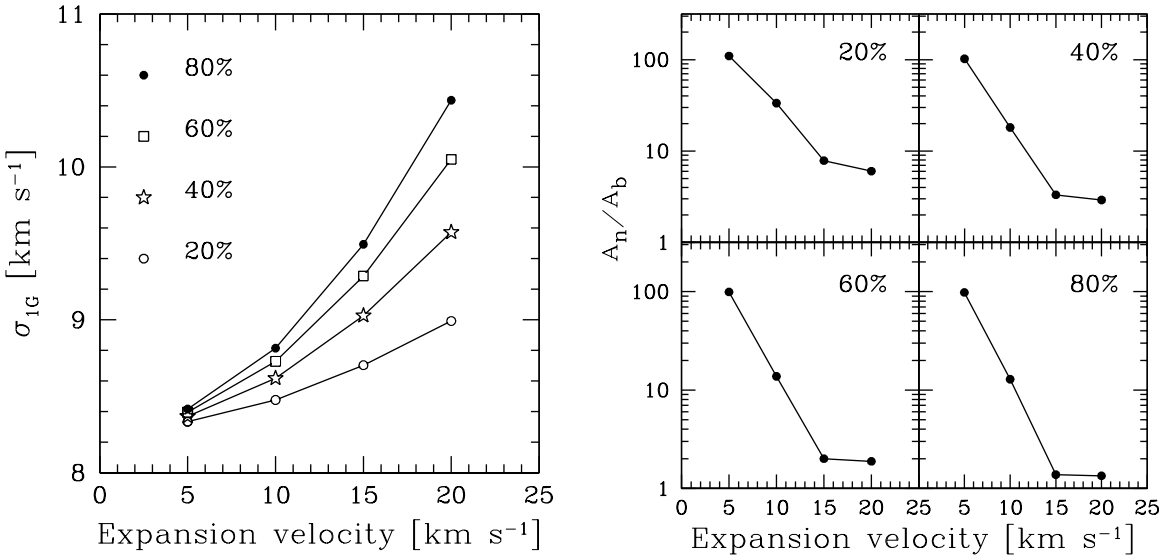

Figure 20: *Left panel*: single Gaussian velocity dispersions derived from the first set of model data cubes of NGC 2403 as a function of the input expansion velocities used to construct the models (see Section 3.1). *Right panel:* A_n/A_b ratio derived from the second set of model data cubes of NGC 2403 as a function of the expansion velocities (see Section 3.1). Percentage indicates the fraction of profiles having non-zero expansion velocities in the model data cubes.

circular motion profiles to mimic low-level broad wings in the super profiles. In this case we fit all resulting super profiles with double Gaussians. We show in Figure 20 and Table 5 the fitted A_n/A_b ratios as a function of input expansion velocities. The A_n/A_b ratio decreases with increasing expansion velocities. If we assume that the non-circular motions in the THINGS galaxies are of order 10 km s^{-1} or less (Trachternach et al., 2008), then these motions are only able to introduce spurious broad wings containing at most 7% of the total flux, i.e., much smaller than observed. We therefore conclude that radial motions cannot be a major cause of the observed non-Gaussianity of the observed super profiles.

3.1.4 Thick disks and lagging halos

Lastly, we investigate the possibility that our sample galaxies have a thin disk embedded in a “lagging" thick HI disk with a lower rotation velocity, as was found for NGC 891 (Oosterloo et al., 2007; Swaters et al., 1997) and NGC 2403 (Fraternali et al., 2002). The super profiles then represent a “cross-cut” through the global dynamics of the system, rather than a reflection of the state of the ISM. If this were the case, the lagging disk would broaden the profiles asymmetrically, depending on whether the approaching or the receding side of the galaxy is studied. Adding these two halves would give the

Table 5
Effect of the radial motions on the shapes of the super profiles

V_{rad} (km s^{-1})	A_n/A_b 20%	40%	60%	80%
5	109.8	102.1	99.3	98.2
10	33.5	18.1	13.8	12.9
15	7.9	3.3	2.0	1.4
20	6.0	2.9	1.9	1.3

Note. — V_{rad}: Input radial velocity used to construct the model data cubes. Percentage indicates the area coverage of gas with non-circular motions. A_n/A_b: Flux ratio of the narrow and broad components.

impression of the super profile having broad wings.

Figure 21 shows examples of super profiles from the approaching and receding sides of a few typical sample galaxies plotted on top of the super profiles derived from the entire disk. Note that the super profiles plotted there are normalized to their peak values. For reference we also show the most asymmetric approaching and receding super profiles in the bottom panel of Figure 21. We compare the velocity dispersions derived from the approaching and receding sides in Figure 22. For each galaxy, the largest of the velocity dispersions derived from the two halves of each galaxy is shown as σ_{large}, whereas the smallest one is given by σ_{small}. We also show a histogram of the difference between the velocity dispersions derived from the two sides in Figure 22. Of the 34 galaxies, 24 have differences less than 1 km s^{-1}; for the remaining 10 galaxies, the difference is between 1 and 4.5 km s^{-1}. Of those 10 galaxies, 4 are interacting (NGC 3031, NGC 4449, NGC 5194, NGC 5457), 2 are kinematically disturbed (NGC 1569 and NGC 3521), one is known to be a galaxy with a counter-rotating inner disk (NGC 4826). To complement our analysis, we also measure the coefficient of skewness of the super profiles in the approaching and receding sides. The result is presented in Figure 23. Most of the points in Figure 23 are offsets towards the lower right quadrant. This means that super profiles in the receding sides tend to be negatively skewed, whereas those in the approaching sides tend to be positively skewed. These are consistent with but do not by themselves prove the existence of lagging thick HI disks. Most of the outliers in Figure 23 will not be considered for further analysis.

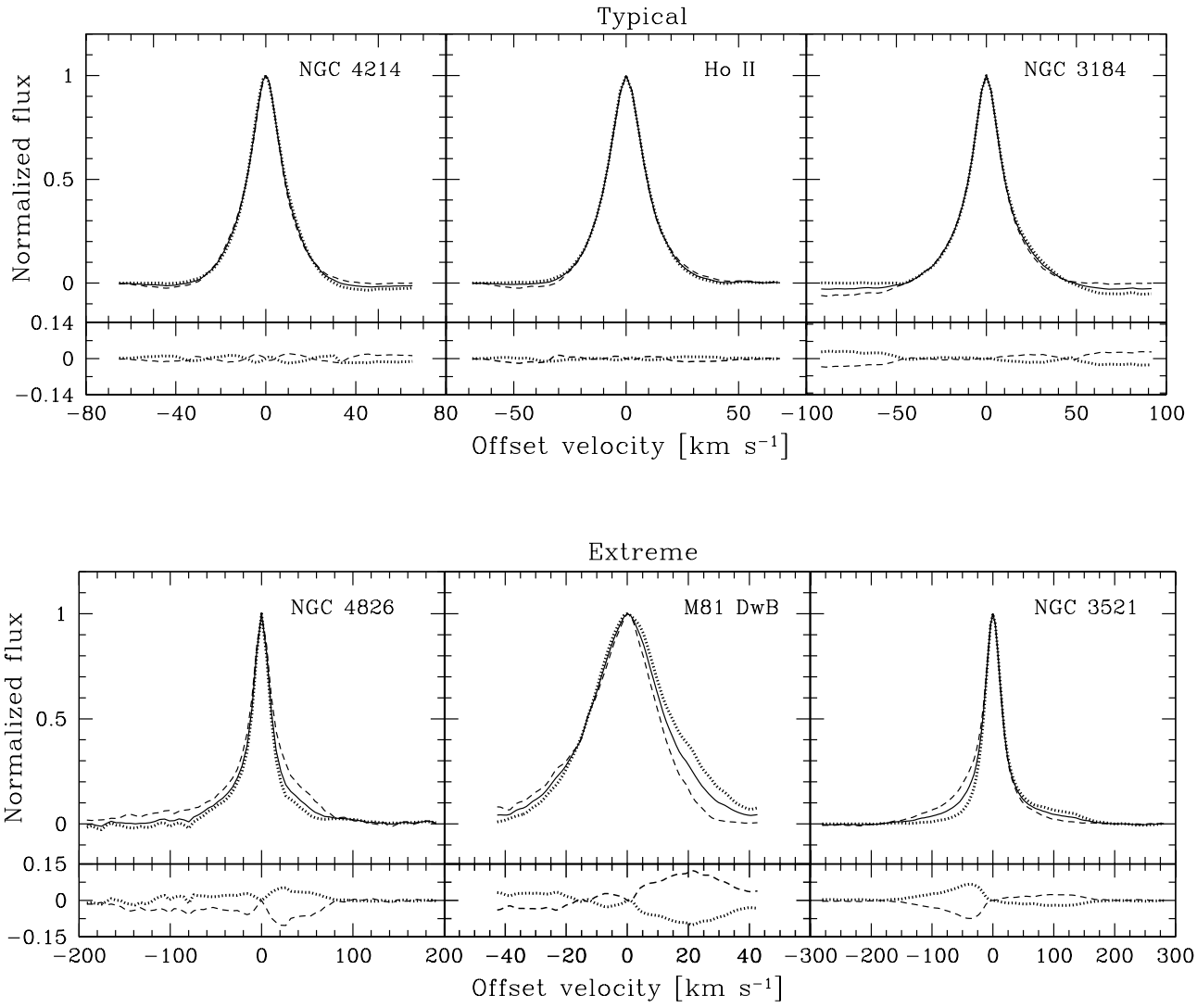

Figure 21: Super profiles extracted from the approaching and receding sides of the galaxies. The super profiles from the two halves of each galaxy are represented as dashed and dotted lines. The overall super profiles are represented by the solid lines. The bottom panels of each plots represent the difference between the super profiles from the two sides and the total super profiles. The super profiles are normalized to their peak values.

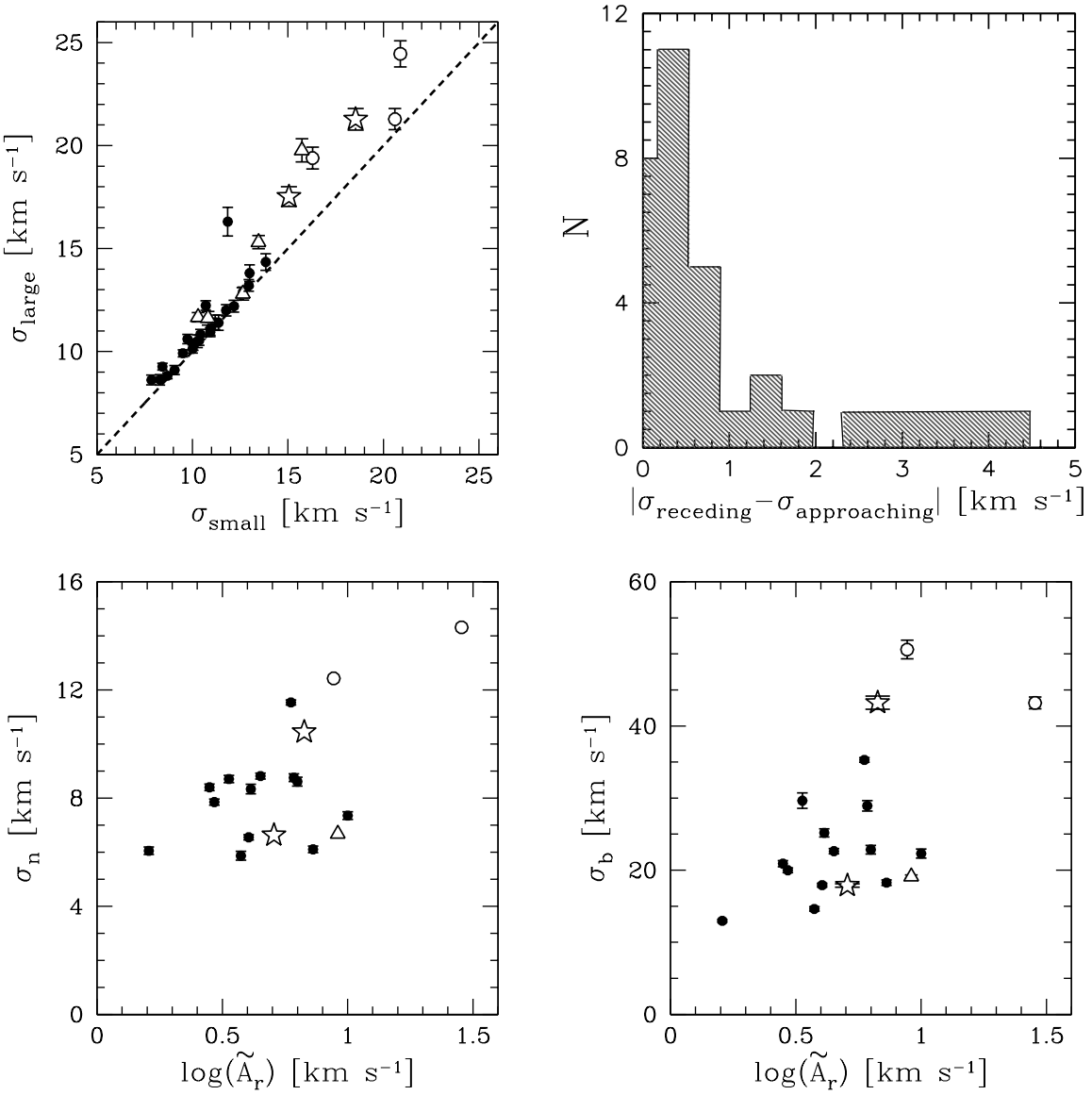

Figure 22: *Top left panel*: Comparison of the widths of the super profiles from the approaching and receding sides of the galaxies. The largest of each of these velocity dispersions is represented by σ_{large} and the smallest one by σ_{small}. The dashed line represents the line of equality.*Top right panel*: Histogram of the difference between the velocity dispersion derived from the approaching and receding halves of the galaxies. *Bottom left panel:* Narrow component velocity dispersion as a function of the amplitudes of non-circular motions, $\tilde{A}$, derived by Trachternach et al. (2008). *Bottom right panel:* Broad component velocity dispersion as a function of $\tilde{A}$. Note that only the 18 galaxies that are part of Trachternach et al. (2008) sample are shown here. Symbols are as in Figure 16.

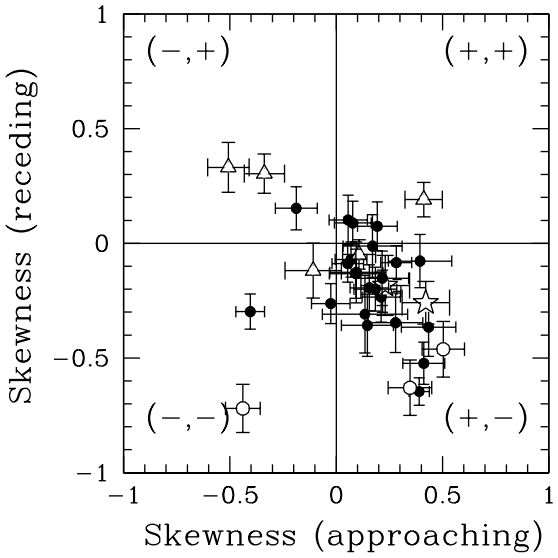

Figure 23: Skewness (defined as $4\sqrt{3}h_3$, where h_3 is the third Gauss-Hermite polynomial coefficient) of the super profiles derived from the receding and approaching side of each galaxy. The two outlying galaxies in the lower left quadrant are DDO 53 (top) and NGC 1569 (bottom). The plus and minus signs represent the signs of the skewness parameters. Symbols are as in Figure 16.

3.1.5 Systematic SHUFFLE uncertainties

Choosing the wrong offset velocity in the profile shuffling procedure could artificially broaden super profiles. As the SHUFFLE method as implemented in GIPSY uses velocity field values as input, the type and accuracy of the velocity field used is important as well. To get an idea of the uncertainties in velocity field values in real data, we show in Figure 24 the uncertainties in the central velocity value of the fitted third-order Hermite h_3 profiles of NGC 2403 plotted against the fitted amplitudes (see de Blok et al., 2008). As expected, low amplitude profiles have larger uncertainties. These uncertainties could in principle create an "artificial" broad component in the super profiles. We therefore carry out an experiment to quantify the effect of these uncertainties on the super profiles. We test a case where all profiles have random offsets with respect to their proper "shuffle" values as well as a case where the offsets depend on the amplitude of the spectra. To do this, we create artificial data cubes. The data cubes contain purely Gaussian profiles, which all have 6 km s^{-1} velocity dispersion but with different amplitudes. We use the observed peak flux distribution of NGC 2403 as input probability distribution for our models. We then randomly pick one thousand amplitudes using this distribution and generate Gaussians using these amplitudes and the 6 km s^{-1} constant velocity dispersion. The position along

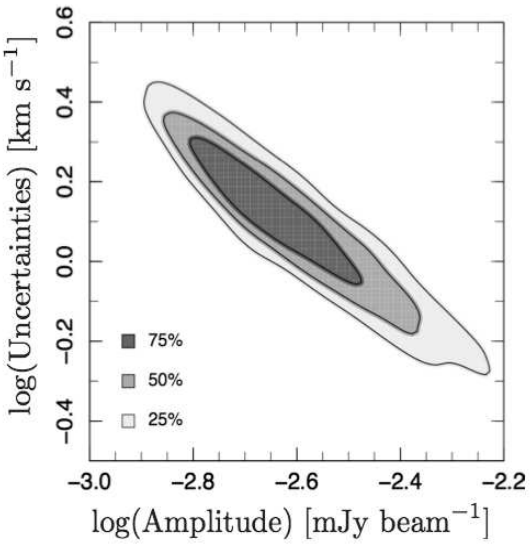

Figure 24: The uncertainties in the central velocity value as derived by fitting a Hermite (h_3) function to the profiles in NGC 2403 plotted against the fitted amplitude of these profiles.

the velocity axis of the model profiles is taken from the observed velocities of the profiles of NGC 2403. We create a data cube using the input spectra described above and derive a velocity field from it, which we refer to as the *true* velocity field. We then add uniform random offsets to the true velocity field and use the modified velocity field to shuffle profiles.

For the first test, we give all the input spectra uniform random offsets (between -5 to 5 km s^{-1}, -10 to 10 km s^{-1}, etc.). For the second model test, only profiles with amplitudes less than 25% of the overall peak amplitude are given uniform random offsets (for the case of NGC 2403, where the maximum profile peak value is 9.2 mJy, this value corresponds to 2.3 mJy). Larger amplitude profiles are assumed to have zero offset.

Figure 25 (left panel) shows examples of super profiles derived from the first set of model cubes. The super profiles get broader as we increase the offsets but the two components retrieved by the double Gaussian fitting are all similar in amplitude and dispersion. In other words, there are *no* broad and narrow components. The results of a single Gaussian fit to the simulated super profiles show that at [-5, 5] km s^{-1} offsets, the resulting broadening due to incorrect shuffling is about 1 km s^{-1}. At [-10, 10] km s^{-1}, this increases to $\sim$ 3 km s^{-1}. At [-15, 15] km s^{-1} offsets, the width of the resulting super profiles is twice as large as the width of the input profiles. At [-20, 20] km s^{-1} offsets, the super profiles start to have double peaked features.

Table 6
Velocity dispersions derived from simulated super profiles using different offsets

Offsets	uniform			amplitude dependent		
(km s^{-1})	σ_{1G} (km s^{-1})	σ_n (km s^{-1})	σ_b (km s^{-1})	σ_{1G} (km s^{-1})	σ_n (km s^{-1})	σ_b (km s^{-1})
-5, 5	7.1	6.5	6.7	6.6	6.1	6.7
-10, 10	9.2	7.1	7.2	6.9	6.2	7.6
-15, 15	11.9	8.0	7.8	7.3	6.1	9.4
-20, 20	15.0	8.8	9.3	7.3	6.1	11.4
-25, 25	···	···	···	7.3	6.2	14.6
-30, 30	···	···	···	7.2	6.2	18.5

Note. — *(Column 1)*: Range of offsets. *Column 2-4*: Derived dispersions using the offset range given in Col. 1 as applied to all profiles. *Column 5-7*: Derived dispersions using the offset range given in Col. 1 as applied only to profiles with an amplitude less than 2.3 mJy. σ_{1G} denotes the velocity dispersion derived from a single Gaussian fitting; σ_n the velocity dispersion of the narrow component and σ_b the velocity dispersion of the broad component.

Figure 25 (right panel) shows examples of super profiles derived from the second model cube. We start to clearly see a broad component resulting from incorrect shuffling at [-15, 15] km s^{-1} offsets. The wings of the simulated super profiles get more and more pronounced with increasing offsets. We summarize in Table 6 the velocity dispersion of the super profiles derived from the two tests.

The above results show that we need an offset of at least 15 km s^{-1} to explain the non-Gaussianity of super profiles by incorrect shuffling. As Figure 24 shows, the maximum uncertainties in the fitted amplitudes are around 5 km s^{-1}. This is three times smaller than the offset required to create a broad component. At [-5, 5] km s^{-1} offsets, i.e., equal to the maximum uncertainty in the real data, the broadest of the two components required in the double Gaussian fitting has a velocity dispersion of ~ 6.7 km s^{-1} at these offsets. Thus, we introduce a broadening of only $\sim 10\%$ to the broad component by going from 0 to [-5, 5] km s^{-1} offsets. Obviously, as this is the maximum uncertainty in the data, the real broadening is likely to be much smaller.

Uncertainties in the SHUFFLE procedure are not sufficient to create the broad component that we see in our super profiles. The offsets required to create a broad component are much larger than inferred for real data.

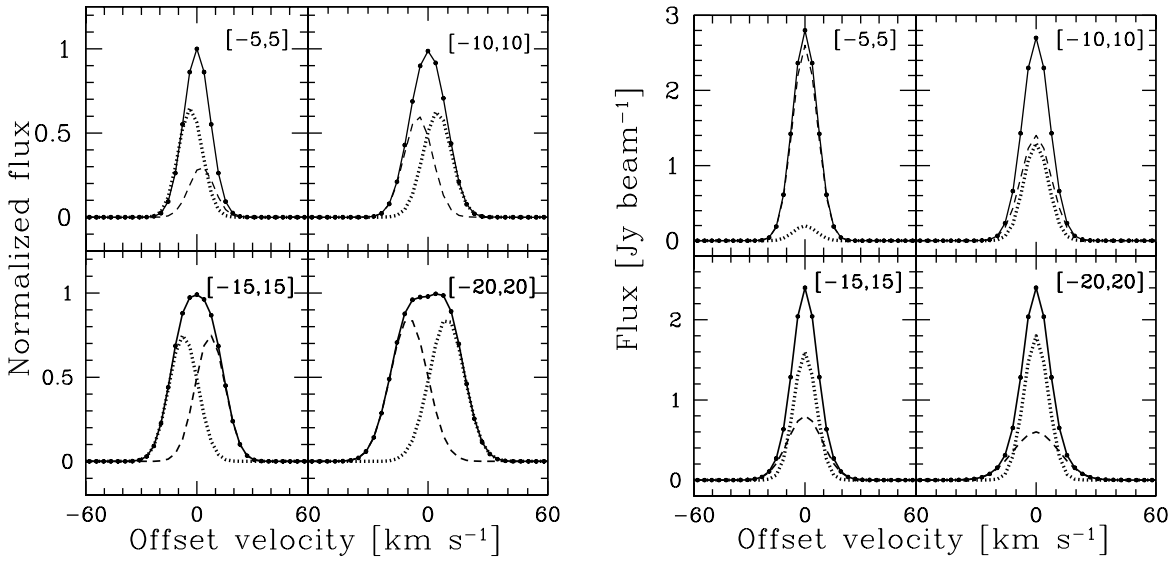

Figure 25: Examples of simulated super profiles derived by giving all input spectra (left panel) and low amplitude spectra (right panel) uniform random offsets. The dotted and the dashed lines represent the narrow and broad components required in the double Gaussian fitting. The solid black lines represent the results from the double Gaussian fitting.

3.2 Selecting a subsample

Here we identify a sample of galaxies that is mostly unaffected by systematic effects or major bulk motions. Figure 26 shows the measured super profile velocity dispersions plotted against the inclinations of the THINGS galaxies. We see a narrow relation with galaxies with higher inclinations having broader profiles (as also shown for these galaxies in Leroy et al., 2008 and Tamburro et al., 2009). Many of the galaxies that do not follow the relation (NGC 1569, NGC 5194, NGC 2841, NGC 3627, NGC 3521, and NGC 7331) are known to be affected by strong sources of turbulence or bulk motion (such as interaction with other galaxies or starbursts). These galaxies are marked with different symbols in Figure 26. One thing to note is the remarkable constancy of the σ_n/σ_b ratio. The weighted average value of this ratio is 0.37 ± 0.04.

Based on inspection of Figures 18, 19, 22, 23 and 26, we exclude from our subsequent analysis galaxies that do not follow the observed trend between inclination and velocity dispersion in Figure 26. We also exclude galaxies where the difference in velocity dispersion measured for the approaching and receding sides, or PA+90° and PA+270° sides is more than 1.5 km s^{-1}. Interacting galaxies will also not be considered. Based on these criteria, we are left with 22 galaxies which we identify as our clean

sample. Their super profiles are expected to be less dominated by the various effects presented earlier. In summary, for these 22 galaxies, the combined effects of the finite channel spacing, the limited spatial resolution and the inclination contribute about 15% of the derived velocity dispersions. Uncertainties due to the inaccurate shifting of the profiles are expected to be at most 10%. In addition, to minimize the effects of individual input profiles on the resulting super profiles (as the sum of a negatively skewed and a positively skewed profile will be one with broader wings and a narrower peak than a Gaussian profile), we selected only symmetrical profiles to construct super profiles. To select symmetrical profiles, we created masks based on the difference between the third-order Hermite (HER3) velocity field values and intensity-weighted mean first moment values (IWM). The former trace the velocity of the peak of the profile, the latter the intensity-weighted mean value. For asymmetric profiles there will therefore be a difference between the HER3 and the IWM values. For symmetrical profiles the difference between the HER3 and IWM is small, and this can be used to efficiently select symmetrical input profiles. We found that the mask where the difference in velocity between the HER3 and IWM is 5 km s^{-1}, can be used to select only very symmetrical profiles to create super profiles. Going smaller than this value will result in a decreased number of input profiles and thus a decreased S/N. When we used this criteria, the resulting super profiles are still well-described by the sum of a narrow and broad Gaussian components, which convincingly show that the shapes of the super profiles are intrinsic.

3.3 Super profiles from the entire disk of galaxies

In this section, we describe the shapes of the super profiles derived from the entire disk of the selected 22 galaxies presented in the previous section. Figure 27 shows the distribution of the narrow, the broad and the single Gaussian components velocity dispersions. The narrow component has a much tighter distribution than the broad component, with mean values of 5.7 ± 1.3 km s^{-1} and 12.6 ± 2.5 km s^{-1}, respectively. The single Gaussian velocity dispersion has a mean of 8.7 ± 1.3 km s^{-1}. Our mean single Gaussian velocity dispersion value can be compared with the mean second moment map velocity dispersion value found by Leroy et al. (2008) for the THINGS galaxies with inclination less than 60°. Leroy et al. (2008) found a mean velocity dispersion of 11 ± 3 km s^{-1}, which is higher than our mean single Gaussian velocity dispersion value. The difference is due to the fact that unlike the single Gaussian velocity dispersions, the second moment velocity dispersions are sensitive to the wings of the profiles. In other words, the second moment velocity dispersions include the contribution of the broad component.

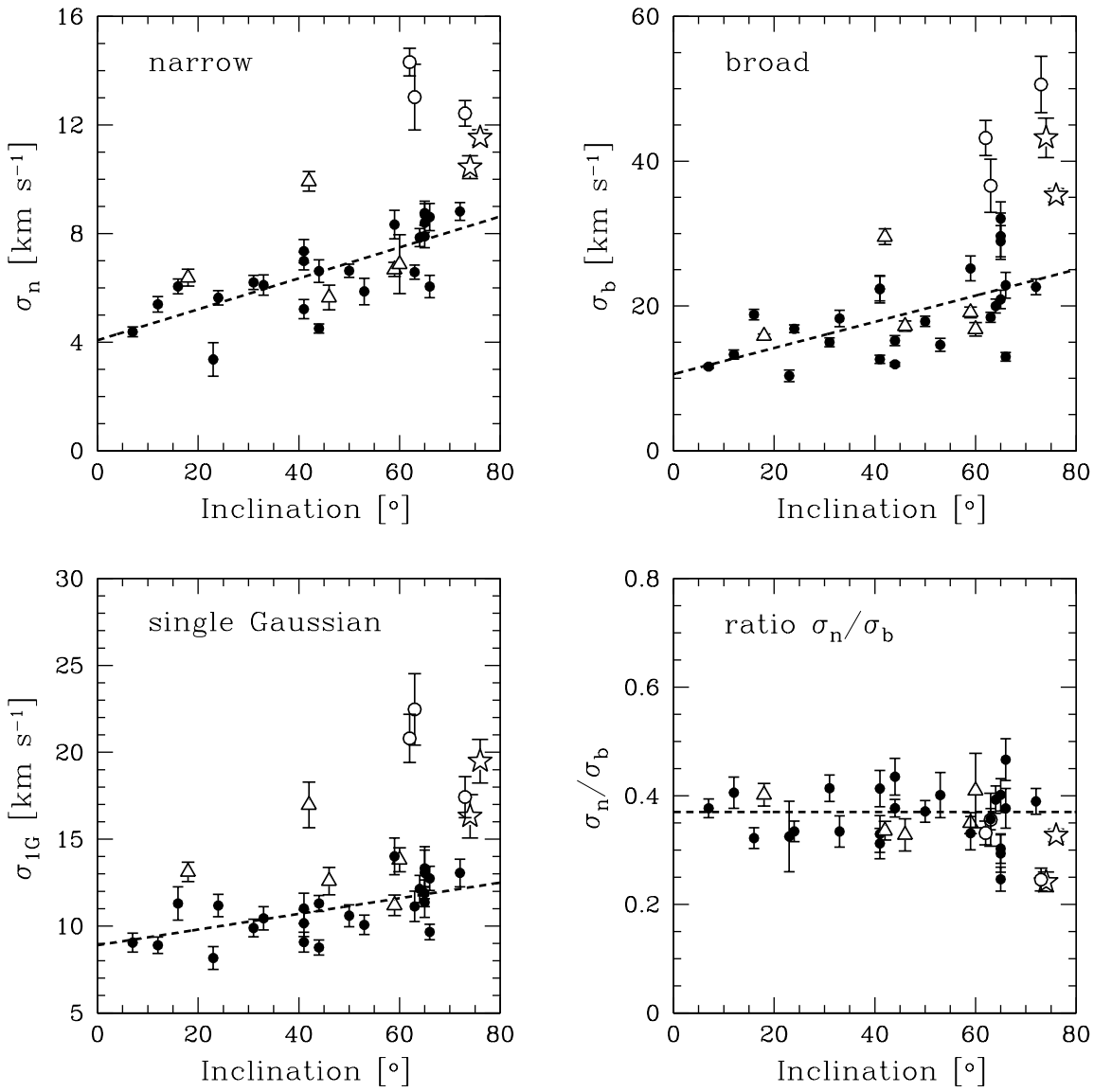

Figure 26: Relation between inclination and measured velocity dispersion. All error bars are 3 σ error bars. The top left panel is for the narrow component. The top right panel is for the broad component and the bottom left panel is for the single Gaussian component. The dashed lines are linear least squares fit with slopes of 0.045±0.014 for the single Gaussian component, 0.057±0.010 for the narrow component and 0.18±0.05 for the broad component. Note that only the filled data points were used in these fits. The bottom right panel is a plot of the ratio of the narrow and broad component velocity dispersions against inclination. The dashed line represents the weighted average value of $\sigma_n/\sigma_b \backsimeq$ 0.37±0.04. Symbols follow Figure 16.

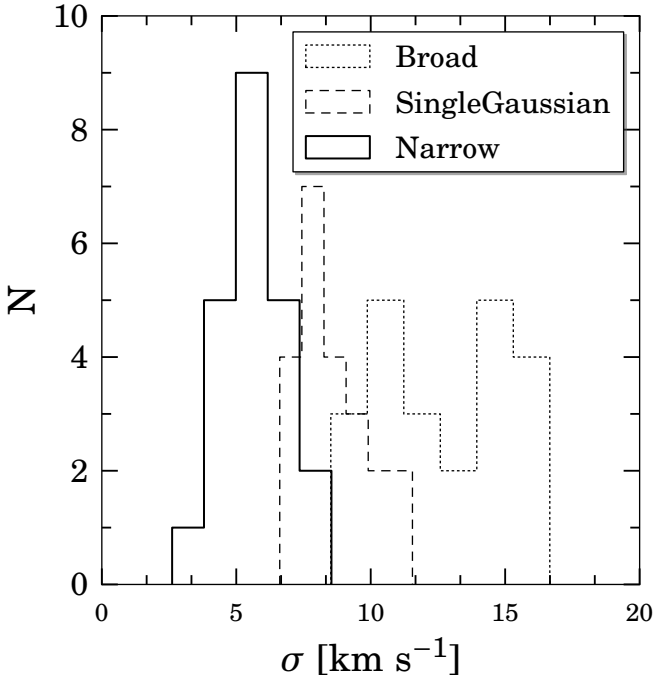

Figure 27: *Solid line*: histogram of the narrow component velocity dispersion; *dotted line*: histogram of the broad component velocity dispersion; dashed line: histogram of the single Gaussian velocity dispersion.

We separate our sample into dwarfs and spirals to see if the shapes of the super profiles depend on galaxy morphology. We adopt the definition of spirals and dwarfs given in Leroy et al. (2008). They define dwarfs as galaxies with rotation velocities $V_{rot} \leq 125$ km s^{-1}, stellar masses $M_* \lesssim 10^{10}\ M_\odot$, and absolute B magnitude $M_B \gtrsim -20$ mag. Galaxies more massive than this are defined to be spirals. For the dwarfs, we find a mean narrow component velocity dispersion of 5.4 ± 1.3 km s^{-1}, a mean broad component velocity dispersion of 11.7 ± 2.2 km s^{-1} and a mean single Gaussian velocity dispersion of 8.6 ± 1.1 km s^{-1}. For the spirals, we find a mean narrow component velocity dispersion of 6.1 ± 1.3 km s^{-1}, a mean broad component velocity dispersion of 13.7 ± 2.4 km s^{-1} and a mean single Gaussian velocity dispersion of 8.7 ± 1.5 km s^{-1}. We thus find that the velocity dispersions of spirals and dwarfs are identical within the uncertainties. The A_n/A_b ratios differ though. We find a mean A_n/A_b of 0.45 ± 0.21 and 0.78 ± 0.24 for the dwarfs and spirals, respectively. This indicates the larger importance of the narrow component (the CNM) in spirals. We summarize the fitted parameters of our sample galaxies' super profiles in Table 7.

Table 7
Fitted parameters derived from the entire disk of galaxies

Galaxy	σ_{1g} (kms^{-1})	σ_n (kms^{-1})	σ_b (kms^{-1})	A_n/Ab	% A_n [%]
1	2	3	4	5	6
DDO 53	8.8 ± 0.1	5.6 ± 0.0	11.8 ± 0.0	0.39 ± 0.01	27
DDO 154	8.3 ± 0.0	4.6 ± 0.0	9.4 ± 0.0	0.16 ± 0.0	13
Ho I	8.0 ± 0.1	4.8 ± 0.0	10.4 ± 0.0	0.33 ± 0.01	24
HoII	7.8 ± 0.1	5.0 ± 0.0	10.6 ± 0.1	0.46 ± 0.01	31
IC 2574	8.3 ± 0.1	5.1 ± 0.0	10.9 ± 0.0	0.37 ± 0.01	27
M81 dwA	7.3 ± 0.1	2.6 ± 0.1	8.5 ± 0.1	0.09 ± 0.0	8
NGC 628	6.6 ± 0.1	4.2 ± 0.0	9.1 ± 0.1	0.47 ± 0.01	32
NGC 925	9.7 ± 0.1	6.8 ± 0.0	14.6 ± 0.1	0.71 ± 0.02	41
NGC 2366	10.9 ± 0.1	7.1 ± 0.1	14.2 ± 0.1	0.42 ± 0.01	29
NGC 2403	8.2 ± 0.1	5.6 ± 0.0	11.3 ± 0.0	0.59 ± 0.01	37
NGC 2903	10.4 ± 0.1	7.0 ± 0.1	16.5 ± 0.1	0.72 ± 0.02	41
NGC 2976	10.4 ± 0.1	7.8 ± 0.0	16.1 ± 0.1	0.92 ± 0.02	47
NGC 3184	7.6 ± 0.1	5.1 ± 0.0	11.9 ± 0.1	0.63 ± 0.02	38
NGC 3198	11.6 ± 0.1	8.5 ± 0.1	16.7 ± 0.1	0.82 ± 0.02	44
NGC 3351	7.3 ± 0.1	5.7 ± 0.0	12.7 ± 0.1	1.18 ± 0.03	54
NGC 3621	9.6 ± 0.1	7.1 ± 0.0	15.4 ± 0.1	0.93 ± 0.03	48
NGC 4214	7.2 ± 0.1	4.4 ± 0.0	10.2 ± 0.1	0.46 ± 0.01	31
NGC 4736	8.3 ± 0.1	6.1 ± 0.0	14.2 ± 0.1	1.04 ± 0.03	51
NGC 5055	9.7 ± 0.1	7.0 ± 0.0	15.2 ± 0.1	0.84 ± 0.02	45
NGC 5236	8.2 ± 0.1	4.6 ± 0.1	10.8 ± 0.1	0.33 ± 0.01	24
NGC 6946	7.9 ± 0.1	5.3 ± 0.1	14.5 ± 0.3	0.81 ± 0.04	44
NGC 7793	9.0 ± 0.1	5.8 ± 0.0	12.9 ± 0.1	0.52 ± 0.01	34

Note. — Column 1: Name of galaxy; Column 2: velocity dispersions derived from the single Gaussian fit; Column 3: velocity dispersions of the narrow component; Column 4: velocity dispersions of the broad component; Column 5: A_n/A_b ratio; Column 6: fraction of the narrow component's flux with respect to the total flux. Spiral galaxies (adopting the definition of Leroy et al. 2008) are marked in bold; the rest are dwarf galaxies (using the same definition).

3.4 Super profiles and global galaxy properties

In the following, we explore possible correlation between global galaxy properties and super profile shapes. If the narrow and broad components identified here are related to the CNM and the WNM phases of the ISM, we expect some correlation between these two components and tracers of star formation. For example, Schaye (2004) suggests that the transition from the warm to the cold phase of the ISM triggers disk instabilities which eventually leads to star formation. We use FUV-NUV colors, Hα luminosities and metallicities as star formation indicators. The FUV-NUV colors are drawn from J. C. Lee et al. (2011) or else Muãoz-Mateos et al. (2009). The FUV-NUV colors have been corrected for galactic extinction. Emission in the UV arises from O and later-type B stars and therefore traces star formation over a timescale of $\lesssim$ 100-200 Myrs. The Hα luminosities are taken from R. C. Kennicutt et al. (2008). Emission in Hα is mainly caused by hot stars such as O and early-type B stars which are massive and short lived. Thus, Hα emission is a tracer of recent star formation over a timecale of $\lesssim$ 10 Myrs. This timescale is roughly comparable to the time it takes for the WNM to cool (e.g. Wolfire et al., 2003). The metal abundance is taken from Moustakas et al. (2010) or alternatively from Table 1 of Walter et al. (2008). Moustakas et al. (2010) used both empirical (Pilyugin and Thuan, 2005) and theoretical (Kobulnicky and Kewley, 2004) calibrations to compute gas-phase abundances. Here we use the average values of the characteristic (globally averaged) metallicities of the two calibrations listed in Table 9 of Moustakas et al. (2010). As discussed in Moustakas et al. (2010), the abundance is likely to be underestimated by up to $\sim$0.2-0.3 dex in the empirical calibrations and overestimated by a similar amount in the theoretical calibrations. Thus, taking the average values of the two calibrations is expected to yield an abundance estimate that is close to the "true" value. Metallicity plays an important role in cold phase formation (Krumholz et al., 2009; Schaye, 2004; Walch et al., 2011) as gas can be cooled, for example, via collisional excitation of heavy elements such as oxygen.

The relationship between the super profile parameters and these different star formation indicators are presented below. We plot in Figure 28 the velocity dispersion ratio (σ_n/σ_b) and the A_n/A_b ratio of the narrow and broad components as a function of metallicities, (FUV-NUV) colors and Hα luminosities.

We find a moderate correlation of the velocity dispersion ratio with metallicity with a correlation coefficient $R \sim -0.60$. In principle this could reflect more efficient cooling, but as turbulence must also play a large role in determining the value of the velocity dispersion, it is more likely that this trend is a reflection of a metallicity-star formation rate relation. High metallicity galaxies tend to have

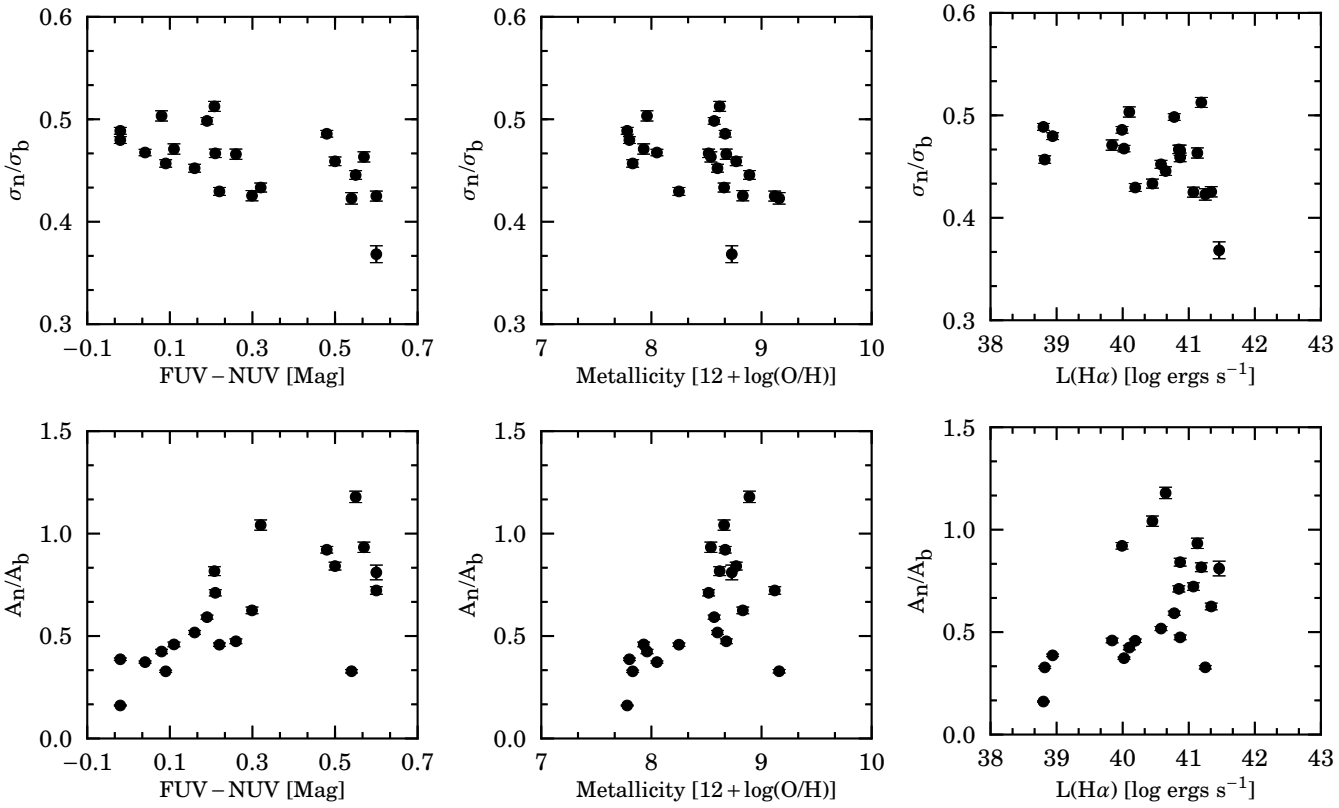

Figure 28: *Top panel*: velocity dispersion ratio as a function of metallicity, FUV-NUV colors, and Hα luminosities. *Bottom panel*: flux ratio of the narrow and broad components as a function of metallicity, FUV-NUV colors, and Hα luminosities.

higher star formation rates, and for these high star formation rate (high metallicity) galaxies, the broad component velocity dispersion is likely to be larger which will give a lower σ_n/σ_b.

The σ_n/σ_b ratio tends to be higher for bluer (FUV-NUV) colors; the correlation coefficient is $R \sim -0.66$. As low metallicity galaxies are on average also bluer in (FUV-NUV), this relation probably reveals similar information as the metallicity *vs* σ_n/σ_b relation. There is only a weak correlation between dispersion ratio and Hα luminosities ($R \sim -0.20$). This weak correlation may be due to the fact that the super profile parameters and the Hα luminosities have not been derived from the same regions within the galaxies.

In terms of the A_n/A_b ratio, which should measure the amount of cold gas (CNM) relative to warm gas (WNM), we find that the fraction of the narrow components relative to the broad components tends to be high for high metallicity galaxies ($R \sim 0.53$). We find similar relations in terms of (FUV-NUV) colors and Hα luminosities with correlation coefficients $R \sim 0.53$ and $R \sim 0.47$, respectively. These correlations are all preliminary indications that the presence of cold gas is associated with star formation.

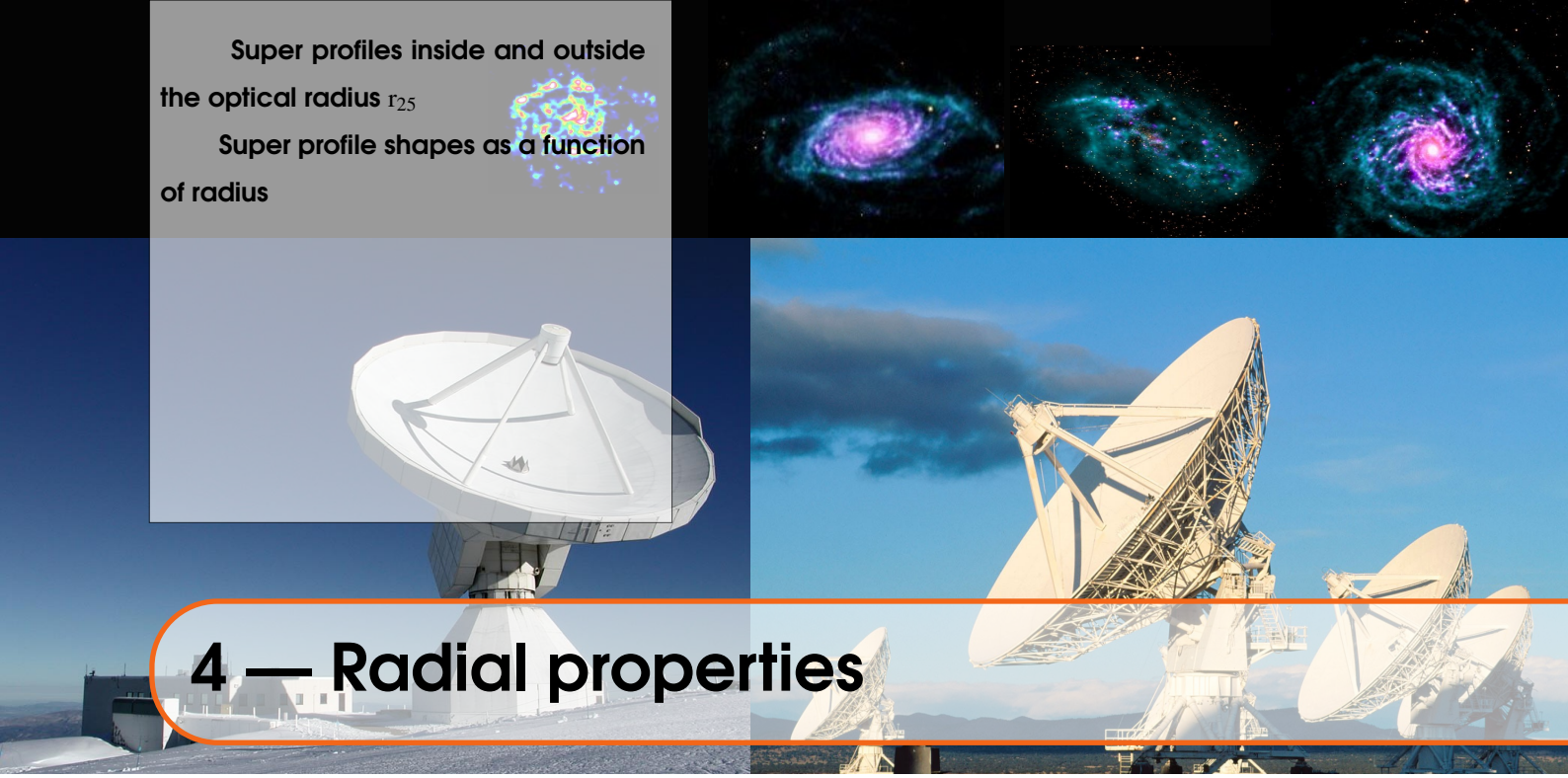

4 — Radial properties

In this chapter, we investigate the radial properties of the shapes of the super profiles. Earlier work has also reported on this. For example, Kamphuis and Sancisi (1993) fitted a single Gaussian function to the HI velocity profiles of NGC 6946, a relatively face-on spiral galaxy, and found that the derived HI velocity dispersions decrease with radius from $\sim$ 13 km s^{-1} to $\sim$ 6 km s^{-1}. Their position-velocity map along the major-axis of NGC 6946 shows faint extended emission of gas moving at velocities of up to 100 km s^{-1} with respect to the systemic velocity. This gas component is seen as wings in the velocity profiles of NGC 6946 and is dominant in the optical disk (r_{25}) of the galaxy but becomes less prominent outside r_{25}. Petric and Rupen (2007) also investigated the shapes of HI velocity profiles for NGC 1058. By fitting a single Gaussian function to the profiles, they found that the derived HI velocity dispersions decrease with radius from $\sim$ 11 km s^{-1} to $\sim$ 6 km s^{-1}. Braun (1997) analyzed the HI emission spectra of 11 nearby spiral galaxies at a resolution of $\sim$ 150 pc and found filamentary structures forming a so-called *High Brightness Network* (HBN). This HBN has a narrow line core with a velocity full width at half maximum (FWHM) of less than $\sim$ 6 km s^{-1} superposed on broad Lorentzian wings having a velocity FWHM extending up to $\sim$ 30 km s^{-1}. The HBN contains about 60% - 90% of the total HI flux within r_{25} but becomes less dominant or disappears in the outer disk. A simple radiative transfer modelling of the HBN indicates that its kinetic temperature increases with radius. Braun (1997) attributed the HBN to the Cold Neutral Medium (CNM) phase of the ISM.

In a recent study, Tamburro et al. (2009) analyzed the HI profiles of 11 face-on and intermediately inclined galaxies from THINGS with the aim of understanding the physical mechanisms that determine

the linewidth of the profiles. Tamburro et al. (2009) used the second-moment values along the line of sight as tracers of the random motion of gas in the galaxies. These values decrease with radius from $\gtrsim 20$ km s^{-1} to ~ 5 km s^{-1}. Tamburro et al. (2009) also reported that their sample exhibits a characteristic velocity dispersion value of 10 ± 2 km s^{-1} at r_{25}. By comparing the predicted energy input from different physical mechanisms with the gas kinetic energy inferred from the observed linewidth of the profiles, they concluded that star formation is the dominant mechanism that determines the width of the profiles inside r_{25}. Outside this radius, ultra-violet (UV) heating from extragalactic sources or magneto-rotational instability (MRI) were proposed to be likely candidates that set the width of the profiles.

The shapes of HI velocity profiles are largely influenced by the local conditions within galaxies. Different form of energies through stellar winds, supernovae explosions, magnetic fields are constantly injected to the ISM and their effects on the HI medium can be investigated by analyzing the shapes of the HI emission velocity profiles. As the environments can be different from one location to another within galaxies, the shapes of the profiles are expected to vary accordingly. Here we will analyze the key parameters that characterize the shapes of the HI velocity profiles as a function of positions in galaxies.

In this chapter, we will derive the HI gas velocity dispersions as a function of radial positions for our sample galaxies. In addition to the velocity dispersion analysis, if the narrow and broad Gaussian components can be associated with the CNM and WNM, then the super profile shapes can be used to address the following questions: *a*) How does the fraction of the CNM vary as a function of radius? *b*) How do the surface densities of the WNM and the CNM vary as a function of radius? *c*) Is the radial profile of the surface density of the CNM similar to that of the molecular gas?

To answer these questions, we investigate the shapes of the super profiles inside the optical radius r_{25}, a region where we expect more star formation, and outside r_{25} where we do not expect much star formation. To complement our studies, we also analyze the shapes of the super profiles as a function of radius. The knowledge of the radial variation of the shapes of the HI velocity profiles are important for theoretical models that explain the source of the turbulent driving mechanisms of the ISM. In addition, the measurement of the gas velocity dispersion as a function of radius is crucial for disk instability analysis. The lack of this measurement has led people to usually assume that the HI gas velocity dispersion is constant with radius (Schaye, 2004). We will show later that the HI gas velocity dispersion varies with radius for most of the analyzed galaxies.

4.1 Super profiles inside and outside the optical radius r_{25}

We use the optical radius, r_{25}, to define the radius of active star formation. This choice is motivated by Figure 29 and Figure 30. In Figure 29 we show, for one galaxy (though the analysis was done for all galaxies) , the cumulative sum of the star formation rate surface density derived by Leroy et al. (2008), Σ_{SFR}, as a function of radius normalized by r_{25}. We have adopted the r_{25} values listed in Table 1 of Walter et al. (2008). We can see that r_{25} corresponds to the radius where Σ_{SFR} has dropped by $\sim$90% (marked by the dashed line). We define the latter radius to be the radius of star formation, r_{SFR}. In Figure 30 we plot r_{25} against r_{SFR}. For about 80% of the galaxies r_{25} corresponds well with the radius for star formation. For galaxies with a centrally concentrated star formation (e.g. NGC 5055, NGC 5236, NGC 2903, NGC 2976 and NGC 4736), r_{25} is roughly 50% greater than r_{SFR}. These galaxies are shown with different symbols in Figure 30. Overall, r_{25} corresponds well to r_{SFR} and given that r_{25} values have been widely used in the literature (e.g. Leroy et al., 2008; Tamburro et al., 2009), we use r_{25} to define the extent of the optical disk.

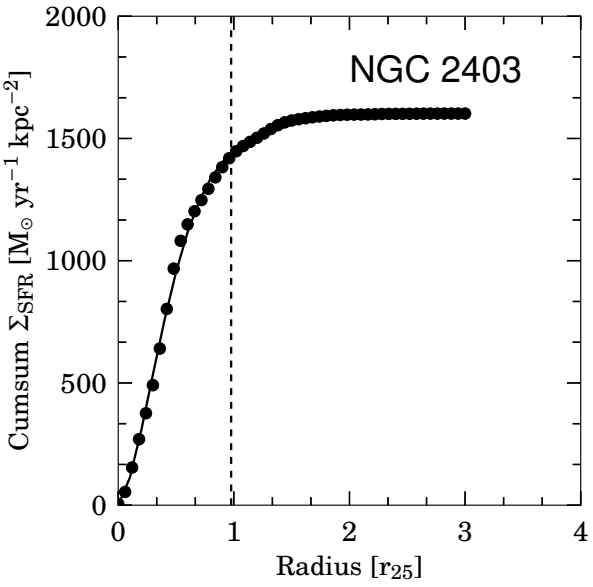

Figure 29: Cumulative sum of star formation rate surface density, Σ_{SFR}, as a function of radius normalized by r_{25}. The dashed line marked the radius where the star formation rate has dropped by 90%.

4.1.1 Velocity dispersion

We compare the velocity dispersions of the narrow and broad components derived inside and outside r_{25} in Figure 31. It is clear that the velocity dispersions derived inside r_{25} tend to be larger than those

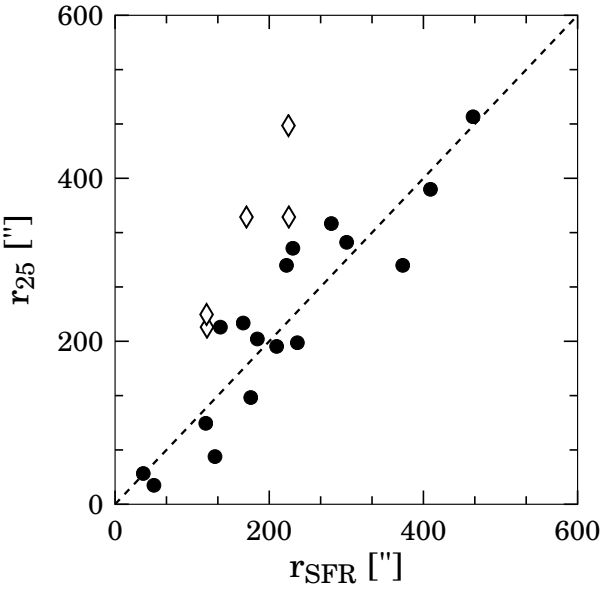

Figure 30: The optical radius r_{25} plotted against the radius of star formation, r_{SFR} (radius where the star formation rate has dropped by 90%). The open diamond symbols represent galaxies with a centrally concentrated star formation (see Section 4.1). The dashed line is the line of unity.

outside r_{25}; with a difference of up to $\sim$2.5 km s^{-1} for the narrow component, $\sim$7.9 km s^{-1} for the broad component, and $\sim$3.8 km s^{-1} for the single Gaussian dispersions. The two galaxies having single Gaussian dispersions that are greater outside than inside r_{25} are DDO 53 and M81 dwA. It is worth noting that the difference between σ^{in}_{r25} and σ^{out}_{r25} tends to be larger for spiral galaxies than for dwarf galaxies. Note that here also we adopt the definition of spirals and dwarfs by Leroy et al. (2008) presented in the previous chapter.

We show in Table 8, the mean velocity dispersions from the single Gaussian fits, as well as the narrow, and broad components derived inside and outside r_{25} separately for the spiral and dwarf galaxies in our sample.

To investigate the cause of the difference between the velocity dispersions derived inside and outside r_{25}, we check the possibility of beam-smearing effects. The expected increase of beam-smearing effects towards the center of galaxies could lead to a larger σ value. If this is the case then we should expect a positive correlation between inclination and $\sigma^{in}_{r_{25}}$ values. We did, however, not find any trend between the two quantities. Moreover, even for a relatively face-on galaxy like NGC 628 (with an inclination of only $\sim 7^{\circ}$), we observe a difference of $\sim$3.5 km s^{-1} between $\sigma^{in}_{r_{25}}$ and $\sigma^{out}_{r_{25}}$. As a further check, we measured the velocity dispersions for $0.2\ r_{25} < r < r_{25}$ thus omitting the inner part where beam smearing is expected to occur (see also Caldú-Primo et al., 2013). We then compared these dispersions

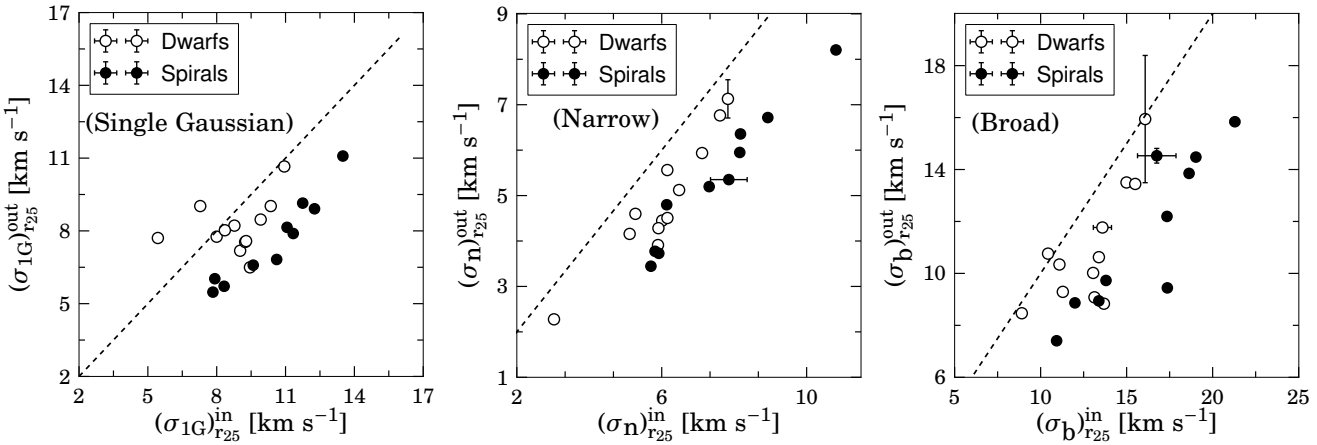

Figure 31: Comparison of the velocity dispersions derived inside and outside the optical radius r_{25}. The dashed lines are lines of equalities.

with $\sigma^{in}_{r_{25}}$. We found no systematic difference between the derived values. A comparison with $\sigma^{in}_{r_{25}}$ results in a slope close to unity and an rms scatter of only $\sim$0.7 km s^{-1} for the single Gaussian and broad components dispersions and $<$0.3 km s^{-1} for the narrow component. Thus, beam-smearing cannot be the main cause of the observed difference between the derived velocity dispersion inside and outside r_{25}.

We now check possible relationship between star formation rate surface density and velocity dispersion. A study by Tamburro et al. (2009) demonstrated that star formation is the main driver of HI velocity dispersion inside r_{25}. Outside this radius, the HI velocity dispersion is thought to be sustained by thermal effects from UV heating (see also Schaye, 2004) or from non-thermal mechanisms such as magneto-rotational instabilities (MRI; Balbus and Hawley, 1991; Sellwood and Balbus, 1999), gravitational instability (Wada et al., 2002), Kelvin-Helmotz, Rayleigh-Taylor instabilities (Shu, 1992), Parker instability (Parker, 1996) or the combined effects of these mechanisms. If the contribution of star formation-driven turbulence is larger than that of the other previously-mentioned mechanisms, as already shown by Mac Low and Klessen (2004), then this can explain the difference between the $\sigma^{in}_{r_{25}}$ and $\sigma^{out}_{r_{25}}$. In Figure 32, we plot $\sigma^{in}_{r_{25}}$ and $\sigma^{out}_{r_{25}}$ as a function of star formation rate surface density, Σ_{SFR}, as derived by Leroy et al. (2008). The Σ_{SFR} was derived from a combination of 24μm and FUV emission maps from the Spitzer Infrared Nearby Galaxies Survey (SINGS; R. C Jr. Kennicutt et al., 2003) and the Galaxy Evolution Explorer Nearby Galaxy Survey (GALEX-NGS; Gil de Paz et al., 2007). The Σ_{SFR}, therefore, traces both obscured and unobscured star formation. Figure 32 shows that the velocity dispersions are more correlated to Σ_{SFR} inside r_{25} than outside this radius. This

Table 8
Average velocity dispersions derived inside and outside r_{25}.

$<\sigma>$ inside r_{25} (km s^{-1})		$<\sigma>$ outside r_{25} (km s^{-1})	
Spirals	Dwarfs	Spirals	Dwarfs
narrow component			
7.5 ± 1.6	6.0 ±1.2	5.4 ± 1.4	4.9 ± 1.3
broad component			
16.1 ± 3.2	12.9 ±2.1	11.5 ± 2.8	11.0 ± 2.2
Single Gaussian			
10.4 ± 1.8	8.8 ±1.4	7.6 ± 1.7	8.1 ± 1.0

confirms previous finding that star formation overwhelms the effects of other physical mechanisms in sustaining the width of HI profiles inside r_{25} (Tamburro et al., 2009). The difference in $\sigma^{in}_{r_{25}}$ and $\sigma^{out}_{r_{25}}$ values can therefore be thought of as the results of the difference in the efficiency of different physical mechanisms to drive turbulence to the HI medium.

4.1.2 Flux or mass ratio

Figure 33 compares the A_n/A_b ratio derived inside and outside r_{25}. The A_n/A_b ratio tends to be larger inside r_{25}. This cannot be due to beam-smearing or bulk motions as they are expected to lower the A_n/A_b ratio. The difference between the A_n/A_b derived inside and outside r_{25} is consistent with the CNM/WNM scenario. Theoretical models (Wolfire et al., 2003) predict the CNM/WNM ratio to decrease as a function of radius due to the decrease in thermal pressure. This has also been confirmed by observations of 11 nearby spiral galaxies by Braun (1997). We summarize the fitted parameters inside and outside r_{25} in Table 9.

4.2 Super profile shapes as a function of radius

Here we investigate the shapes of the super profiles as a function of radius. We derive super profiles within annular ellipses of 0.2 r_{25} width. Note that as discussed by Tamburro et al. (2009), normalizing by r_{25} is similar to normalizing by the optical disk scale length and r_{SFR}.

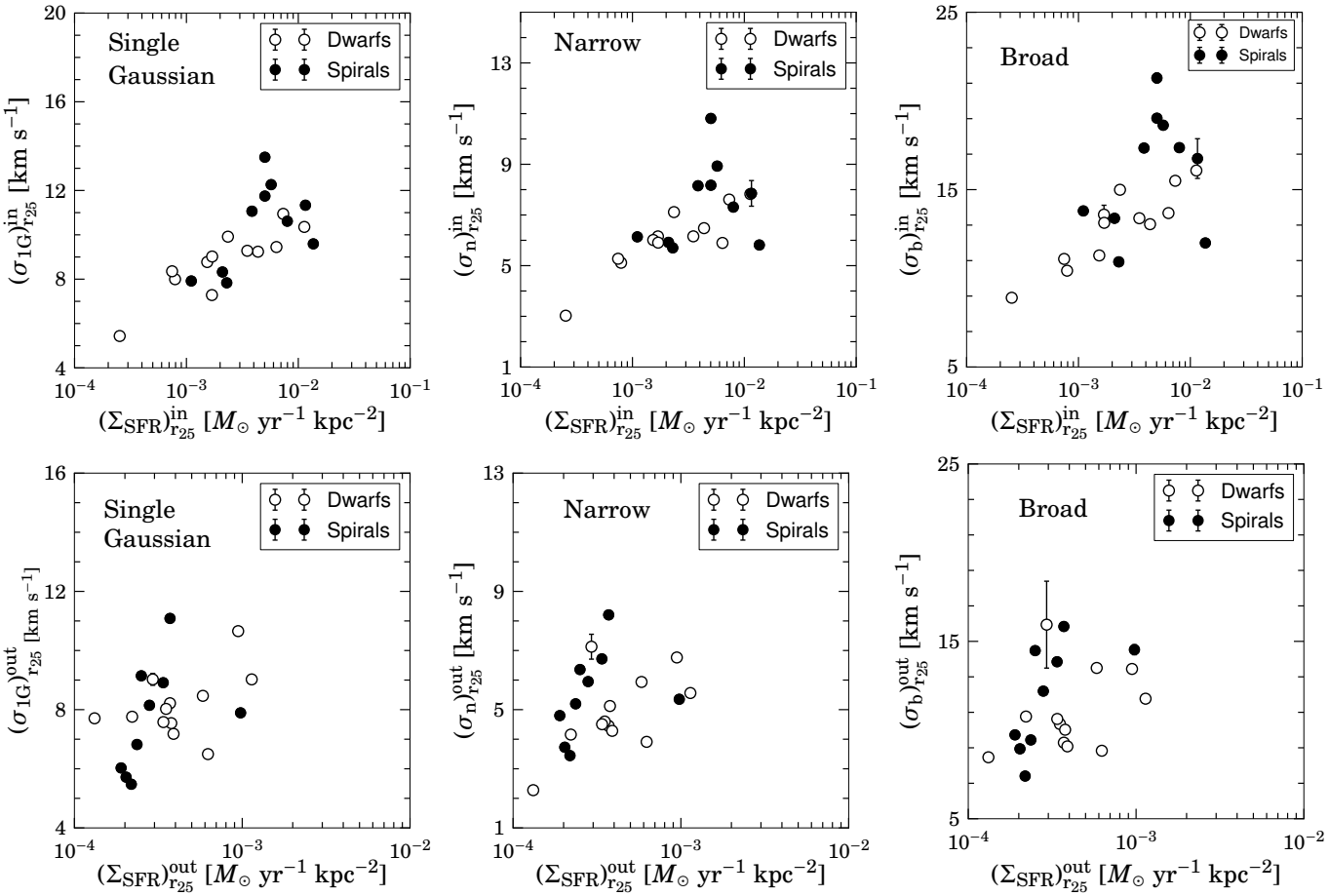

Figure 32: Velocity dispersions derived inside and outside the optical radius r_{25} as a function of star formation rate surface density, Σ_{SFR}, derived in the same radius.

4.2.1 Radial velocity dispersion profiles

Figure 34 shows the single Gaussian, narrow, and broad components velocity dispersions as a function of radius normalized to r_{25}. In most cases, the velocity dispersions decrease exponentially with radius. The single Gaussian velocity dispersion profiles tend to be flatter than that of the narrow and broad components. This behaviour is caused by the broad component becoming more dominant towards the outer disk of the galaxies. For M81 DwA, DDO 53, DDO 154, Ho I, NGC 2976 and NGC 7793, the radial velocity dispersion profiles are relatively flat. These galaxies all fall under our *dwarf* galaxy classification. Galaxies that are classified as spirals exhibit a clear radial decline in velocity dispersions. We fit the radial velocity dispersion profiles with an exponential function of the form $\sigma_0 \exp(-\frac{x}{l})$, where σ_0 is the interpolated value of the velocity dispersion towards the center, and l is the scale length. The results of the fits are shown as dashed lines in Figure 34. With the exception of M81 dwA, DDO 154 and DDO 53, the radial profiles can be well described by the exponential function. Note that the

Table 9
Fitted parameters of super profiles derived inside and outside r_{25}

Galaxy	inside r_{25}					outside r_{25}				
	σ_{1G} (km s^{-1})	σ_n (km s^{-1})	σ_b (km s^{-1})	A_n/A_b	%n (%)	σ_{1G} (km s^{-1})	σ_n (km s^{-1})	σ_b (km s^{-1})	A_n/A_b	%n (%)
DDO 53	7.3 ± 0.0	6.2 ± 0.1	13.6 ± 0.5	1.3 ± 0.21	56	9.0 ± 0.1	5.6 ± 0.0	11.8 ± 0.1	0.32 ± 0.07	24
DDO 154	8.8 ± 0.1	6.0 ± 0.1	11.3 ± 0.1	0.42 ± 0.05	29	8.2 ± 0.0	9.3 ± 0.0	4.4 ± 0.0	0.15 ± 0.02	12
Ho I	8.0 ± 0.1	5.1 ± 0.0	10.4 ± 0.0	0.38 ± 0.01	27	7.8 ± 0.1	4.2 ± 0.1	10.8 ± 0.1	0.29 ± 0.04	22
HoII	9.0 ± 0.1	5.9 ± 0.0	13.1 ± 0.0	0.53 ± 0.02	34	7.2 ± 0.1	4.3 ± 0.1	9.1 ± 0.1	0.31 ± 0.04	23
IC 2574	8.4 ± 0.1	5.3 ± 0.0	11.1 ± 0.0	0.41 ± 0.02	28	8.0 ± 0.1	4.6 ± 0.0	10.3 ± 0.0	0.3 ± 0.01	23
M81 dwA	5.4 ± 0.1	3.0 ± 0.1	8.9 ± 0.2	0.34 ± 0.04	25	7.7 ± 0.1	8.5 ± 0.0	2.3 ± 0.1	0.05 ± 0.04	4
NGC 628	7.8 ± 0.0	5.7 ± 0.0	10.9 ± 0.1	0.69 ± 0.04	40	5.5 ± 0.1	3.4 ± 0.0	7.4 ± 0.0	0.43 ± 0.04	29
NGC 925	9.9 ± 0.1	7.1 ± 0.0	15.0 ± 0.1	0.75 ± 0.04	42	8.5 ± 0.1	5.9 ± 0.0	13.5 ± 0.1	0.7 ± 0.05	41
NGC 2366	10.9 ± 0.1	7.6 ± 0.1	15.5 ± 0.2	0.54 ± 0.06	35	10.7 ± 0.1	6.8 ± 0.1	13.4 ± 0.1	0.34 ± 0.04	25
NGC 2403	9.2 ± 0.1	6.5 ± 0.0	13.1 ± 0.1	0.64 ± 0.03	39	7.5 ± 0.1	5.1 ± 0.0	10.0 ± 0.0	0.5 ± 0.03	33
NGC 2903	11.7 ± 0.1	8.2 ± 0.1	19.0 ± 0.2	0.78 ± 0.06	43	9.1 ± 0.1	6.4 ± 0.0	14.5 ± 0.1	0.74 ± 0.05	42
NGC 2976	10.4 ± 0.1	7.8 ± 0.0	16.1 ± 0.1	0.92 ± 0.04	47	9.0 ± 0.2	7.1 ± 0.4	15.9 ± 2.4	0.78 ± 0.59	43
NGC 3184	8.3 ± 0.1	5.9 ± 0.0	13.4 ± 0.1	0.76 ± 0.04	43	5.7 ± 0.1	3.7 ± 0.0	8.9 ± 0.1	0.6 ± 0.04	37
NGC 3198	13.5 ± 0.1	10.8 ± 0.1	21.3 ± 0.3	1.22 ± 0.12	54	11.1 ± 0.1	8.2 ± 0.1	15.8 ± 0.1	0.79 ± 0.09	44
NGC 3351	7.9 ± 0.1	6.1 ± 0.0	13.8 ± 0.1	1.2 ± 0.06	54	6.0 ± 0.1	4.8 ± 0.0	9.7 ± 0.1	1.21 ± 0.11	54
NGC 3621	12.3 ± 0.1	8.9 ± 0.0	18.6 ± 0.1	0.81 ± 0.04	44	8.9 ± 0.1	6.7 ± 0.0	13.9 ± 0.1	0.96 ± 0.06	49
NGC 4214	9.4 ± 0.1	5.9 ± 0.0	13.7 ± 0.1	0.47 ± 0.02	31	6.5 ± 0.1	3.9 ± 0.0	8.8 ± 0.0	0.39 ± 0.02	28
NGC 4736	10.6 ± 0.1	7.3 ± 0.0	17.4 ± 0.1	0.77 ± 0.04	43	6.8 ± 0.1	5.2 ± 0.0	9.4 ± 0.0	0.82 ± 0.03	45
NGC 5055	11.1 ± 0.1	8.2 ± 0.0	17.3 ± 0.1	0.92 ± 0.06	47	8.1 ± 0.1	5.9 ± 0.0	12.2 ± 0.1	0.8 ± 0.07	44
NGC 5236	9.6 ± 0.1	5.8 ± 0.0	12.0 ± 0.0	0.32 ± 0.01	24	6.6 ± 0.1	3.8 ± 0.1	8.9 ± 0.1	0.36 ± 0.03	26
NGC 6946	11.3 ± 0.2	7.9 ± 0.5	16.8 ± 1.1	0.69 ± 0.39	40	7.9 ± 0.1	5.4 ± 0.1	14.5 ± 0.3	0.81 ± 0.08	44
NGC 7793	9.3 ± 0.1	6.2 ± 0.0	13.4 ± 0.1	0.56 ± 0.02	35	7.6 ± 0.1	4.5 ± 0.0	10.6 ± 0.1	0.41 ± 0.03	28

Note. — σ_{1G}: single Gaussian velocity dispersion. σ_n: narrow component velocity dispersion. σ_b: broad component velocity dispersion. A_n: linestrength (flux) of the narrow component. A_b: linestrength of the broad component. %n: fraction of the narrow component relative to the *total* gas (i.e $A_n/(A_n + A_b)$).

results of the exponential fits depend on the points being fitted. For example, for NGC 4736, NGC 5055 and NGC 2903, the radial decline starts to flatten at about the optical radius. Thus fitting only those points in the inner r_{25} will give a steeper slope. Here we fit the entire radial range.

We compare the scale length of the broad and narrow components in Figure 35. We fit a linear function to this relation and find a slope of $\sim$0.78 and an intercept value of 0.19.

In order to have a more general understanding of the radial decline in velocity dispersion in our sample, we plot, for all galaxies and for dwarfs and spirals, the single Gaussian, narrow and broad component velocity dispersions as a function of radius in Figure 36. We fit the complete set of radial velocity dispersion profiles with a single exponential function. In addition, we try and remove the scatter between individual radial profiles by applying a normalization technique similar to the one presented in Schruba et al. (2011). That is, we normalize the velocity dispersions so that an exponential fit to the profiles has a value of unity at 0.6 r_{25}. Note that the choice of this value is arbitrary. This normalization technique removes galaxy-to-galaxy variation. We also fit the normalized radial velocity dispersion profiles with a single exponential function. The combined radial velocity dispersion profiles before and after normalization are both shown in Figure 36. We see that the radial decline in velocity

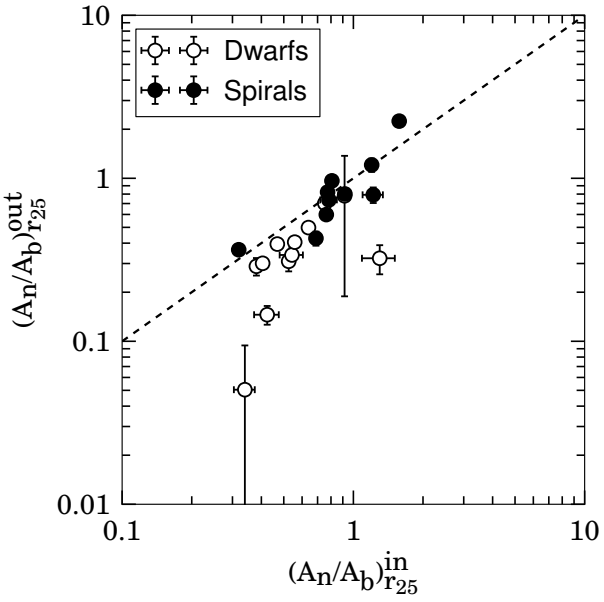

Figure 33: Comparison of the A_n/A_b ratio derived inside and outside r_{25}. The dashed line is a line of unity.

dispersions of spiral galaxies tends to be steeper than that of dwarf galaxies.

Radial dependences of HI velocity dispersions have previously been reported in the literature. Dickey et al. (1990) and Petric and Rupen (2007) studied the HI kinematics of the face-on spiral galaxy NGC 1058 and found a radial decline of HI velocity dispersion from ~ 12 km s^{-1} in the inner part to ~ 6 km s^{-1} in the outer part. Boulanger and Viallefond (1992) and Boomsma et al. (2008) also found a radial fall-off of HI velocity dispersion for the face-on spiral galaxy NGC 6946. As already mentioned, Tamburro et al. (2009) analyzed the radial HI second moment profiles of 11 THINGS galaxies (all but one galaxy are also in our sample), and found that all exhibited a clear radial decline. Our single Gaussian velocity dispersion profiles can be directly compared to those presented in Boomsma et al. (2008) and Tamburro et al. (2009). For NGC 6946, the radial profile from Boomsma et al. (2008) show a steep drop in velocity dispersion followed by a linear decrease from about the optical radius to their outermost observed radius. Our velocity dispersion profile and that from Tamburro et al. (2009), however, shows a continual decline from $\sim 0.7 r_{25}$ to $\sim 1.8 r_{25}$ and then starts to level off. We overplot our single Gaussian velocity dispersion profiles with the second moment velocity dispersion profiles of Tamburro et al. (2009) in Figure 37. In general, we do not find good agreement between our measured velocity dispersions and those from Tamburro et al. (2009) especially in the central parts of galaxies. Here our velocity dispersions tend to be smaller. This can be explained by the fact

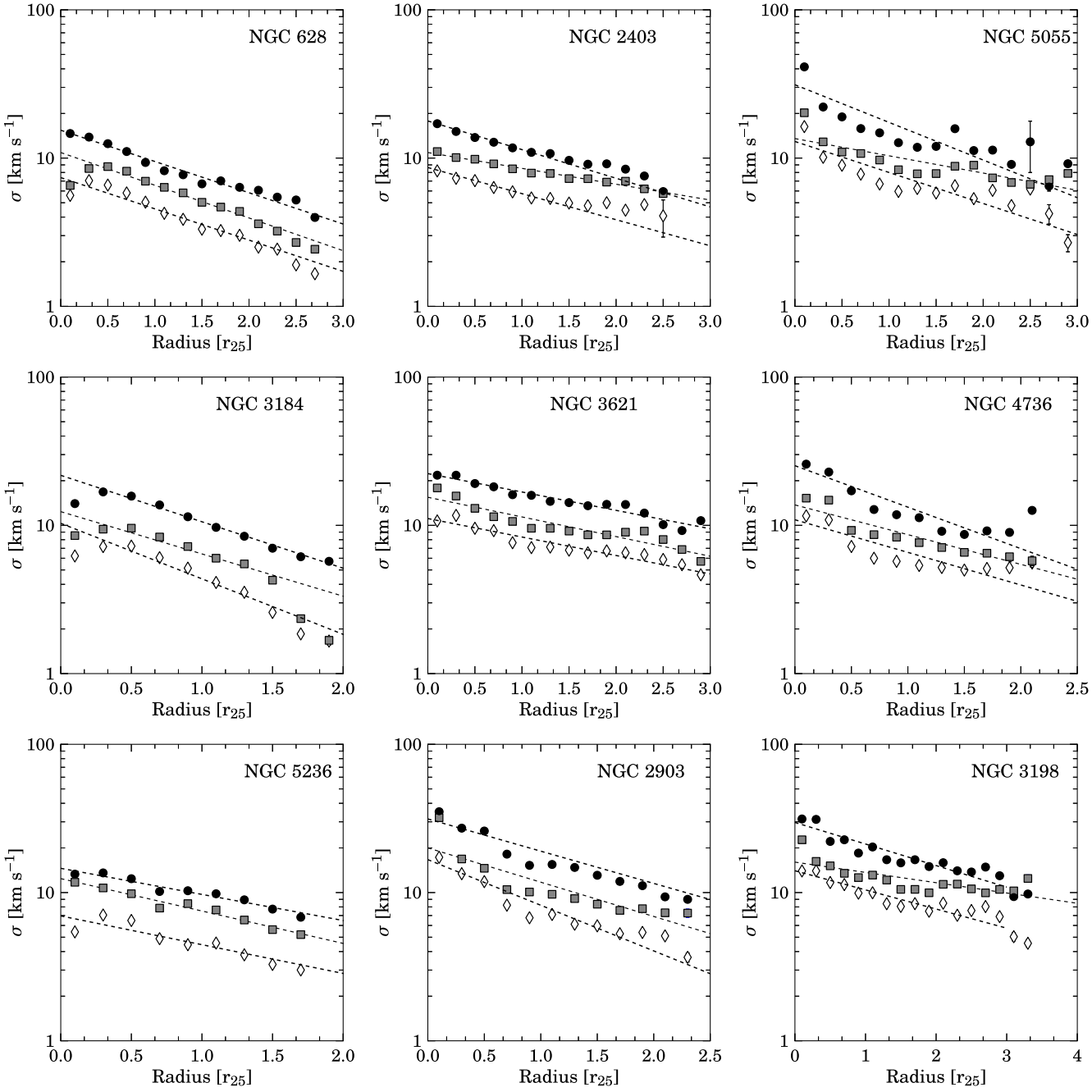

Figure 34: Velocity dispersions as a function of radius normalized to r_{25}. Black solid circle symbols represent the broad component velocity dispersions. The square gray symbols represent the velocity dispersions from the single Gaussian fits and the open diamond symbols show the velocity dispersions of the narrow component. The dashed lines are fits to an exponential function of the form $\sigma_0 \exp(-\frac{x}{l})$.

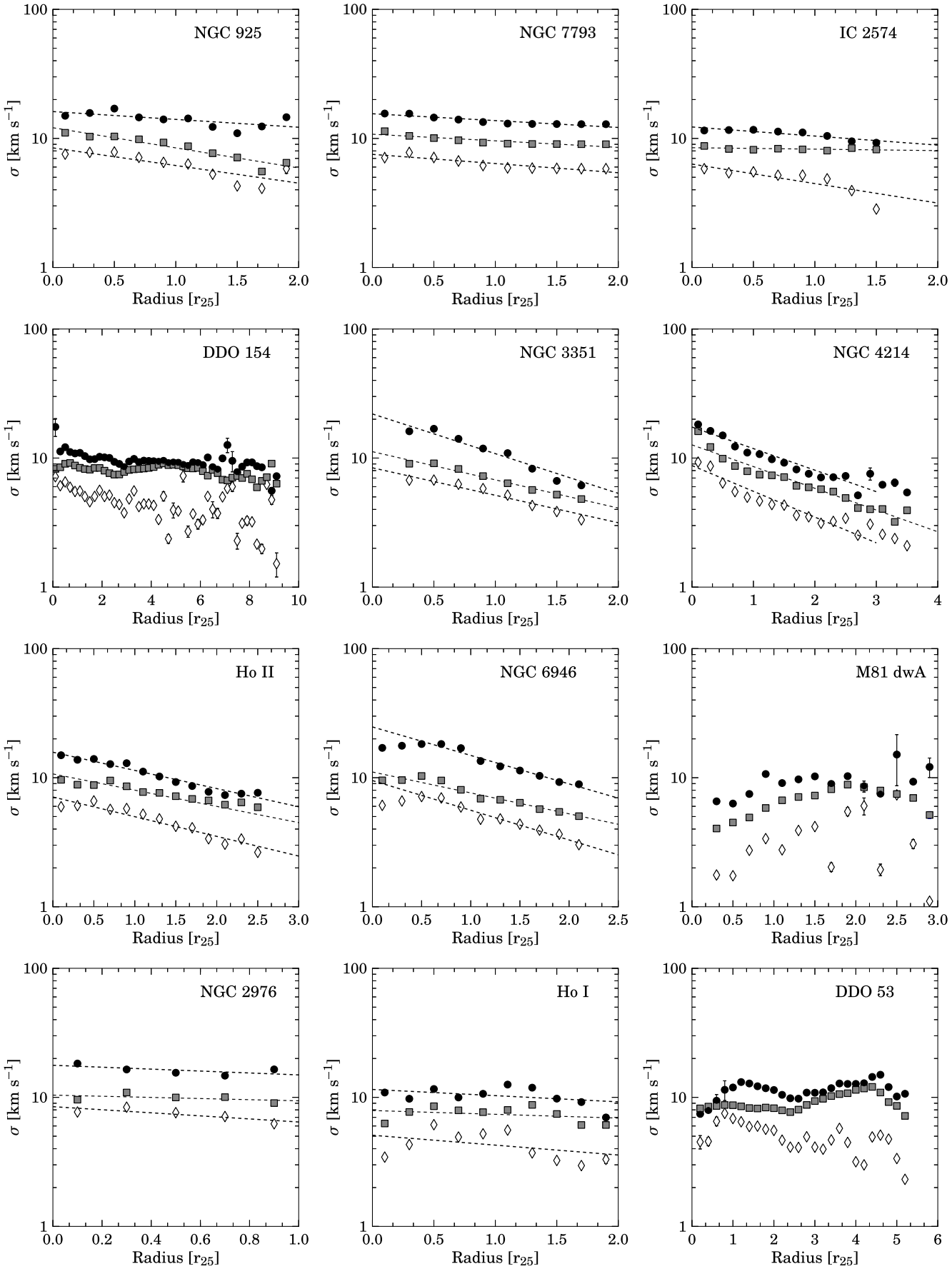

Figure 34: (Continued).

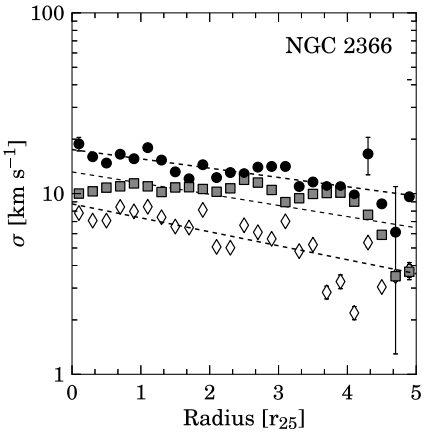

Figure 34: (Continued).

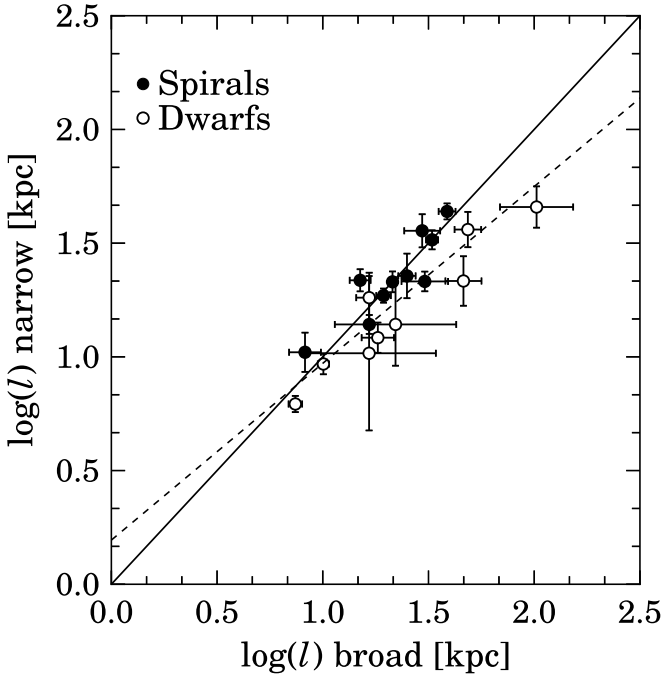

Figure 35: Comparison of the scale length (left panel) of the broad and narrow components. The dashed line is a linear fit to the data points. The solid line represents the line of equality.

that the shapes of the velocity profiles in the inner disk of galaxies are strongly non-Gaussian. For a perfectly Gaussian profile, the second moment velocity dispersion and the single Gaussian velocity dispersion would be equal. However, for a velocity profile with prominent wings, the second moment dispersion would be higher than that of the single Gaussian dispersion. In Figure 37, we also show second moment velocity dispersions calculated from the super profiles. The offset between the single Gaussian dispersions and the second moment dispersions become smaller with increasing radius and for most galaxies the two dispersions start to overlap at a certain radius. This behaviour is due to the shapes of the profiles becoming more and more Gaussian toward larger radius. The overlap radius may indicate the radius beyond which we only expect one component of the HI gas, most likely the WNM. To better understand the behaviour of the second moment velocity dispersion as a function of profile shape, we proceed as follows. We take the fitted super profile of NGC 3184 at $0.3r_{25}$ (this is a typical non-Gaussian super profile with broad and narrow components). We derive a single Gaussian dispersion and a second moment dispersion from it. We then gradually suppress the wings of the profile by decreasing the broad component amplitude while keeping the narrow component parameters fixed. We re-measure the single Gaussian and the second moment dispersions. We do this until the broad component is completely suppressed and we are left with a perfect Gaussian profile. We plot the derived second moment velocity dispersions and single Gaussian velocity dispersions in Figure 38 as a function of the broad component amplitude. As expected, the disagreement between the two kinds of velocity dispersions becomes smaller with decreasing wings strength and they are identical when the profiles are perfect Gaussians. It is also worth noting that the single Gaussian dispersion is very much less affected by the profile wings than the second moment velocity dispersion.

4.2.2 Surface density profiles

We show in Figure 39 the gas surface density as derived from the single Gaussian fits, Σ_{1G}, the surface density derived from the narrow component, Σ_n, and that derived from the broad component, Σ_b, as a function of radius for all galaxies. We fit a single exponential function to the surface density profiles. This is to facilitate comparisons with CO surface density profiles from Schruba et al. (2011). The latter authors fit a single exponential function to the CO surface density profiles of galaxies from the HERACLES sample. Exponential HI surface density profiles were already found before for late-type dwarf galaxies (Swaters et al., 2002). Here, we find that the surface densities can be reasonably explained by the exponential function. The narrow component surface densities tend to decrease faster

than that of the broad component. The single Gaussian surface densities radially decline with a rate somewhere in between the two components. We compare the scale lengths of the narrow and broad component surface density profiles in Figure 40. It is interesting to also compare the radial decline in surface density of the narrow component with that of a tracer of the molecular gas component. Schruba et al. (2011) found that the integrated CO intensities in their sample (a sample of 33 nearby spiral galaxies) decrease exponentially with a scale length of $\sim 0.2\ r_{25}$. This is much steeper than we find for the surface density of the narrow components. Apparently, the colder the gas components the steeper their radial decline in surface densities. We also compare the surface density scale lengths from the single Gaussian fits, the narrow and broad components with the velocity dispersion scale lengths in Figure 41. They show a moderate positive correlation, with $R \sim 0.50$ for the single Gaussian fits, $R \sim 0.73$ for the narrow component and $R \sim 0.66$ for the broad component. The correlation between the surface density scale length and the velocity dispersion scale length indicates correlation between the velocity dispersion and the local HI surface density. Figure 41 shows that spiral galaxies have a better one-to-one correlation than dwarf galaxies for both the narrow and broad components. Dwarf galaxies also seem to correlate but show an offset from the one-to-one line. We show in Figure 42 the surface densities of the narrow and broad components as well as the ratio between the two quantities, Σ_n/Σ_b, as a function of radius for the individual galaxies. The Σ_n/Σ_b ratio tends to decrease with radius for most galaxies. In a similar analysis, Braun (1997) found that the fractional line flux of the HBN mentioned previously (which was attributed to the CNM) decreases abruptly near the optical radius, r_{25}. However, only about 20 % of our sample galaxies show an abrupt decrease in the Σ_n/Σ_b near the optical radius. For most galaxies, the Σ_n/Σ_b ratio continually decline with radius without a clear break. Although we attempted to fit the super profiles with the sum of a Gaussian and a Lorentzian function, similar to what Braun (1997) did, we still did not reach the same conclusion as the latter author. Braun (1997) found that the HI velocity profiles of his sample galaxies are well described by a narrow Gaussian core (with FWHM $\lesssim 6\ km\ s^{-1}$) superposed on broad Lorentzian wings with a FWHM of up to 30 $km\ s^{-1}$. However in our Gaussian plus Lorentzian fitting, the FWHM of the Gaussian component is greater than that of the Lorentzian component. This dissimilarity could be due to the fact that we did not do any opacity corrections and we just fitted the super profiles with the sum of a Gaussian plus Lorentzian function rather than with the physical model assumed by Braun (1997). Investigation of this will be left as future work.

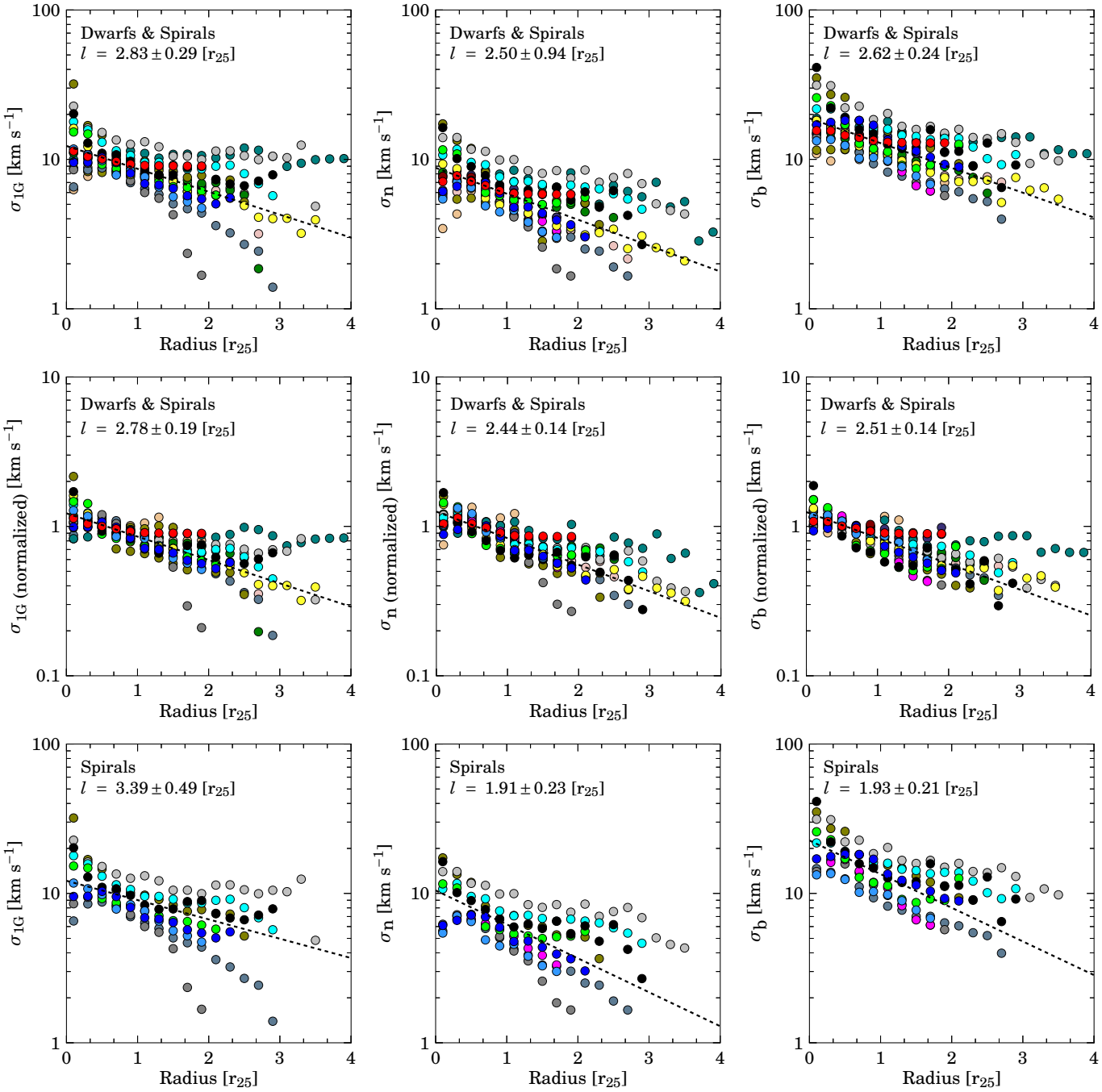

Figure 36: Radial velocity dispersion profiles. Normalized means the velocity dispersions are normalized so that an exponential fit to the radial velocity dispersion profiles is equal to unity at 0.6 r_{25}.

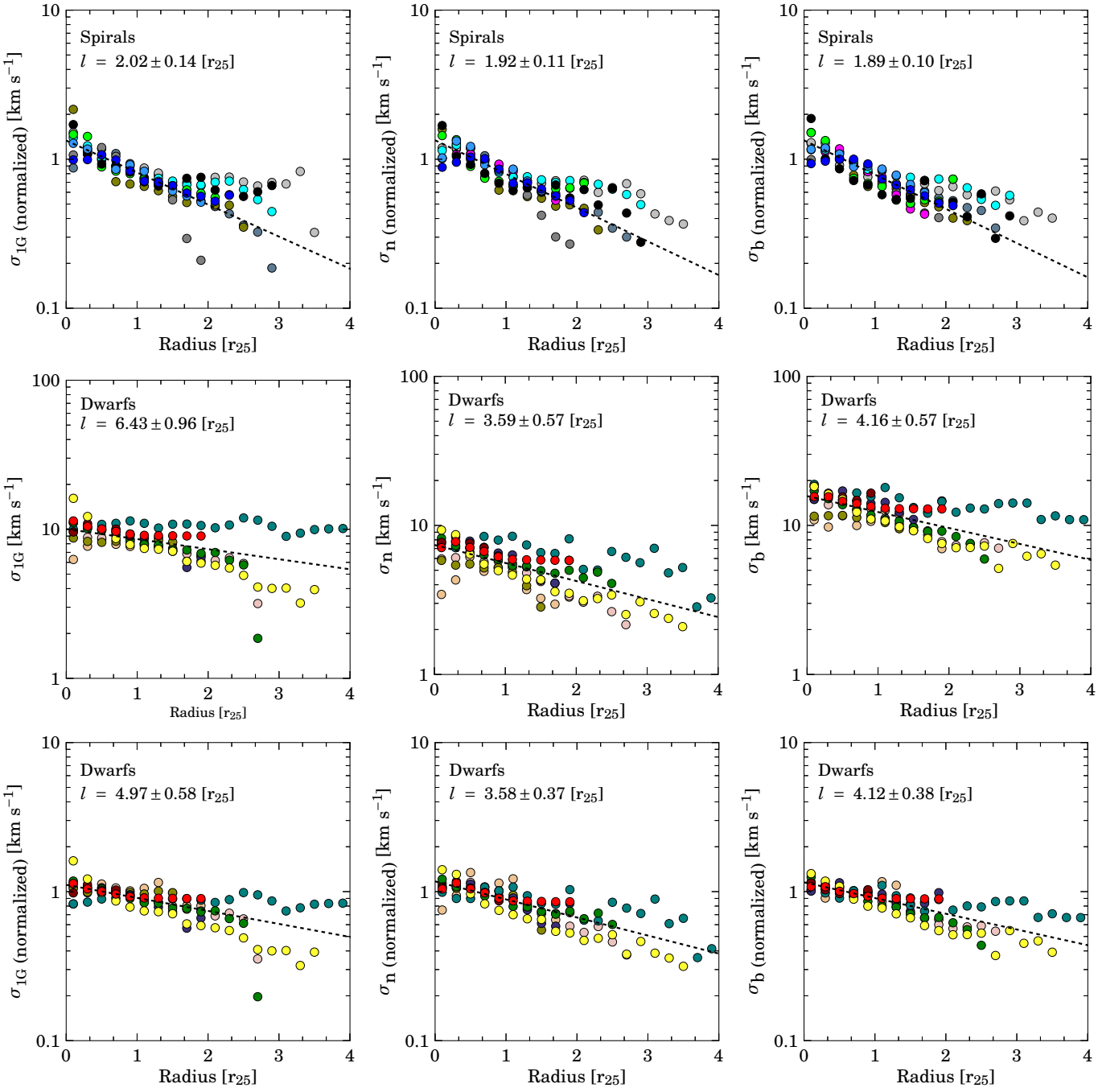

Figure 36: (Continued).

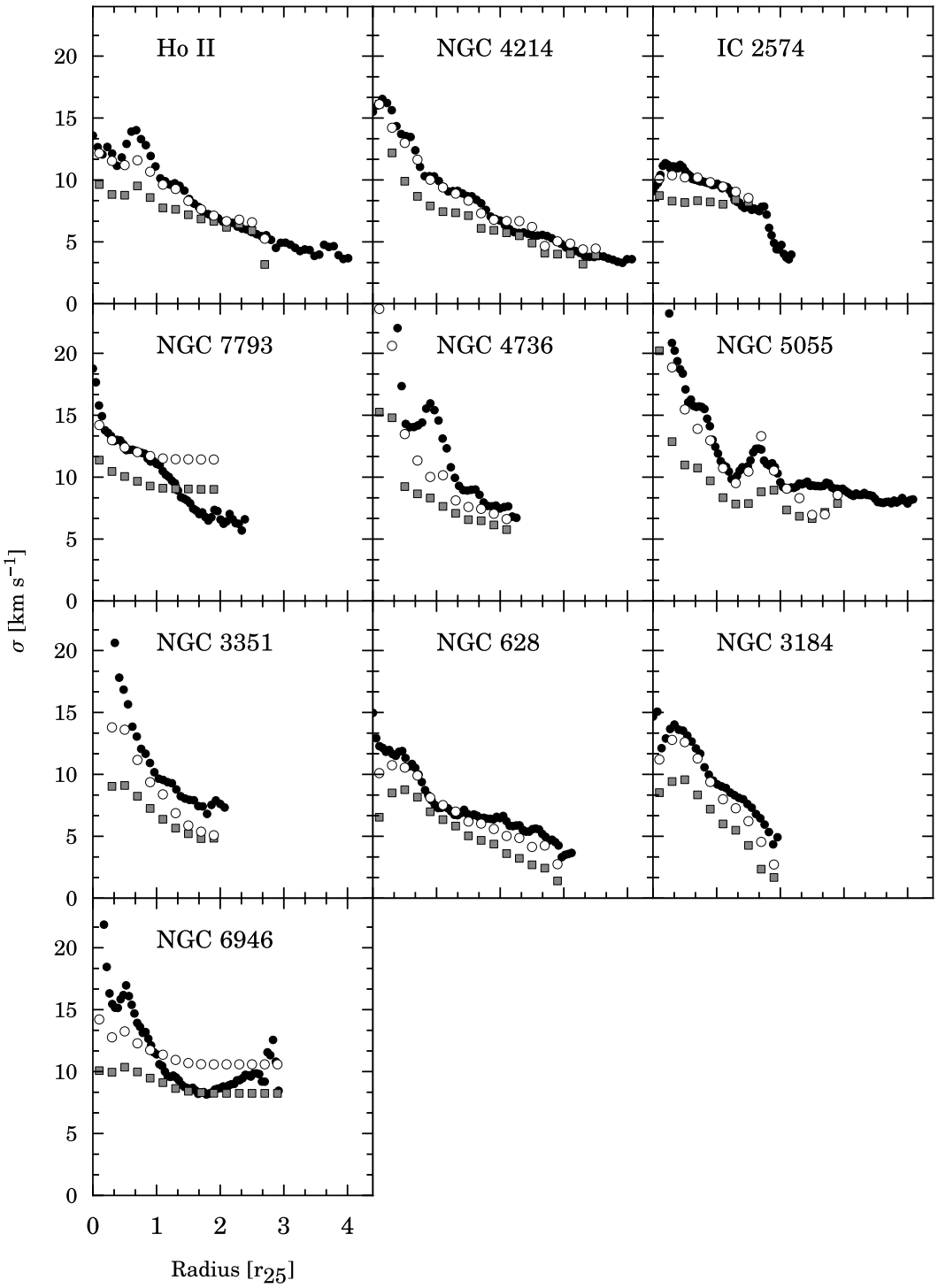

Figure 37: Comparison of velocity dispersions with those derived in Tamburro et al. (2009). The solid black symbols represent the Tamburro et al. (2009) radial velocity dispersion profiles, which were derived from second moment maps. The square symbols are single Gaussian dispersions from our super profiles. The open circle symbols are second moment velocity dispersions calculated from the super profiles.

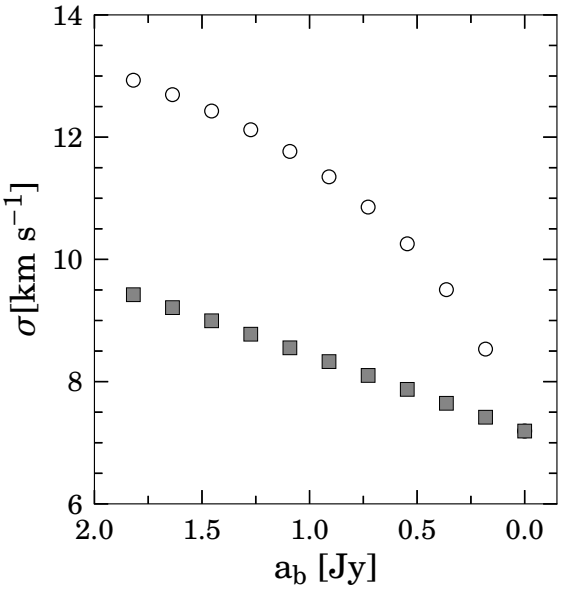

Figure 38: Testing the dependence of single Gaussian and second moment velocity dispersions on the strength of profile wings. Open circle symbols: second moment velocity dispersions. Square symbols: single Gaussian velocity dispersions. a_b: Broad component amplitude.

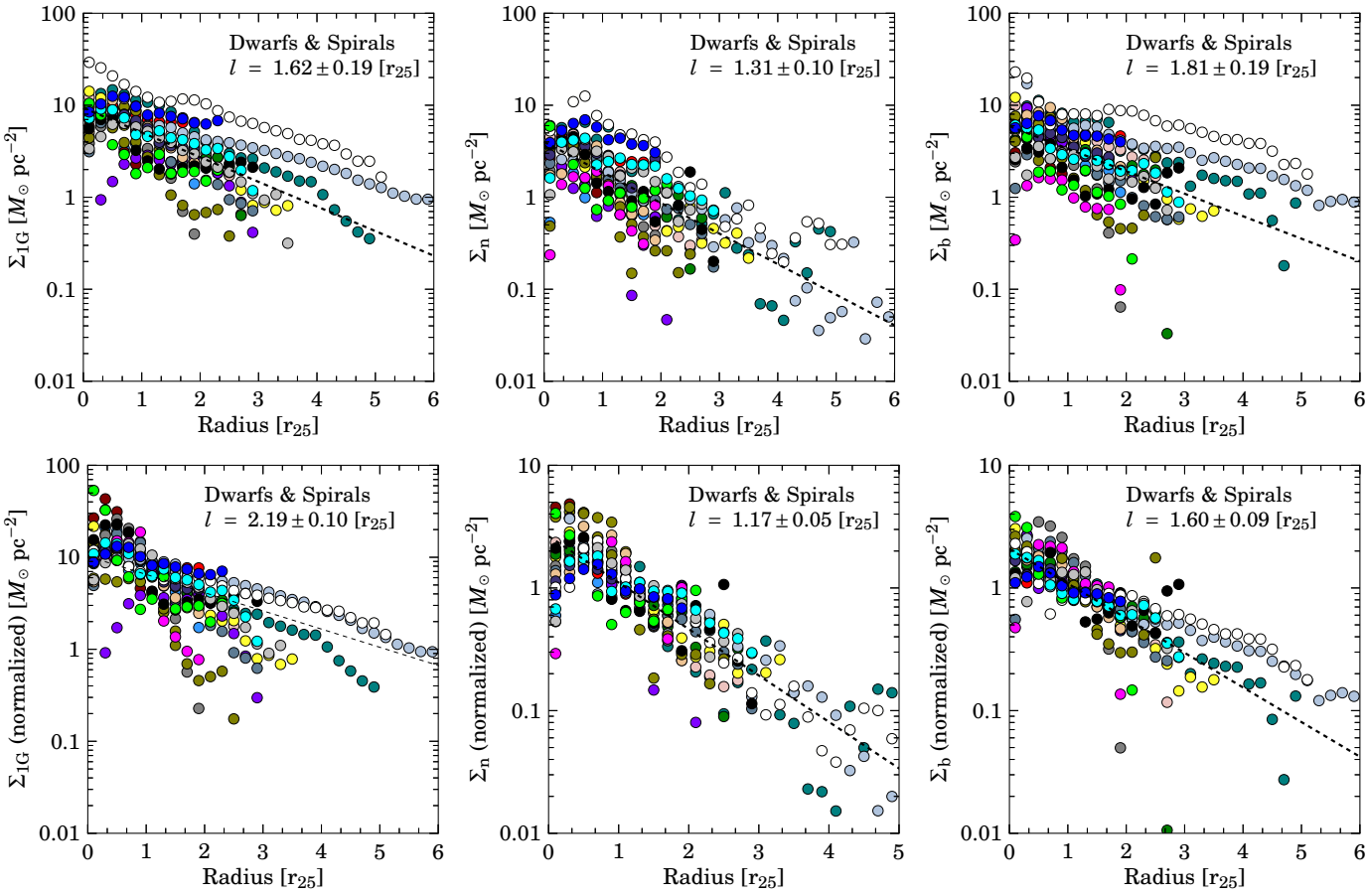

Figure 39: Single Gaussian, narrow and broad component surface densities as a function of radius. In the bottom panels, the surface densities are normalized so that an exponential fit to the radial surface density profiles is equal to unity at r_{25}.

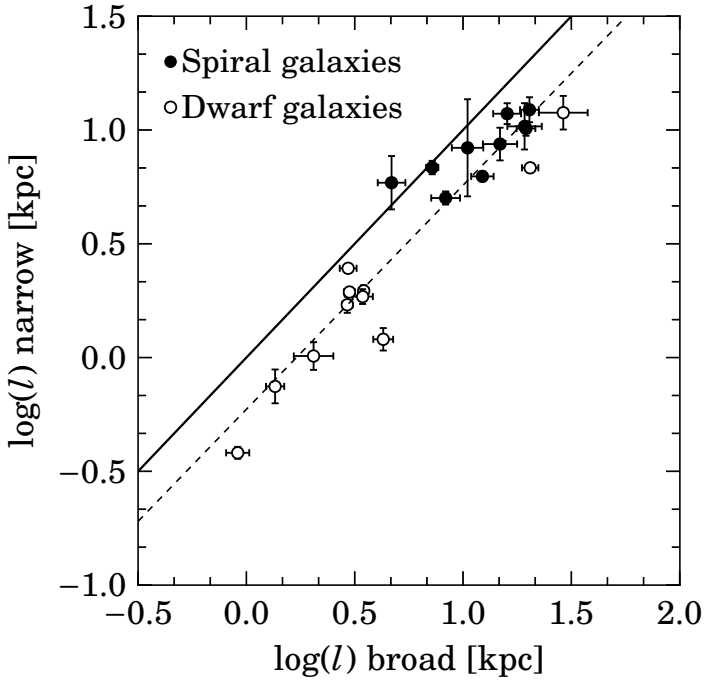

Figure 40: Comparison of the scale lengths derived from the narrow and broad component surface density profiles. The solid line is a line of equality and the dashed line is a linear fit with a slope of 0.98 and an intercept value of -0.23.

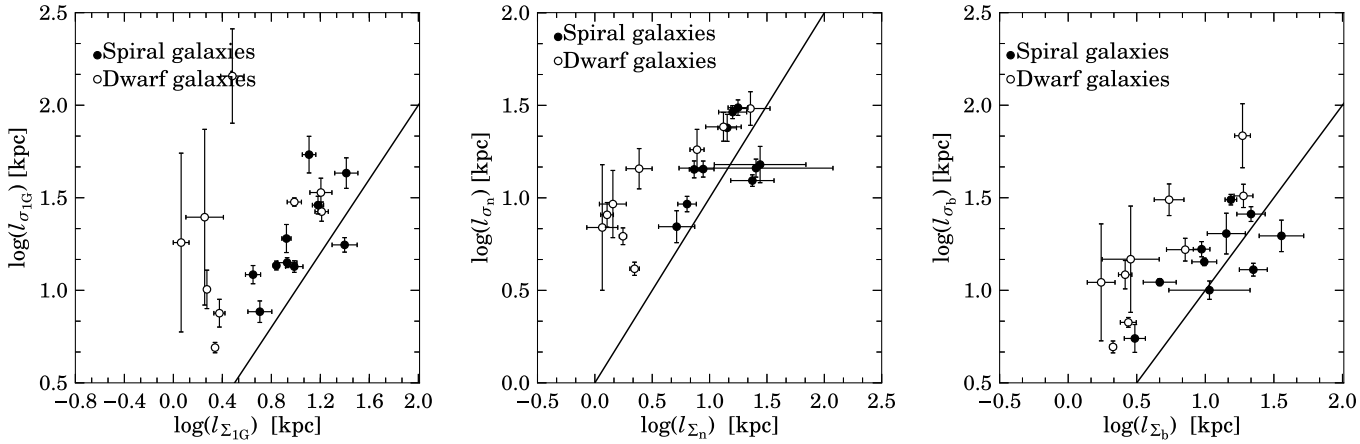

Figure 41: Comparison of the surface density scale lengths with the velocity dispersion scale lengths of the single Gaussian (left panel), narrow (middle panel) and broad (right panel) components.

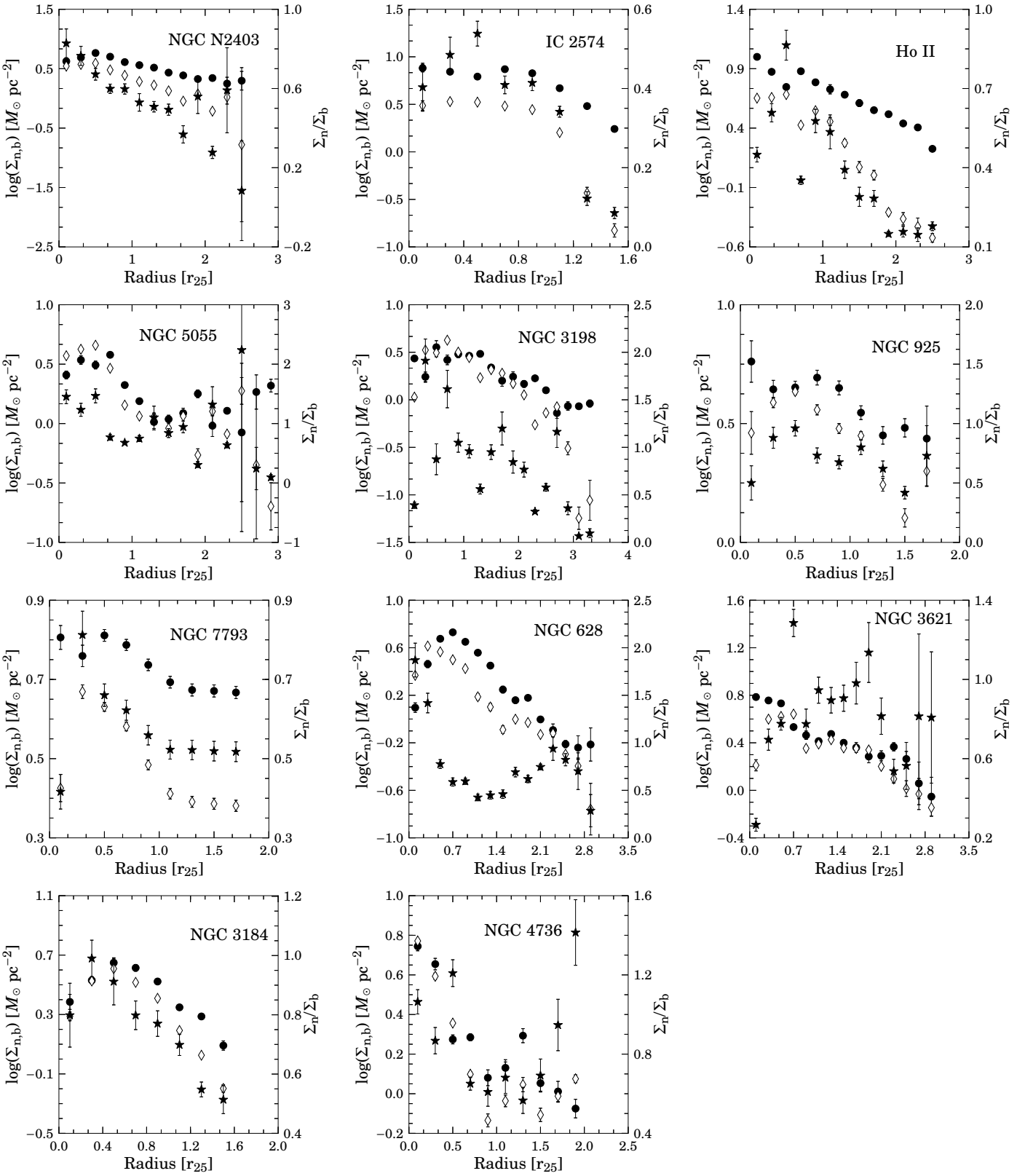

Figure 42: *Open symbols*: surface density of the narrow component; *solid black symbols*: surface density of the broad component; *star symbols*: ratio between the surface densities of the narrow and broad components.

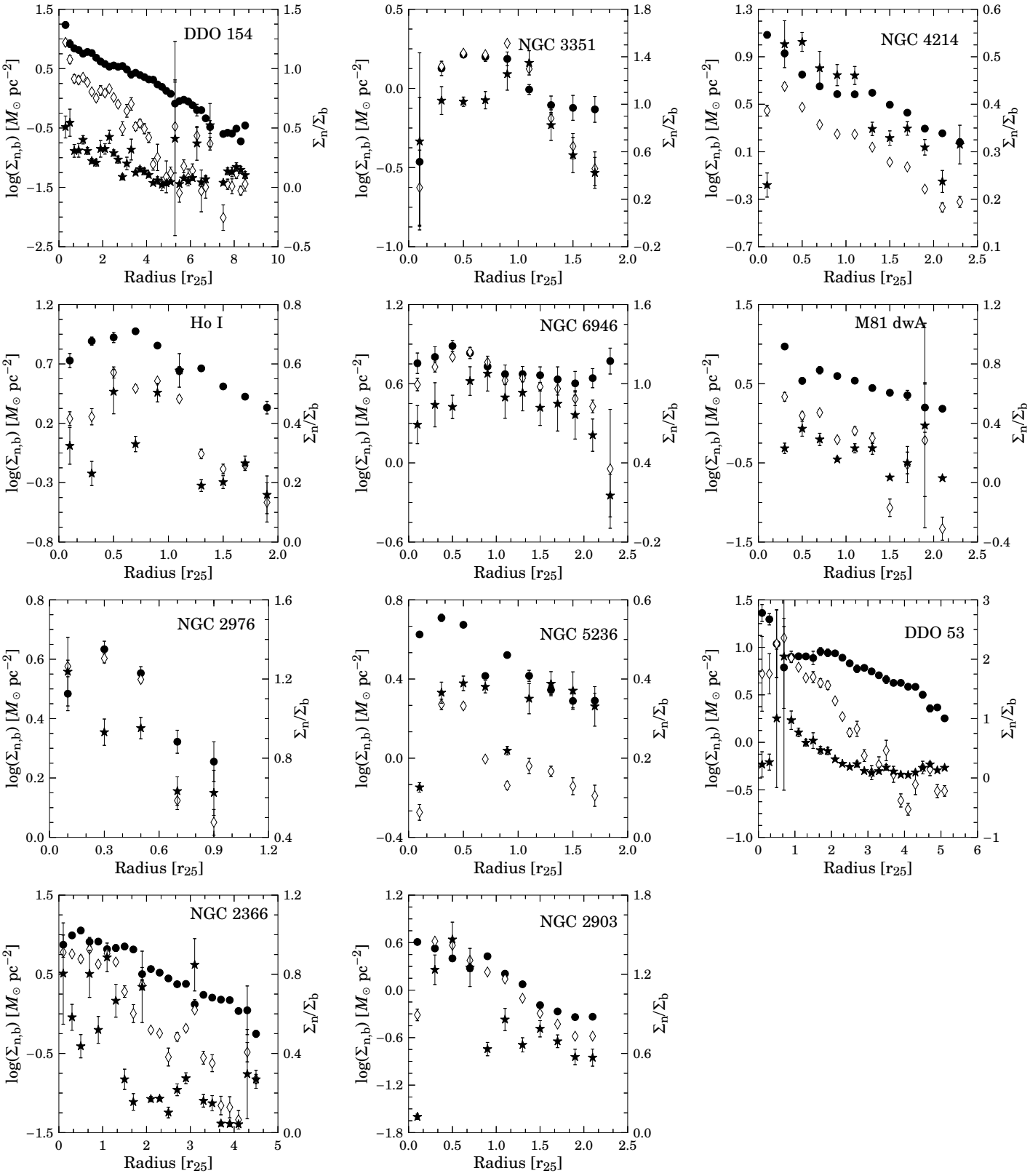

Figure 42: (Continued).

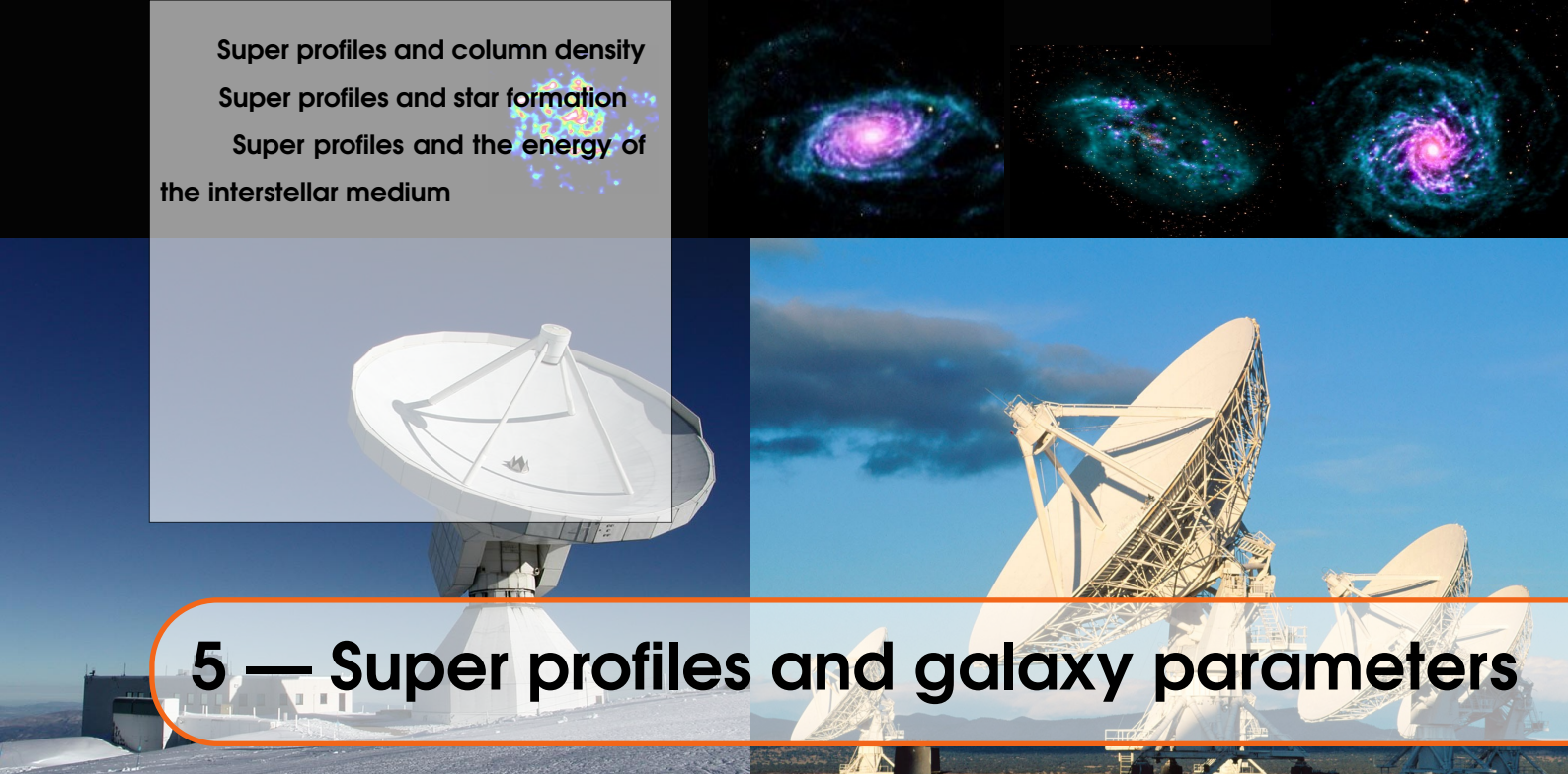

5 — Super profiles and galaxy parameters

5.1 Super profiles and column density

5.1.1 Overview

The thermal state of the HI gas is set by the intensity of the ambient radiation field and the ability of the gas to protect itself against the penetrating radiation. Far Ultraviolet (FUV, 6 eV $<h\nu <$ 13.6 eV) radiation can convert the CNM into the WNM. If the FUV radiation is low, the WNM can cool to the CNM (Wolfire et al., 1995). The cooling and heating processes are known to depend on the gas column density. As mentioned in Kanekar et al. (2011), the gas is optically thin to ionizing UV photons at low column density $N_{HI} \lesssim 10^{17}$ cm^{-2}, whereas at high column density, 10^{17} cm$^{-2} \lesssim N_{HI} \lesssim 10^{20}$ cm^{-2}, the gas is optically thick to ionizing photons. At a column density of $N_{HI} \gtrsim 10^{22}$ cm^{-2}, the gas is known to be predominantly molecular (Schaye, 2004). Thus, high HI column density favors the formation of cold gas, whereas low column density favors the formation of warm or hot gas. In this chapter, we test the link between the HI column density and the importance of the CNM. Kanekar et al. (2011) found that below a column density threshold value, which they estimated to be $N_{HI} \sim 2 \times 10^{20}$ cm^{-2} ($\sim 1.6\ M_\odot$ pc^2), the formation of the CNM gas is hindered. Warren et al. (2012) analyzed individual HI profiles of 31 nearby dwarf galaxies from the Very Large Array Advanced Camera for Surveys Nearby Galaxy Survey Treasury galaxies (VLA-ANGST, Ott et al., 2012) and THINGS. They found that the CNM gas in their sample is usually located in regions having a total column density above the canonical threshold value for star formation $\sim 10^{21}$ cm^{-2}. In the next section, we investigate possible correlations between the shapes of the super profile and the gas column

density. Although with stacking, we are losing the spatial information regarding the narrow and broad components, the A_n/A_b ratio should still correlate with column density if the narrow component is indeed concentrated in high column density regions. We also investigate possible relationship between the gas velocity dispersion and column density.

5.1.2 Results

We plot the A_n/A_b ratios as a function of column density in Figure 43 for three galaxies, the rest are shown in Figure 48 of Appendix B. For the 11 galaxies where CO observations are available, we also plot the A_n/A_b as a function of both HI and total (HI + H_2) column density. We use the same procedure and conversion factor as described in Leroy et al. (2009) to convert the CO surface density to H_2 surface density. In many cases, the A_n/A_b ratios increase with increasing HI and/or total column density values. This increase of A_n/A_b with column density starts around an HI column density value of (2.5-4)$\times 10^{20}$cm^{-2}. For the galaxies where CO observations are available, we found that higher values of the A_n/A_b ratio tend to correspond to regions having molecular gas. In low column density regions, the shapes of the super profiles tend to be more Gaussian and the total flux is dominated by the broad component. Similarly, in high column density regions, the super profiles are strongly non-Gaussian. This change in shape and the fact that the A_n/A_b ratio increases with column density indicates that the narrow component preferentially forms in high-column density regions. This is consistent with the CNM formation. As explained in Kanekar et al. (2011), at low column density, the shielding of the HI gas against UV photons is inefficient. UV photons can therefore penetrate the gas easily at low column density and this keeps the gas mostly warm and hinders the formation of the CNM. At high column density, the HI gas is mostly opaque to incoming UV photons and this favors the formation of the CNM.

We also observe a positive trend of velocity dispersions with HI column density. The correlation with velocity dispersion is stronger and smoother than that with the A_n/A_b ratios. Figure 44 shows plots of the narrow and broad component velocity dispersions as a function of HI column density. Only one galaxy is shown in this figure and the rest can be seen in Figure 49 of Appendix B. Since regions with higher column density values usually corresponds to high star formation regions, the velocity dispersion-column density correlations likely indicate a trend with star formation.

5.2 Super profiles and star formation

5.2.1 Overview

In this section, we investigate the influence of star formation on the HI gas properties. Numerical simulations have shown that star formation affects the surrounding medium by injecting thermal and mechanical energies to the ISM through various physical processes such as stellar winds and supernova explosions (Dib et al., 2006; Tamburro et al., 2009). The effects of the star formation feedback on the HI gas can be investigated by analyzing the shapes of the HI velocity profiles. Star formation and other mechanisms drive turbulence or heat the ISM, thereby increasing the velocity dispersion of the gas. Thus, by comparing the velocity dispersions expected from different ISM energy drivers (e.g. star formation feedback, magnetorotational instability, swing amplification, spiral shocks) with the observed velocity dispersions, we can determine which processes contribute the most to the energy budget of the ISM in specific regions of galaxies (e.g. outer-disks vs inner-disks). Tamburro et al. (2009) investigated this and found that supernova explosions are the main drivers of HI velocity dispersions within the optical disk of galaxies, whereas outside this radius, processes such as magneto-rotational instability and ionizing UV photons were proposed to be the mechanisms that set the observed HI velocity dispersions. Here also, we investigate the physical mechanisms that can explain the observed HI velocity dispersions.

5.2.2 Results

In Figure 45, we plot the single Gaussian, the narrow and broad component velocity dispersions as a function of star formation rate surface density, $\Sigma_{\rm SFR}$ for NGC 2903 and NGC 6946, the rest of the galaxies are shown in Figure 50 of Appendix B. Virtually all our analyzed galaxies show a positive correlation between HI velocity dispersion and $\Sigma_{\rm SFR}$. A global relationship between HI velocity dispersion and $\Sigma_{\rm SFR}$ among galaxies has been observed before and is illustrated in Figure 2 of Dib et al. (2006). Here, we show the relationship between HI velocity dispersion and $\Sigma_{\rm SFR}$ within individual galaxies. As shown in Figure 45 and in the Appendix, for about 30% of the sample, there seem to be two regimes where there is a steady increase followed by a rapid increase in HI velocity dispersion with $\Sigma_{\rm SFR}$. For the rest of the galaxies, the velocity dispersion continually increases with $\Sigma_{\rm SFR}$ without a clear observed break. The observed steady increase or flattening of the velocity dispersion at low star formation rate ($\Sigma_{\rm SFR} \lesssim 5 \times 10^{-4}\ M_{\odot}\ {\rm yr}^{-1}\ {\rm kpc}^{-2}$) may indicate the importance of other mechanisms other than star formation feedback in broadening the HI velocity profiles. In the following, we explore

the physical mechanisms that can explain the observed linewidth of the super profiles.

5.3 Super profiles and the energy of the interstellar medium

There are many mechanisms that can drive turbulence to the ISM and thus broaden the HI velocity profile. Among these mechanisms figure supernova explosions (SNe), magnetorotational instability (MRI) and thermal effects from UV photons (Dib et al., 2006; Sellwood and Balbus, 1999; Stilp et al., 2013; Tamburro et al., 2009). When massive stars with masses greater than somewhere between ~ 8 and $\sim 10\,M_{\odot}$ explode as supernovae, enormous amount of energy are released to the ISM. The energy released during a single supernova explosions can be as high as 10^{51} erg (van Marle et al., 2010). Part of this energy will go into kinetic energy of the ISM. Analytical estimates by Mac Low and Klessen (2004) showed that SNe dominate the global energy input rate of the ISM of the Galaxy. MRI is the consequence of a magnetic force acting on a differentially rotating fluid. In the presence of even a weak magnetic field (10^{-25} G), the motion of a differentially rotating fluid would be destabilized. This phenomena is called MRI. Due to the fact that differential rotation and magnetic fields are common in the ISM, MRI has been proposed to be a source of turbulence in the ISM. UV photons from young stars can heat the surrounding medium and thus, for HI, results in thermal motions of the hydrogen atoms. This also broadens the HI velocity profile. Here we test if one or more of these mechanisms can explain the width of the super profiles.

5.3.1 Energy from supernova (SN)

Following the procedures outlined in Tamburro et al. (2009), the turbulent energy implied by the HI velocity dispersion, $\sigma_{\rm HI}$, is

$$E_{\rm HI} = (3/2)\,\Sigma_{\rm HI}\,\sigma^2_{\rm HI}. \tag{5.1}$$

We can compare this energy to the energy by supernova explosions (SNe) given by

$$E_{\rm SN} = \eta \times (\varepsilon_{\rm SN} 10^{51}{\rm erg})\,\tau_{\rm SN}, \tag{5.2}$$

where η is the SN rate per unit area and $\varepsilon_{\rm SN}$ is the SN efficiency. The SN rate per unit area, η, can be inferred from the star formation rate surface density and can be written as

$$\eta = \Sigma_{\rm SFR} \times \frac{f_{*\rightarrow SN}}{\langle m \rangle}, \tag{5.3}$$

where $f_{*\rightarrow SN}$ is the fraction of massive stars (8-120) $M_{\odot}$ ending up in SNe and $\langle m \rangle$ is the average mass of the population. Assuming a Kroupa (2001) initial mass function (IMF), Tamburro et al. (2009) found $f_{*\rightarrow SN}/\langle m \rangle \simeq 1.3 \times 10^{-2} M_{\odot}^{-1}$ using the mass range (8-120) $M_{\odot}$. As defined in Mac Low (1999) the turbulent decay time, τ_{SN}, or the timescale over which the HI turbulent energy is dissipated depends on the driving scale (i.e. the scale at which the turbulent driving mechanism operates on the ISM), λ, and is given by

$$\tau_{SN} = 9.8 \times \left(\frac{\lambda_{100}}{\sigma_{10}} \right) \mathrm{Myr}, \tag{5.4}$$

where $\lambda_{100} = \lambda/100$pc and $\sigma_{10} = \sigma_{\rm HI}/10$ km s^{-1}. Here, $\sigma_{\rm HI}$ is the average of the HI velocity dispersions derived over our observed star formation rate surface density range. Thus $\sigma_{\rm HI}$ differs from galaxy-to-galaxy. This is different from the $\sigma_{\rm HI}$ = 10 km s^{-1} value adopted by Tamburro et al. (2009). The driving scale λ is roughly 100 pc. Here we use only the single and the broad component velocity dispersions for the HI turbulent energy calculations. This is because the narrow component, which we attribute to the CNM, is likely not be turbulent (Stilp et al., 2013). We show in Figure 46 the turbulent HI energy derived from the single Gaussian and the broad component velocity dispersions as a function of the SN energy inferred from $\Sigma_{\rm SFR}$ for different SN efficiency $\varepsilon_{\rm SN}$ = (0.01, 0.1, 0.5) for NGC 5055. Plots for other galaxies can be seen in Figure 51 in the Appendix. The turbulent HI energy correlates well with the SN energy for most of the galaxies. For spiral galaxies with $\varepsilon_{\rm SN}$=0.01 and dwarf galaxies with $\varepsilon_{\rm SN}$=0.1, there seems to be a one-to-one correlation between $E_{\rm HI}$ and $E_{\rm SN}$ at high $E_{\rm SN}$ or high $\Sigma_{\rm SFR}$. Examples of this are NGC 4736, NGC 4214, NGC 628 and NGC 2903, Ho I, DDO 53, IC 2574. However, at low $\Sigma_{\rm SFR}$, $E_{\rm SN}$ is systematically lower than that of the $E_{\rm HI}$. This may indicate that other sources of energy contribute to the observed linewidth of the profiles. For $\varepsilon_{\rm SN}$ = 0.1, the data points cross the line of equality at a certain $E_{\rm SN}$. Thus, we may have overestimated the SN efficiency at high $\Sigma_{\rm SFR}$. For $\varepsilon_{\rm SN}$ = 0.5, $E_{\rm SN}$ tends to be always larger than $E_{\rm HI}$. Our data is therefore consistent with $\varepsilon_{\rm SN}$ $\lesssim$ 0.1.

5.3.2 Thermal effects from UV photons and magneto-rotational instability (MRI)

UV photons from nearby young stars or of extragalactic origin can inject kinetic energy to the surrounding HI medium through stellar winds (e.g. Schaye, 2004). This will heat up the gas and broaden the HI velocity profiles. At our lowest observed star formation rate surface density $\Sigma_{\rm SFR}$ = 10^{-4} $M_{\odot}$ yr^{-1} kpc^{-2}, we find a single Gaussian velocity dispersion of $\gtrsim$ 6 km s^{-1} even for face-on galaxies like NGC 628, NGC 6946 and NGC 5236, NGC 3184. For NGC 628, with an inclination of only 7°, we

find a single Gaussian velocity dispersion of 6 km s^{-1} at $\Sigma_{\rm SFR} = 10^{-4}\,M_{\odot}$ yr^{-1} kpc^{-2}. If this velocity dispersion was purely thermal and if we apply the relationship between temperature and line-width, FWHM $= 0.22\,\sqrt{\rm T}$ (Walterbos and Braun, 1996), then this velocity dispersion gives a temperature of $\sim$ 6000 K, corresponding to a warm HI phase in the unstable regime (Wolfire et al., 2003). Again for NGC 628, its broad component velocity dispersion is about 8 km s^{-1} at $\Sigma_{\rm SFR} = 10^{-4}\,M_{\odot}$ yr^{-1} kpc^{-2}. This gives a temperature of 9000 K, which also corresponds to HI in the warm phase but in the stable regime. From about $\Sigma_{\rm SFR} \sim 5\times10^{-4}\,M_{\odot}$ yr^{-1} kpc^{-2}, there is a sudden linear increase of the broad component velocity dispersion with $\Sigma_{\rm SFR}$. At $\Sigma_{\rm SFR} \sim 5\times10^{-4}\,M_{\odot}$, the observed broad component velocity dispersion is 9.5 km s^{-1}. This velocity dispersion value cannot be due to the thermal motions of hydrogen atom alone as it would mean that the gas is ionized. Therefore, this may be attributed to turbulent motions caused by physical processes such as SNe. MRI has also been previously proposed to explain the HI linewidth in the outer disk of galaxies where star formation is rare or absent (Sellwood and Balbus, 1999). The 6 km s^{-1} single Gaussian velocity dispersion we found for our most face-on galaxy NGC 628 can also be attributed to MRI turbulence as demonstrated by Sellwood and Balbus (1999). Again, we use the same formula adopted by Tamburro et al. (2009) to calculate the energy from the MRI:

$$E_{\rm MRI} = \varepsilon_{\rm MRI}\,\eta_{\rm MRI}\,\tau_{\rm MRI}, \tag{5.5}$$

where ε_{MRI} is the efficiency at which the MRI energy is converted to kinetic energy; $\eta_{\rm MRI}$ is the rate of the energy from MRI and $\tau_{\rm MRI}$ is the timescale over which the turbulent energy from MRI is dissipated. The rate of the energy from MRI is

$$\eta_{\rm MRI} = 3.7\times10^{-8}\,{\rm erg\,cm^{-2}\,s^{-1}}\times\left(\frac{\rm h_z}{\rm 100pc}\right)\times\left(\frac{\rm B}{6\,\mu{\rm G}}\right)^2\times\frac{\Omega}{(220\,{\rm Myr})^{-1}}. \tag{5.6}$$

Here also, we assume a vertical thickness h_z = 100 pc for the gaseous disk, a constant magnetic field of 6 μG. The angular velocity $\Omega = v/r$ is calculated from the rotation curve of the galaxy. The decay time for the turbulent MRI energy is

$$\tau_{\rm MRI} = 9.8\,(\lambda_{100}/\sigma_{10}){\rm Myr}, \tag{5.7}$$

where $\lambda_{100} = \lambda/100$ pc. The driving scale λ is given by

$$\lambda = 2\pi\,v_A\left[-\frac{3+\alpha}{4}\frac{d\Omega^2}{dlnr}\right]^{-1/2}, \tag{5.8}$$

where $\alpha = dlnv/dlnr$ and $v_A = B/\sqrt{4\pi\rho}$ is the Alfvén velocity. Note that due to the almost face-on orientation of NGC 628, its rotation curve is not available in the high-resolution rotation curve study by de Blok et al. (2008); therefore, we adopt the rotation curve by Kamphuis and Briggs (1992) for this galaxy. Rotation curves for part of our sample galaxies were derived by de Blok et al. (2008) and we use them in this study. We show in Figure 47 and in Figure 52 of the Appendix, the turbulent HI energy, the supernova energy inferred from the star formation rate surface density and the MRI energy as a function of radius. Note that only those galaxies in which we have available rotation curves are plotted.

For the E_{SN}, we reach similar conclusions as in Figure 46. The data agrees with a supernova efficiency $\varepsilon_{SN} = 0.01$ at the very center of the galaxy which also corresponds to the highest star formation rate surface density. At approximately the optical radius, r_{25}, the data corresponds to $\varepsilon_{SN} = 0.1$. The supernova energy corresponding to $\varepsilon_{SN} = 0.5$ and 1 is always larger than the energy inferred from the width of the super profiles.

For about half of the sample, the turbulent energy from MRI, E_{MRI}, tends to be always lower than the energy inferred from the width of the super profiles except for $\varepsilon_{MRI} = 1$, which is physically unrealistic. This suggests that other physical mechanisms such as thermal effects from UV photons contribute to the broadening of the HI profile at large radii. For the rest of the sample, the E_{MRI} corresponding to $\varepsilon_{MRI} = 0.1$ and 0.5 cross or approach the values of the energy inferred from the width of the super profiles at large radii.

We conclude that within the optical radius, the energy from supernova can account for the observed width of the profiles and our data suggests a supernova efficiency between 0.01 and 0.1. A proper modeling of the supernova efficiency as a function of radius is desired in order to better compare the turbulent energy inferred from the HI linewidth with that of supernova. For about half of the sample, the energy from MRI is not enough to explain the observed width of the super profiles and thus other sources of energy are required to explain the width of the super profiles at large radii. There are other previously proposed sources of turbulence such as galactic rotation, spiral shocks, gravitational instability which were not investigated in this thesis. A combination of these mechanisms may explain the observed width of the super profiles at large radii.

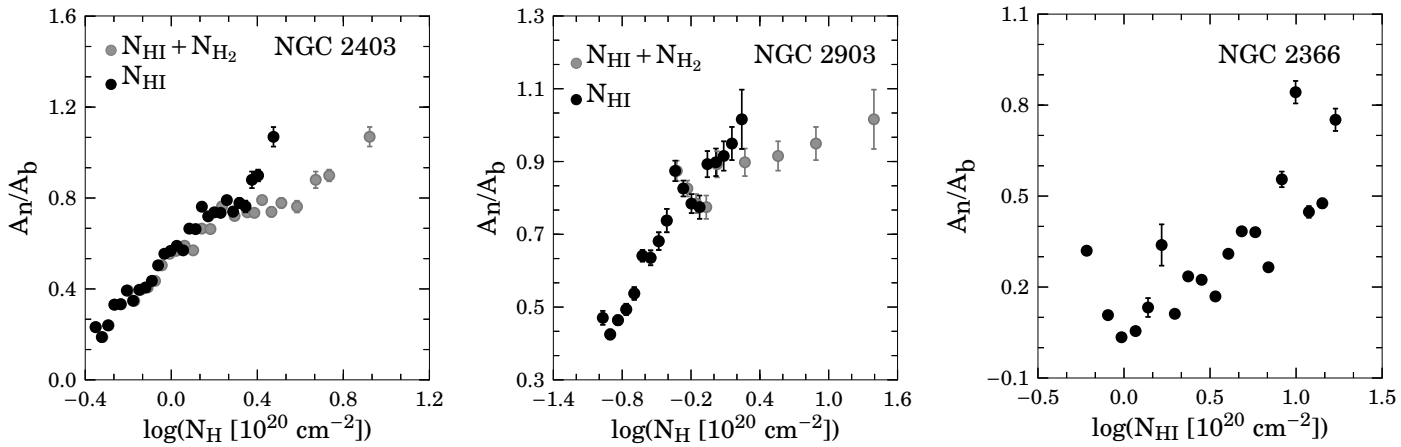

Figure 43: Flux (mass) ratio between the narrow and broad components, A_n/A_b, as a function of HI or total column density (HI+H_2). The black solid circle symbols represent the HI column density, whereas grey symbols represent the total column density, including the molecular gas.

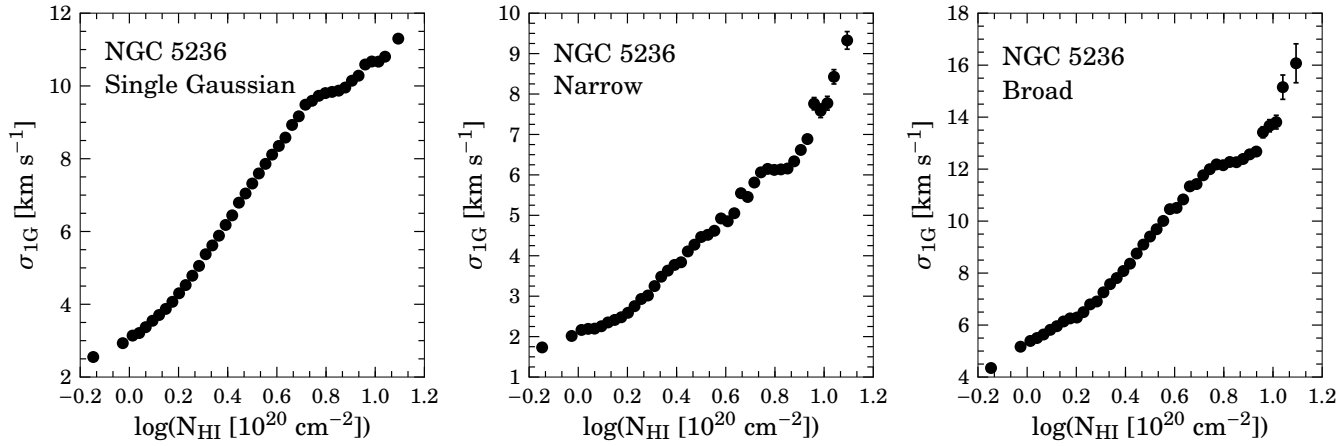

Figure 44: Velocity dispersion of the single Gaussian, narrow and broad components as a function of HI column density.

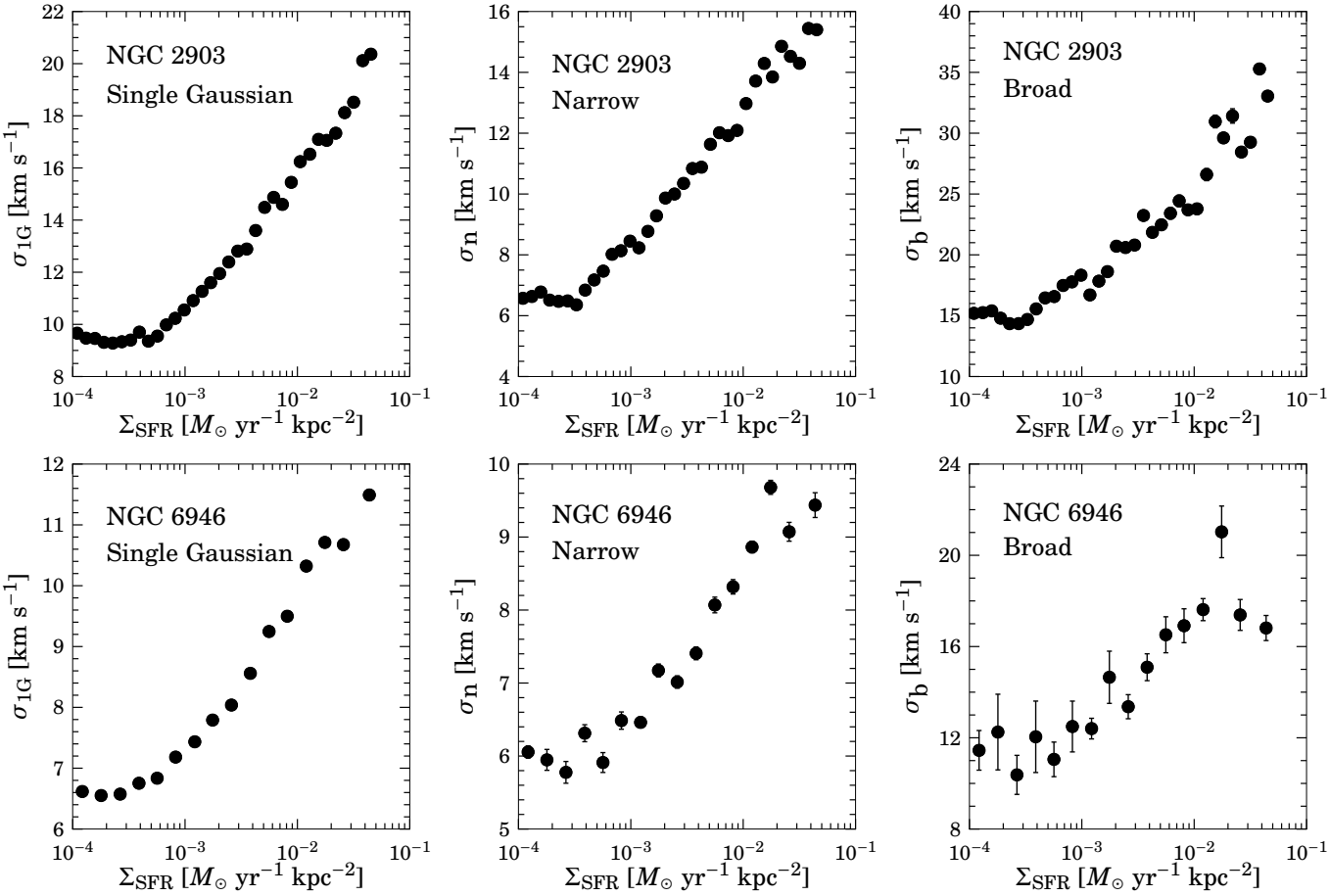

Figure 45: Velocity dispersion of the single Gaussian narrow and broad components as a function of star formation rate surface density, Σ_{SFR}.

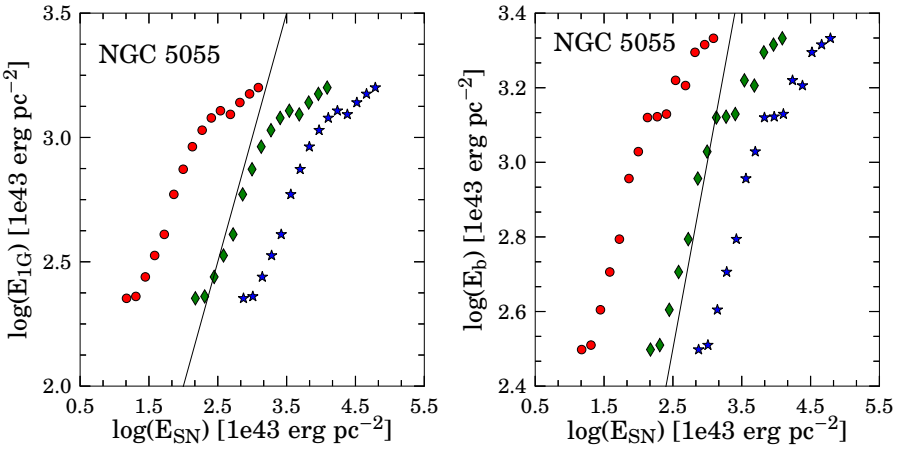

Figure 46: Turbulent HI energy as a function of supernova energy. The circle symbols represent a supernova efficiency, ε_{SN}=0.01; the diamond symbols represent ε_{SN}=0.1 and the star symbols correspond to ε_{SN}=0.5. The black solid line is a line of equality.

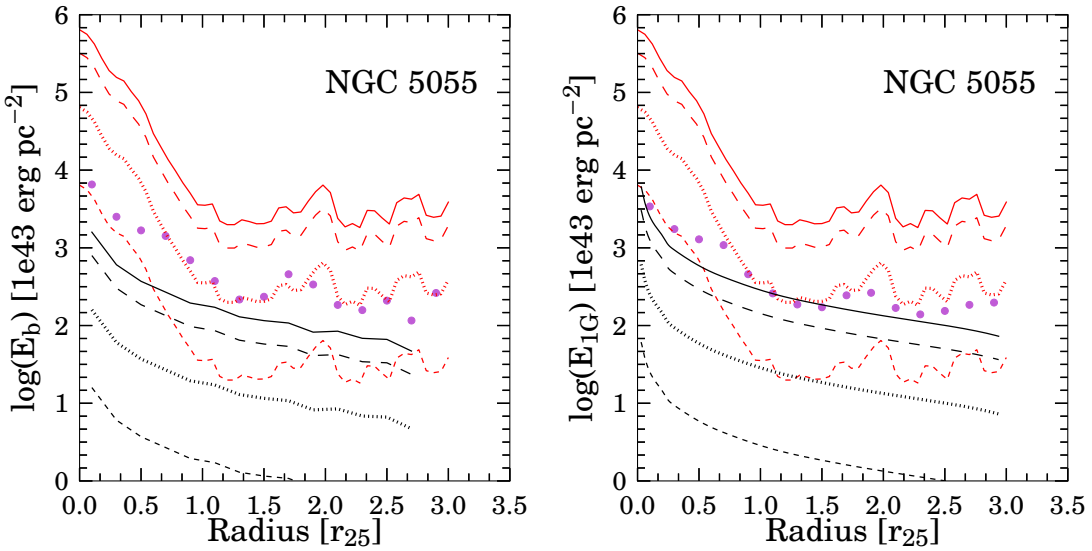

Figure 47: Comparison of turbulent energy inferred from the width of the super profiles with the turbulent energy from supernova (SN) and magneto-rotational instability (MRI). The solid circle symbols represent the turbulent energy inferred from the width of the super profiles; the black lines represent the MRI energy and the red lines represent the SN energy. The different line-styles represent different energy efficiency. The short-dashed lines represent an efficiency of 0.01; the dotted lines represent an efficiency of 0.1; the long-dashed lines represent an efficiency of 0.5 and the solid lines represent an efficiency of 1.

6 — Summary and future work

6.1 Summary

We have analyzed the HI velocity profiles of a selected 22 galaxies from The HI Nearby Galaxy Survey (THINGS; Walter et al., 2008) with the aim of studying the properties of the interstellar medium (ISM) and the star formation in these galaxies. We have stacked individual profiles to obtain high signal-to-noise (S/N) *super profiles*. The super profiles were decomposed into Gaussian components following Young and Lo (1996, 1997) and de Blok and Walter (2006). After quantifying all the relevant systematic effects, we found that the super profiles are optimally described by the sum of a narrow and a broad Gaussian component. We have also presented results from a single Gaussian fitting of the super profiles to facilitate comparisons with work from the literature that did not use multiple components in the fitting of the HI velocity profiles. For each galaxy, we have derived super profiles using the entire HI disk, inside and outside the optical radius r_{25}, as a function of radius, HI and HI+H_2 column densities, and star formation rate surface density. We have also investigated previously proposed energy drivers of the ISM that may explain the observed width of the super profiles. These are supernova explosions (SNe), thermal effects from ultra-violet (UV) photons and magnetohydrodynamic (MHD) instability.

Globally (i.e., across the entire HI disk of the galaxies), we found a narrow component velocity dispersion ranging from 2.6 km s^{-1} (M81 dwA) to 8.5 km s^{-1} (NGC 3198) with a mean of 5.7 $\pm$ 1.3 km s^{-1}. The broad component velocity dispersion ranges from 8.5 km s^{-1} (M81 dwA) to 16.7 km s^{-1} (NGC 3198) with a mean value of 12.6 $\pm$ 2.5 km s^{-1}. Finally, the single Gaussian velocity dispersion

range from 7.2 km s^{-1} (NGC 4214) to 11.6 km s^{-1} (NGC 3198) with a mean of 8.7 $\pm$ 1.3 km s^{-1}. Our mean single Gaussian velocity dispersion is smaller than the mean second moment velocity dispersion found by Leroy et al. (2008) for the same sample galaxies. This is due to the fact that the second moment velocity dispersion is sensitive to the wings of the profiles. Apart from the global analysis of the velocity dispersion, we have also looked at the correlation between the overall shapes of the super profiles and star formation indicators. We found that the shapes of the super profiles correlate with star formation indicators such as far-UV–near-UV colors, metallicity and Hα luminosity.

Radially, we found a higher velocity dispersion and higher narrow component fractional line flux (A_n/A_b) inside the optical radius r_{25} compared to those in the outer HI disk. We divide our sample galaxies into dwarfs and spirals according to the definition by Leroy et al. (2008). Except for a few dwarf galaxies, we find a higher velocity dispersion value inside the optical radius r_{25}. The higher velocity dispersion inside the optical radius is caused by star formation driving turbulence into the HI medium. In addition, the higher fractional line flux of the narrow component inside the optical radius indicates the importance of the presence of the CNM for star formation. We also find that the velocity dispersion decreases exponentially with radius for virtually all the analyzed galaxies. For a few dwarf galaxies, the velocity dispersion is constant or independent of radius. The A_n/A_b ratio also seems to decrease with radius. However, only 20 % of our sample galaxies show an abrupt decrease in the A_n/A_b ratio near the optical radius. For most galaxies, the Σ_n/Σ_b ratio continually decline with radius without a clear break. This is different from the work by Braun (1997), who found that the fractional line flux of the so-called high brightness network (HBN), attributed to the CNM, decreases abruptly near the optical radius, r_{25}. Investigation of this difference is left as future work.

We find a positive correlation between velocity dispersion, HI column density and star formation rate surface density, Σ_{SFR}. For about 30% of the analyzed galaxies, there seem to be two regimes where there is a slow increase in velocity dispersion at low Σ_{SFR}, followed by a rapid increase in velocity dispersion at high Σ_{SFR}. For the rest of the galaxies, the velocity dispersion continually increases with Σ_{SFR} without a clear break. We interpret the observed steady increase or flattening of the velocity dispersion at low star formation rate surface density ($\Sigma_{SFR} \sim 5 \times 10^{-4}\ M_\odot\ yr^{-1}\ kpc^{-2}$) to be due to the inefficiency of star formation in broadening the HI velocity profiles. Other sources of energy may be responsible for the broadening of the velocity profiles at this low star formation rate regime. We have examined whether SNe, MHD instability and thermal effects from UV photons can explain the observed width of the super profiles. For our most face-on galaxy NGC 628, below about

$\Sigma_{SFR} \sim 5 \times 10^{-4}\ M_{\odot}\ yr^{-1}\ kpc^{-2}$, thermal effects from UV photons and MHD instability can explain the observed width of the super profiles. However above this value, the observed width of the super profiles may be attributed to SNe. In general, within the optical radius, the energy from supernova can accounts for the observed width of the profiles and our data suggests a supernova efficiency between 0.01 and 0.1. Regarding the turbulent energy from MRI, we find that for about half of the sample, E_{MRI} tends to be always lower than the energy inferred from the width of the super profiles except for an efficiency $\varepsilon_{MRI} = 1$, which is physically unrealistic. This suggests that other physical mechanisms such as thermal effects from extragalactic background UV photons (Schaye, 2004) contribute to the broadening of the HI profile at large radii. For some galaxies, the E_{MRI} corresponding to $\varepsilon_{MRI} = 0.1$ and 0.5 cross or approach the values of the energy inferred from the width of the super profiles at large radii. Although we have shown that the energy from supernova can account for the observed width of the super profiles within the optical radius, we still lack a proper modeling of the supernova efficiency as a function of radius to allow a better comparison between the turbulent HI energy and the supernova energy. Moreover, there are considerable uncertainties in the calculation of the supernova energy and E_{MRI} as discussed in Tamburro et al. (2009).

6.2 Future work

This thesis has examined the connection between the narrow component, attributed to the CNM, and star formation. However, we have not yet fully explored the connection between the CNM and molecular gas (H_2) as traced by CO. This can be done by comparing the shapes of the super profiles in regions having CO with those without a detected CO emission. Where the signal-to-noise (S/N) is adequately high, we can do a pixel-by-pixel study and compare maps of the identified narrow component with the corresponding CO maps to allow a more direct comparison between the distribution of the narrow component and that of the CO. If the CNM traces H_2, then the CNM study (as traced by the narrow component) will offer a unique probe of star formation for low-metallicity galaxies in which CO observations are problematic. It would also be interesting to select very nearby galaxies and observe these at sufficiently high linear and velocity resolution to resolve the more compact, clumpy CNM. It would also be interesting to identify the narrow component in the very low column density outer-HI disks of galaxies where no CO emission is detected. This will allow us to quantify the amount of the CNM in the halos of galaxies. This will also allow us to study the connection between the amount of the CNM and star formation in the low column density outer-HI disks. This analysis requires

high-sensitivity data. The Westerbork Hydrogen Accretion in LOcal GAlaxieS (HALOGAS; Heald et al., 2011) offers the sensitivity to carry out this analysis. The HALOGAS survey was designed to detect faint, diffuse HI at a characteristic column density of a few times 10^{19} cm^{-2}. The stacking technique used in this thesis could achieve even higher sensitivity.

Another analysis which can be done as an extension of this thesis work is also the use of the derived velocity dispersions in the Toomre Q-stability parameter analysis. Previous work has usually assumed a constant HI velocity dispersion as a function of radius. However, this thesis has demonstrated that the HI velocity dispersion decreases exponentially with radius for virtually all the analyzed galaxies. In addition, previous work usually treats the HI as a single-component and thus used a velocity dispersion that also include the contribution from the warm HI. However, as explained in Schaye (2004) and de Blok and Walter (2006), it is the CNM that contributes the most to the disk instability due to its lower velocity dispersion. Therefore, treating the HI as a single component underestimates the contribution of the CNM in the disk instability. The analysis of the Toomre Q-stability parameter, taking into account the presence of the two components of the HI gas will be left as future work. This will enable study of the relative contribution of each gas components to the instability of disk galaxies.

This work has enabled us to study the physics of the interstellar medium in a sample of 22 nearby galaxies as observed by THINGS. In the future, the wealth of data from future HI surveys such as the Widefield ASKAP L-Band Legacy All-sky Blind SurveY (WALLABY), the MeerKAT HI Observations of Nearby Galactic Objects: Observing Southern Emitters (MHONGOOSE), the Looking At the Distant Universe with the MeerKAT Array (LADUMA) HI survey will allow us to study the connection between the physics of the interstellar medium and star formation and to extend this work to high-redshift galaxies. When the Square Kilometre Array (SKA) telescope becomes available, we can study the very compact CNM and trace HI out to very large radii for a large sample of galaxies. The sensitivity of the SKA will allow us to study the low column density HI and to see how far in radius does the CNM extends.

Appendix

Appendix A

Testing S/N effects

Here we test the effects of choosing different S/N cut-offs on the shapes of the resulting super profiles. Choosing inappropriate value for the S/N cut-off could result in noise peaks and multiple peaked low S/N profiles being included in the stacking, which could artificially broaden the super profiles. We derive super profiles of NGC 2403 and IC 2574 using different types of data cubes (robust and natural-weighted, residual-scaled and non-residual scaled) and adopt 3 times rms, 4 times rms and 5 times rms S/N cut-offs. We choose these two galaxies as representative of spirals and dwarfs in our sample. We compare the results in Table 10 for σ_b and Table 11 for A_n/A_b ratio. It is clear that the different cut-offs all give similar results and conclude that the 3 times rms is a reasonable S/N cut-off.

TABLE 10
BROAD COMPONENT VELOCITY DISPERSIONS USING DIFFERENT S/N CUT-OFFS (km s^{-1})

NGC 2403				IC 2574			
NA	NA-res	RO	RO-res	NA	NA-res	RO	RO-res
S/N cut-off: 3 times rms							
17.9	12.7	17.8	12.2	15.8	11.2	14.1	11.1
S/N cut-off: 4 times rms							
17.8	12.7	17.8	12.1	16.6	11.2	13.9	11.1
S/N cut-off: 5 times rms							
18.0	12.6	17.5	12.1	16.1	11.3	13.9	11.1

TABLE 11
A_n/A_b RATIO FROM USING DIFFERENT S/N CUT-OFFS

NGC 2403				IC 2574			
NA	NA-res	RO	RO-res	NA	NA-res	RO	RO-res
S/N cut-off: 3 times rms							
0.54	0.79	0.57	0.82	0.45	0.42	0.51	0.55
S/N cut-off: 4 times rms							
0.55	0.78	0.58	0.83	0.46	0.43	0.48	0.54
S/N cut-off: 5 times rms							
0.57	0.78	0.58	0.83	0.48	0.44	0.47	0.55

Appendix B

FIGURE ATLAS

B.1 A_n/A_b ratio and column density

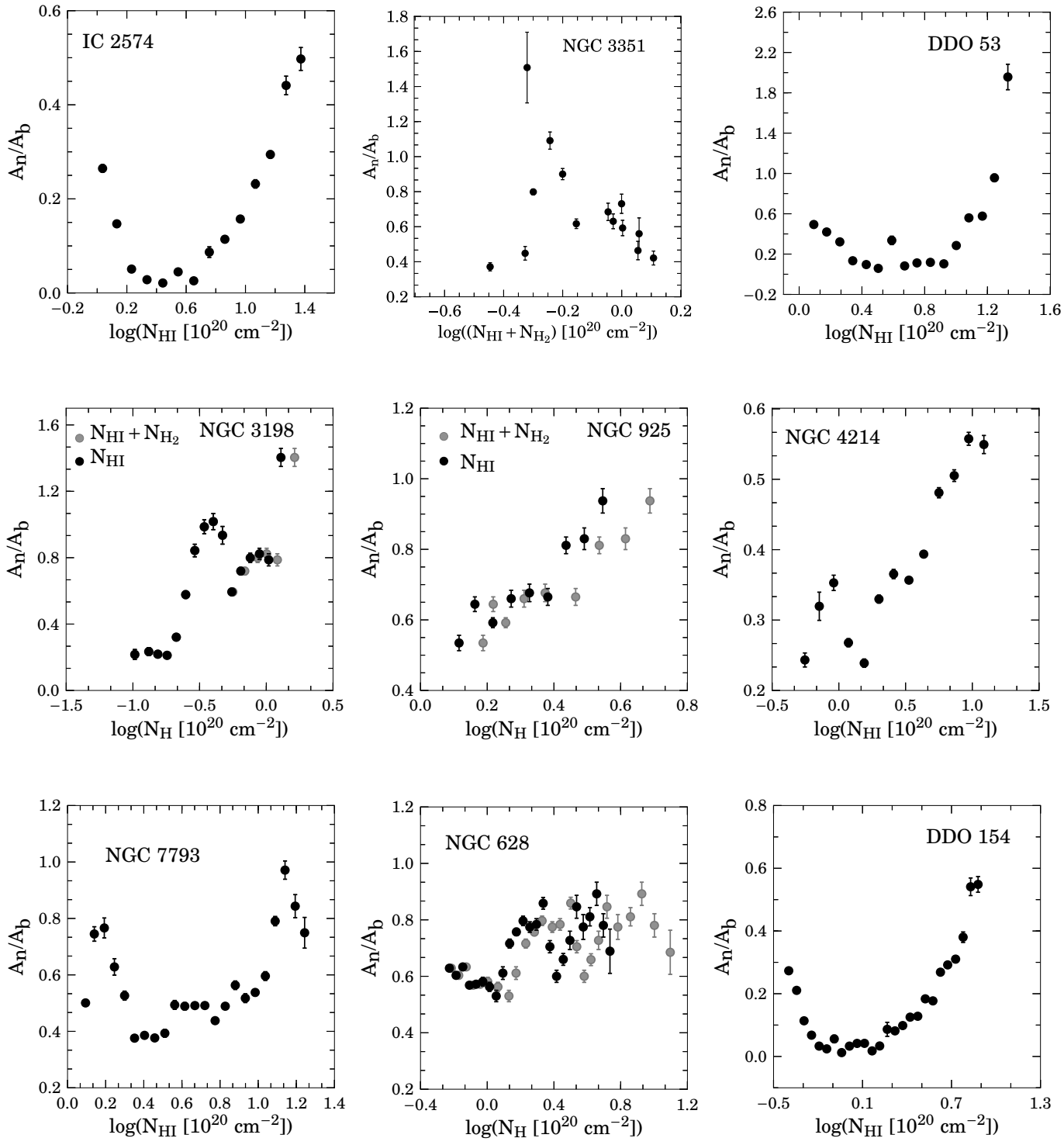

Figure 48: Flux (mass) ratio between the narrow and broad components, A_n/A_b, as a function of HI or total column density (HI+H_2). The black solid circle symbols represent the HI column density, whereas grey symbols represent the total column density, including the molecular gas.

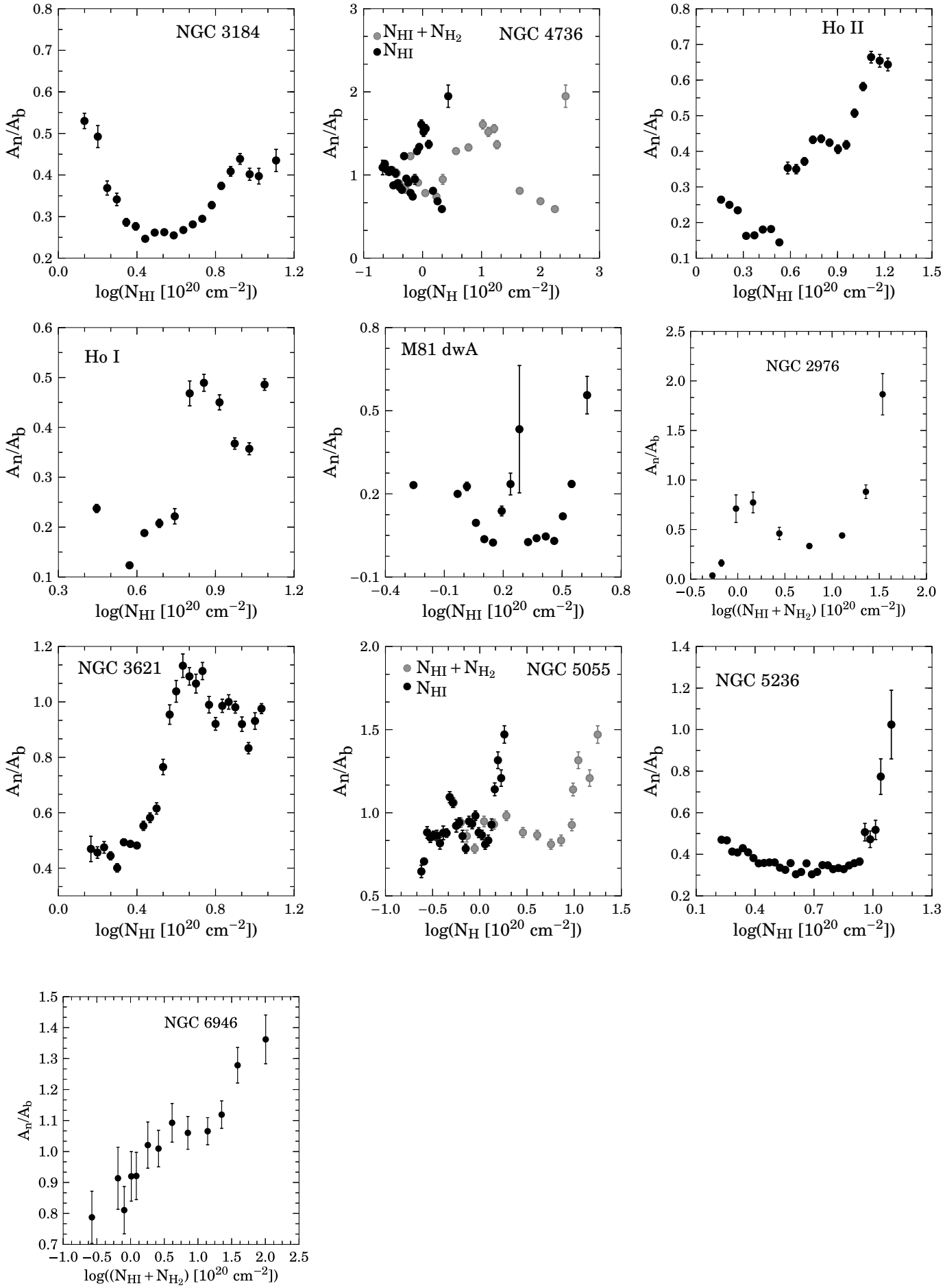

Figure 48: (Continued).

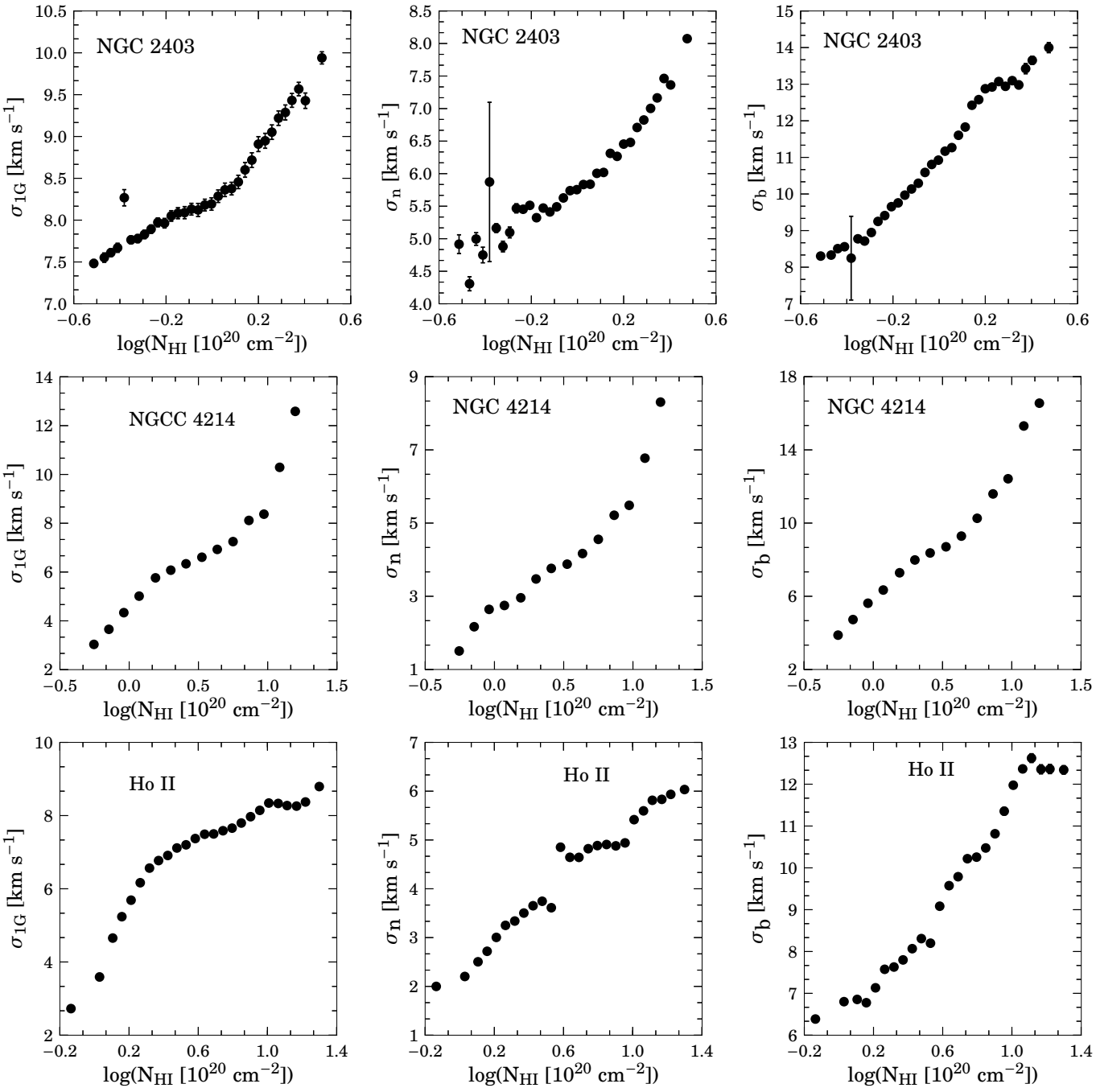

Figure 49: Velocity dispersion of the single Gaussian, narrow and broad components as a function of HI column density.

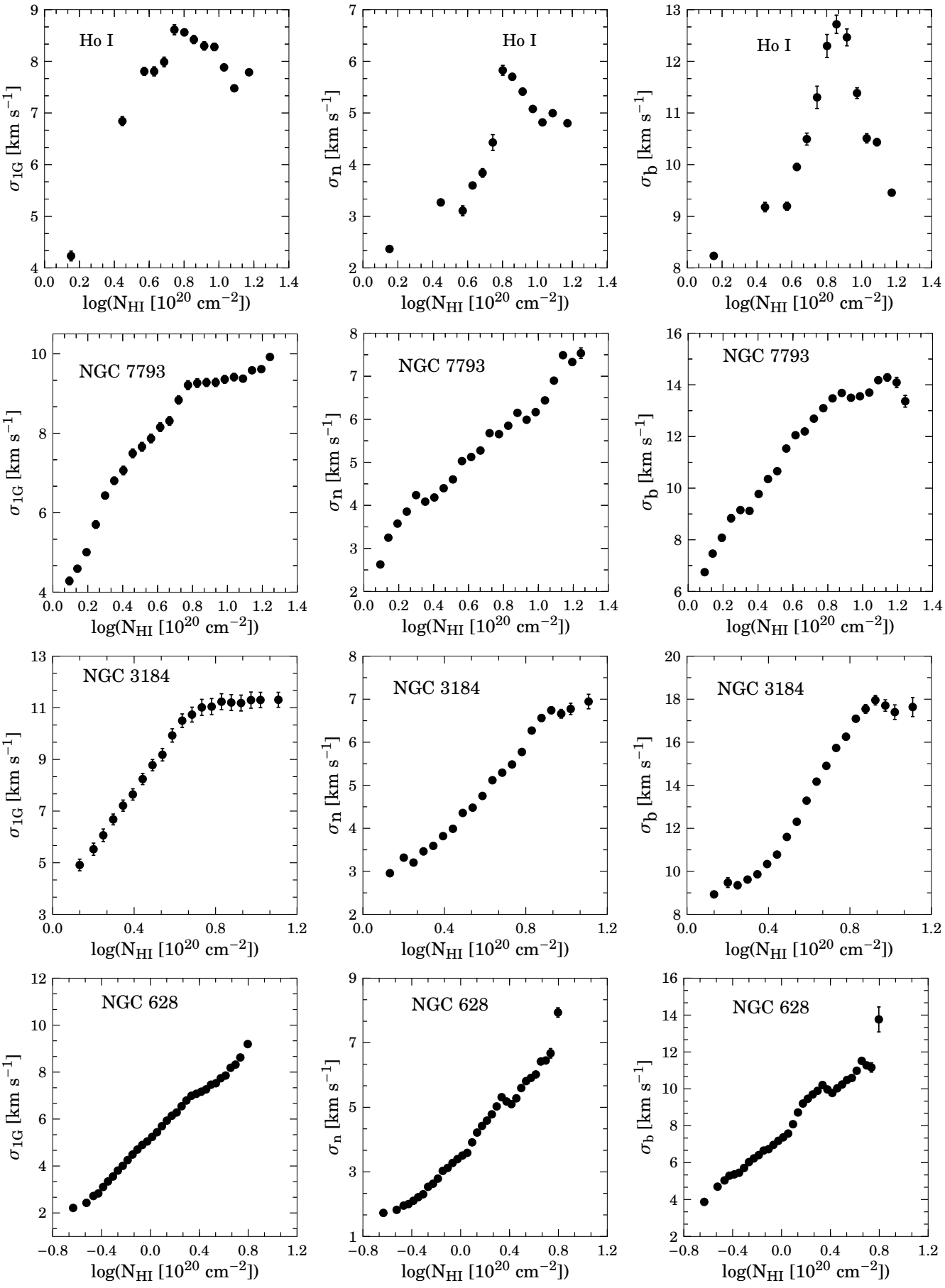

Figure 49: (Continued).

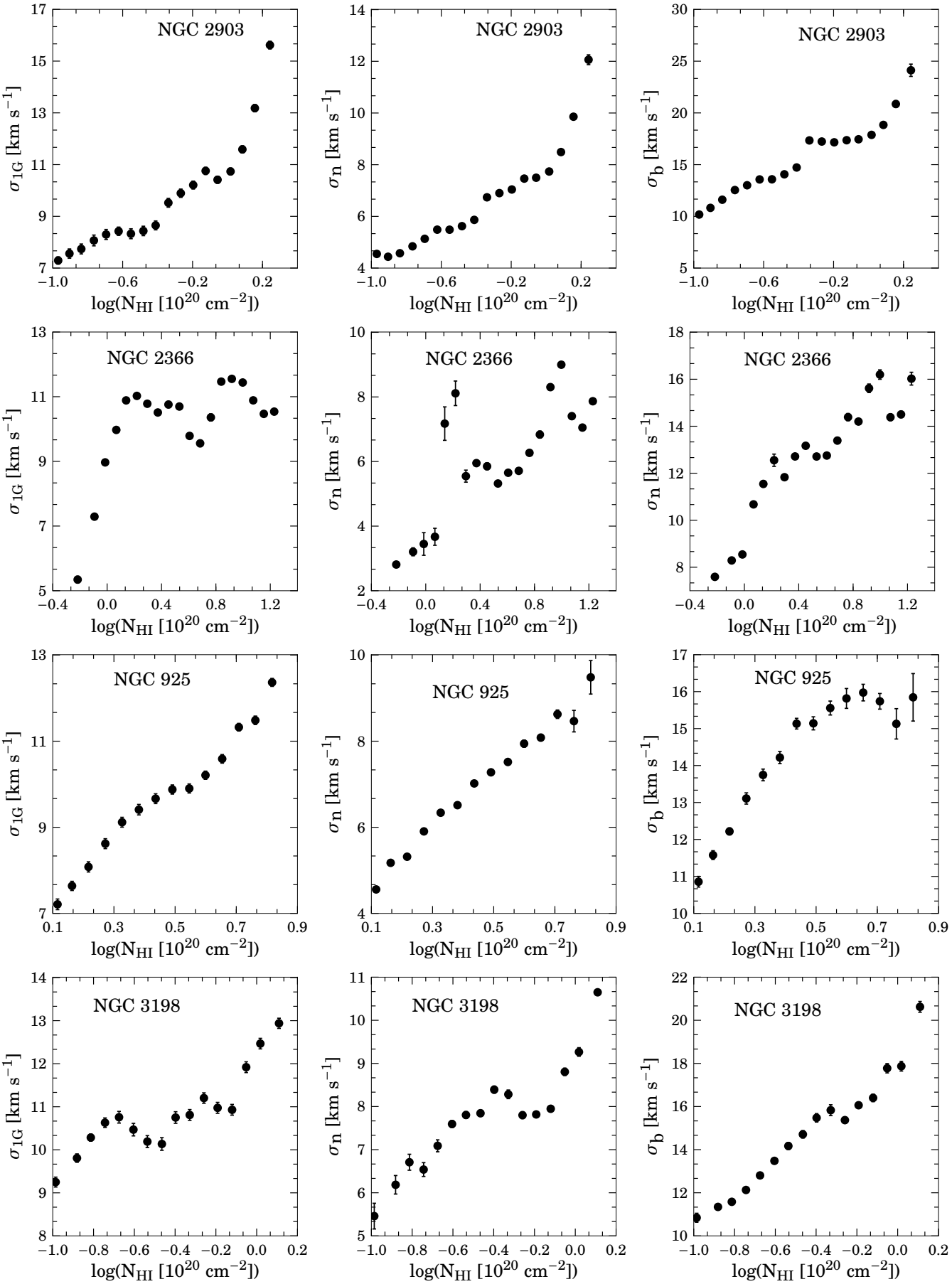

Figure 49: (Continued).

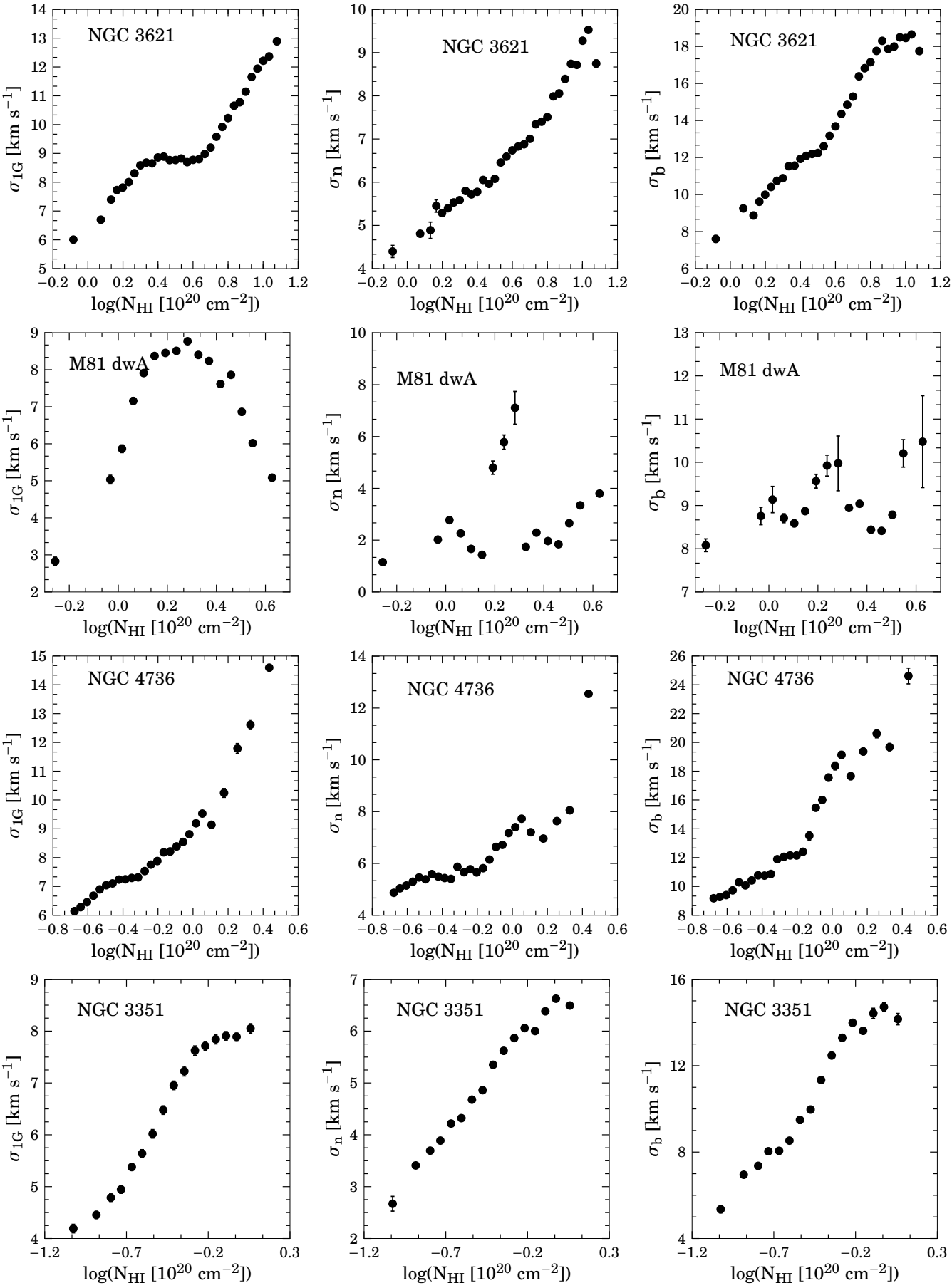

Figure 49: (Continued).

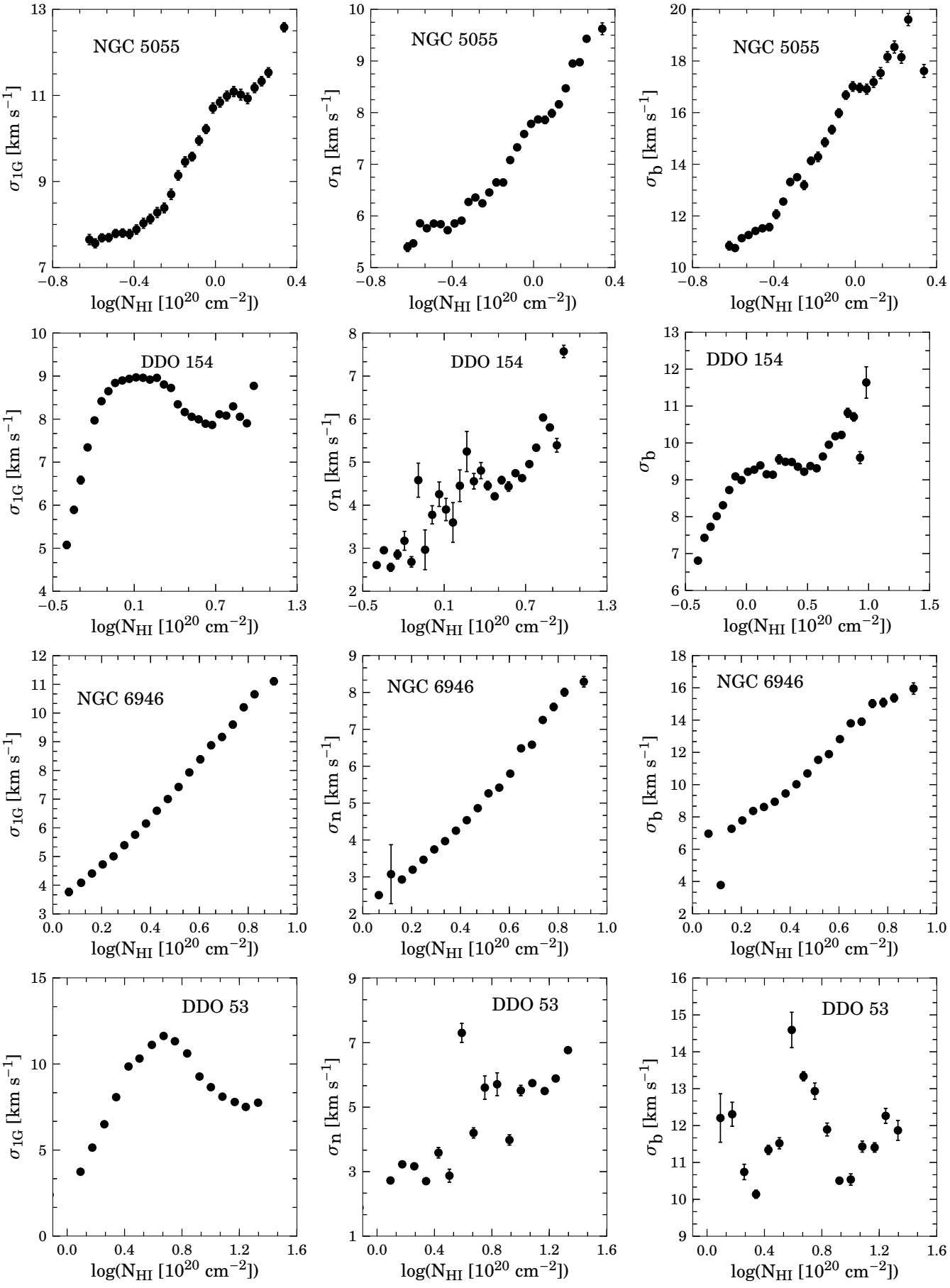

Figure 49: (Continued).

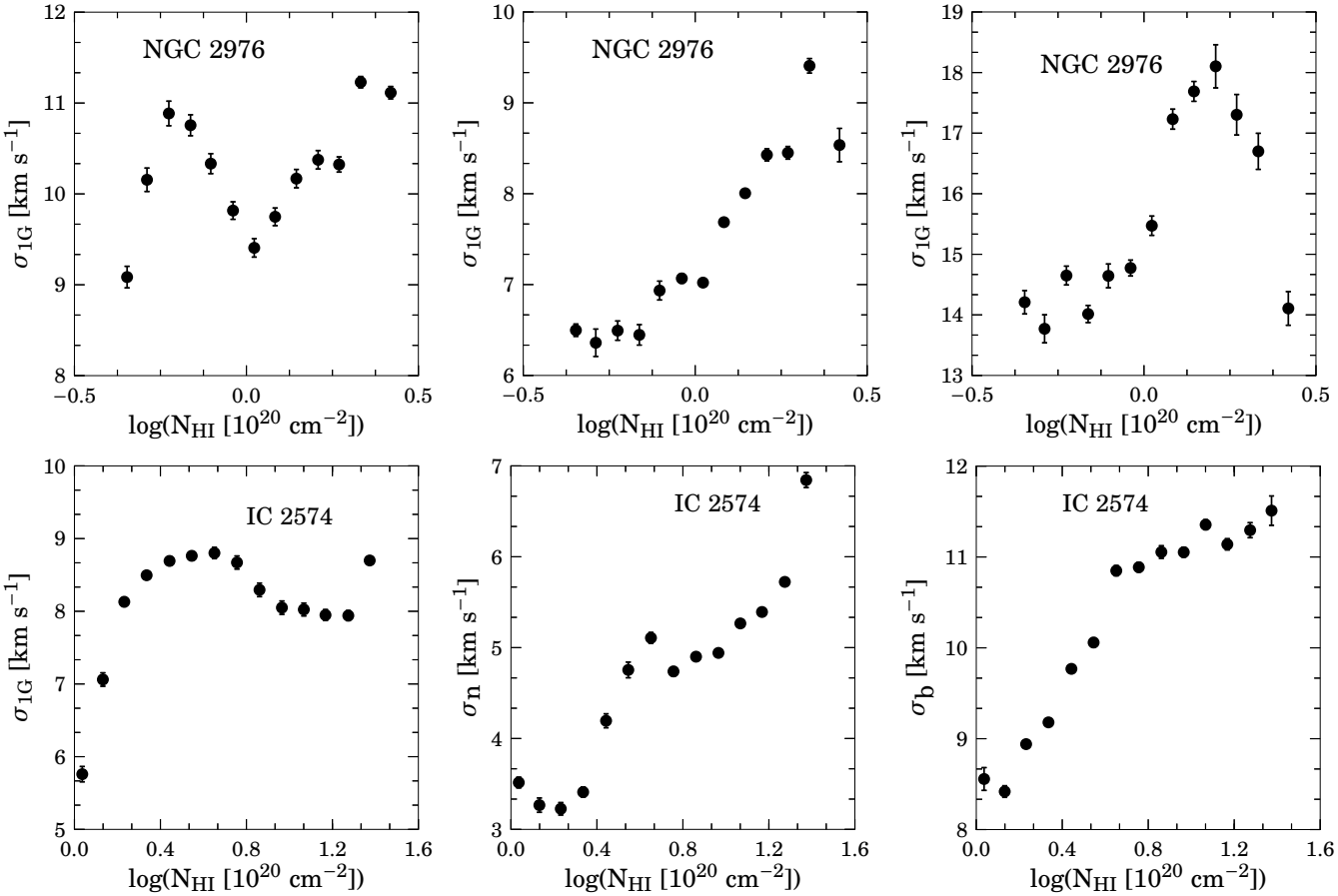

Figure 49: (Continued).

B.3 Velocity dispersion and Σ_{SFR}

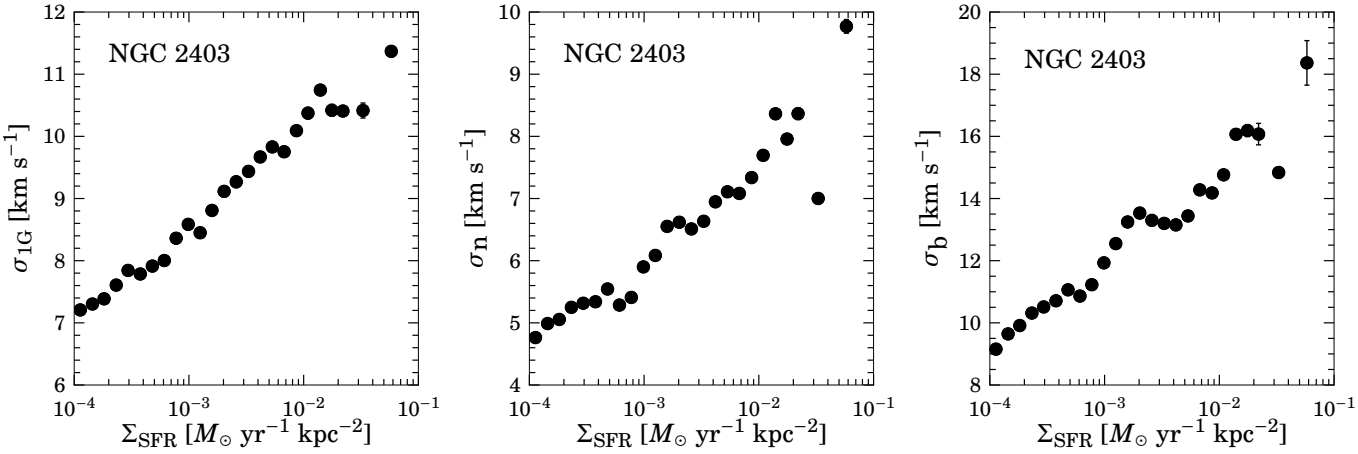

Figure 50: Velocity dispersion of the single Gaussian, narrow and broad components as a function of star formation rate surface density, Σ_{SFR}.

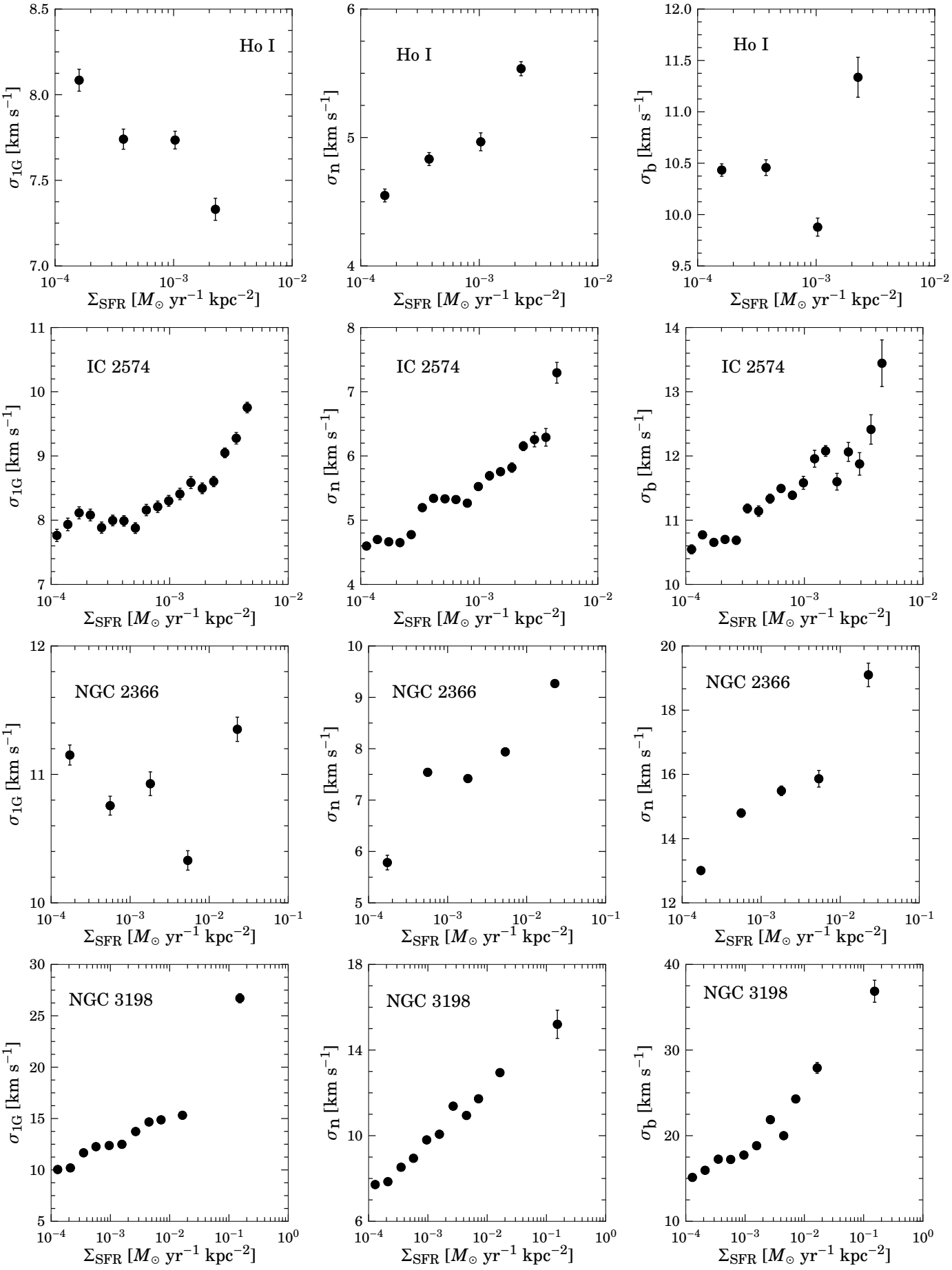

Figure 50: (Continued).

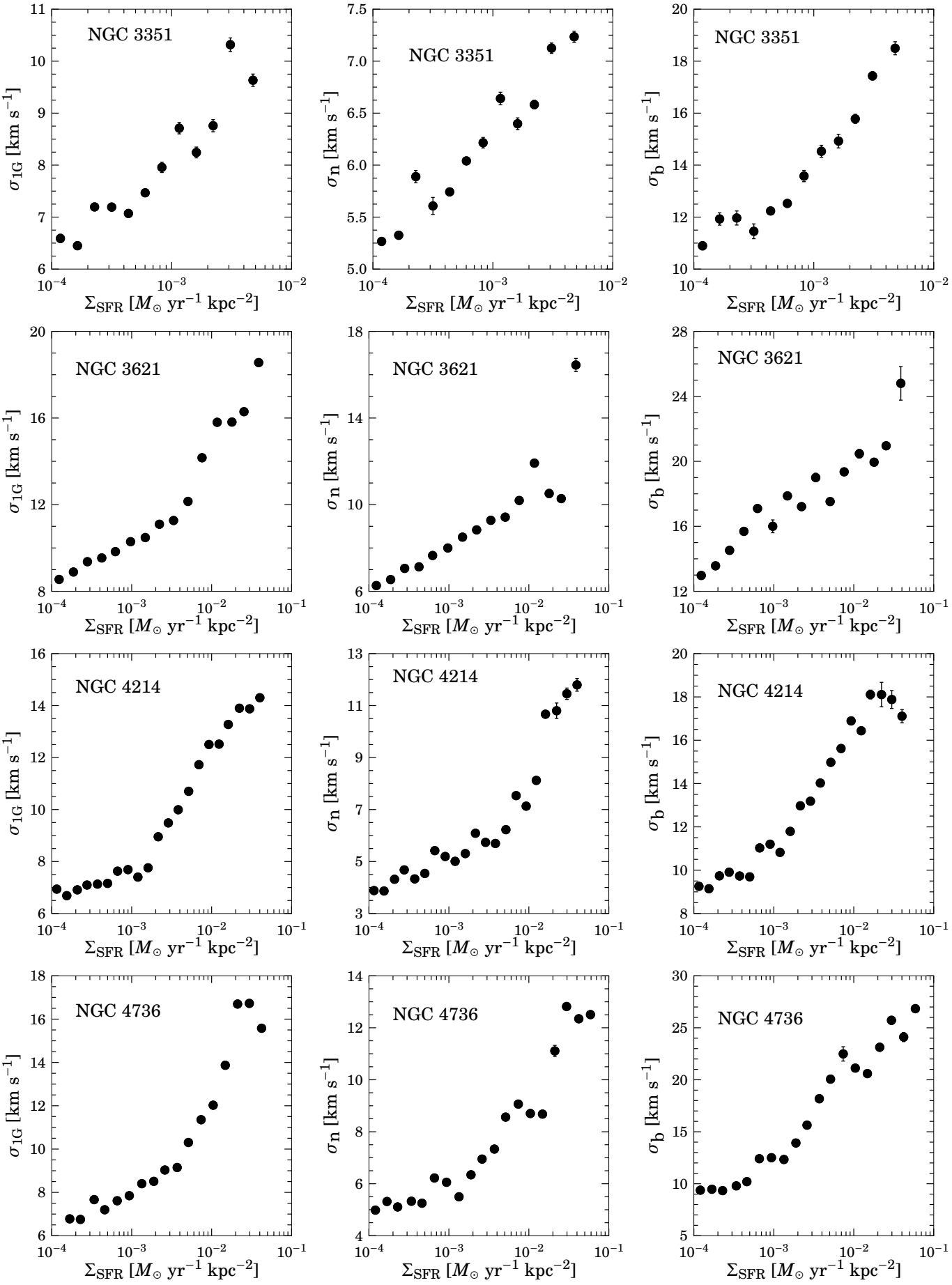

Figure 50: (Continued).

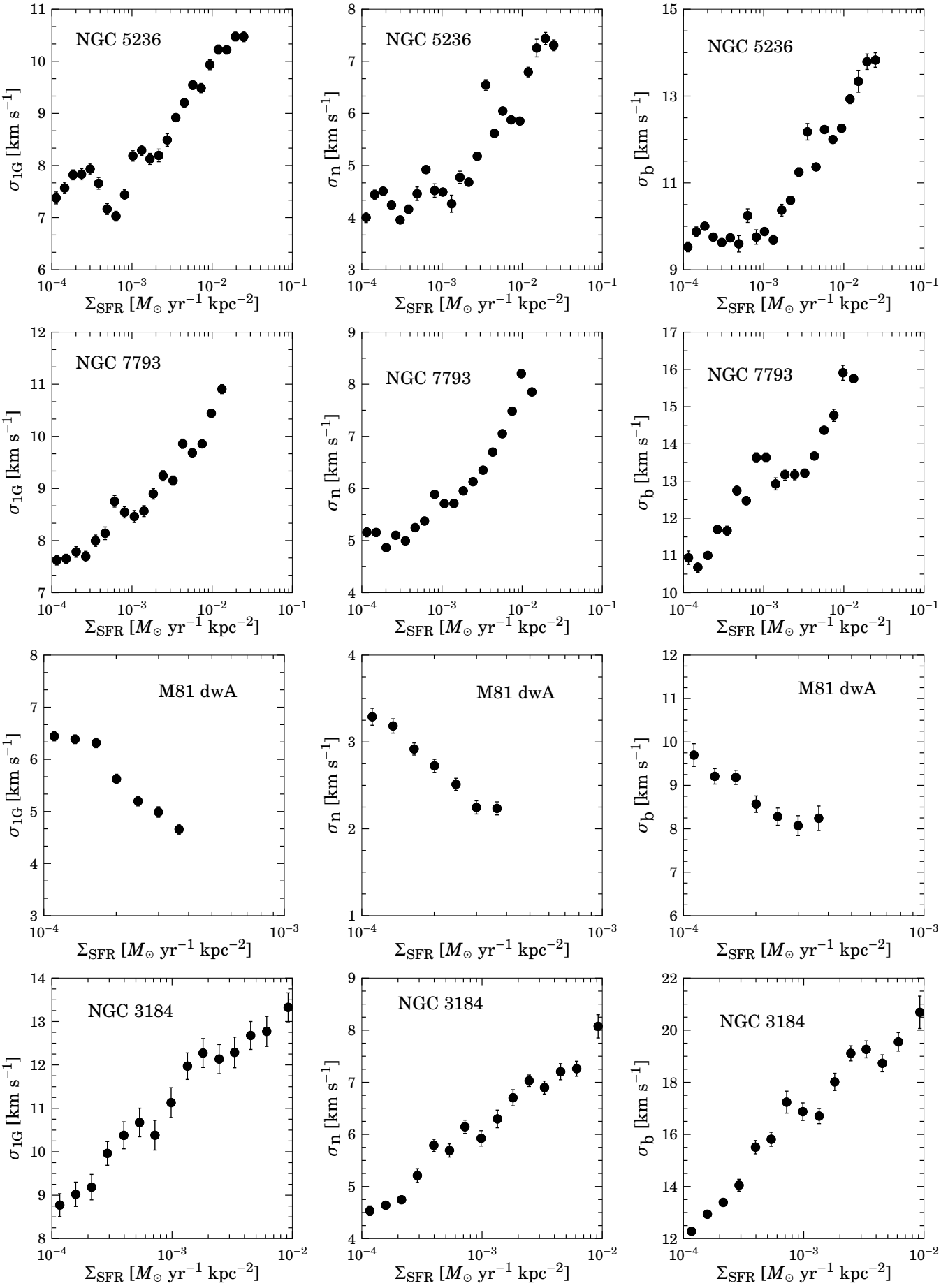

Figure 50: (Continued).

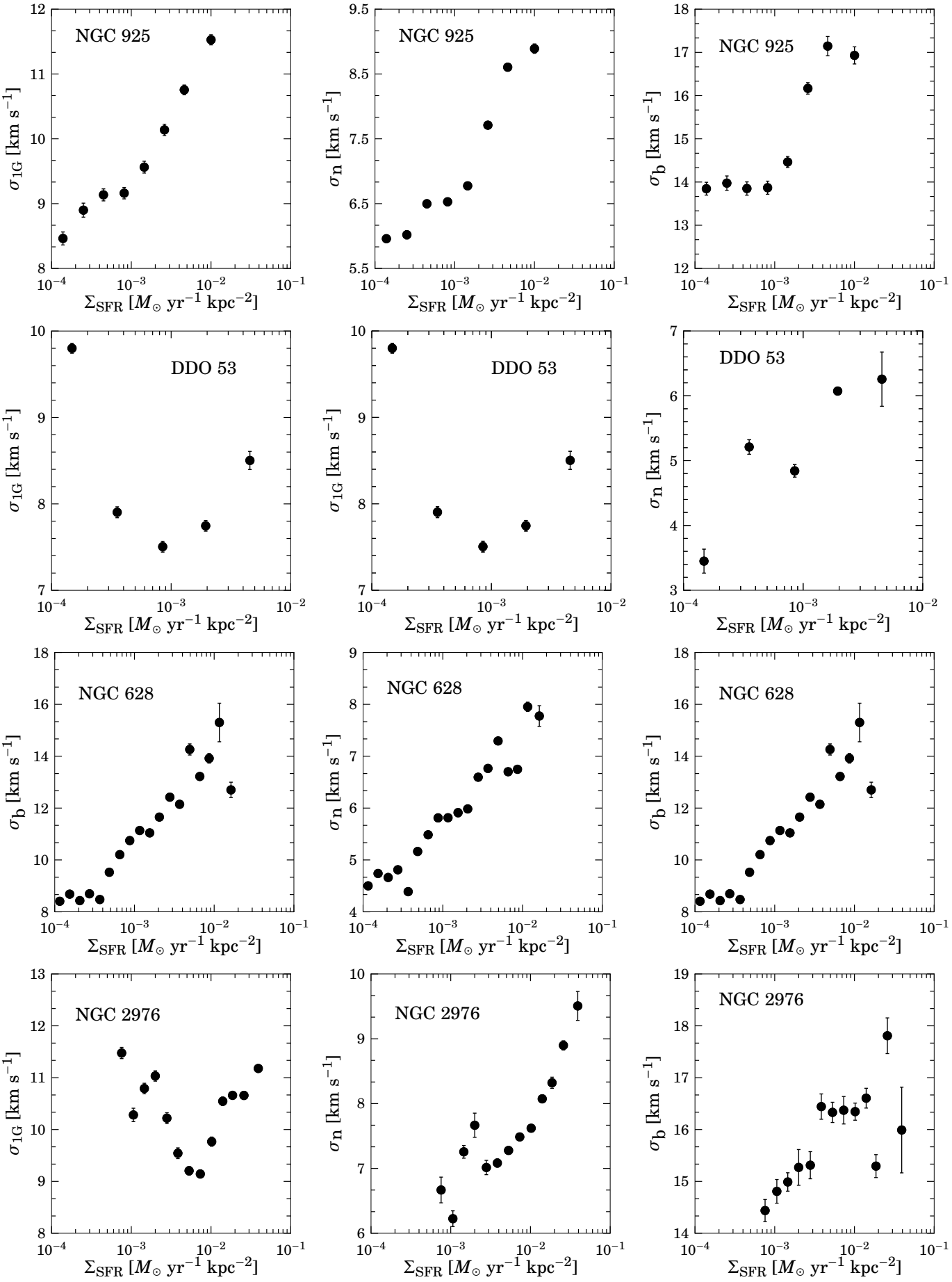

Figure 50: (Continued).

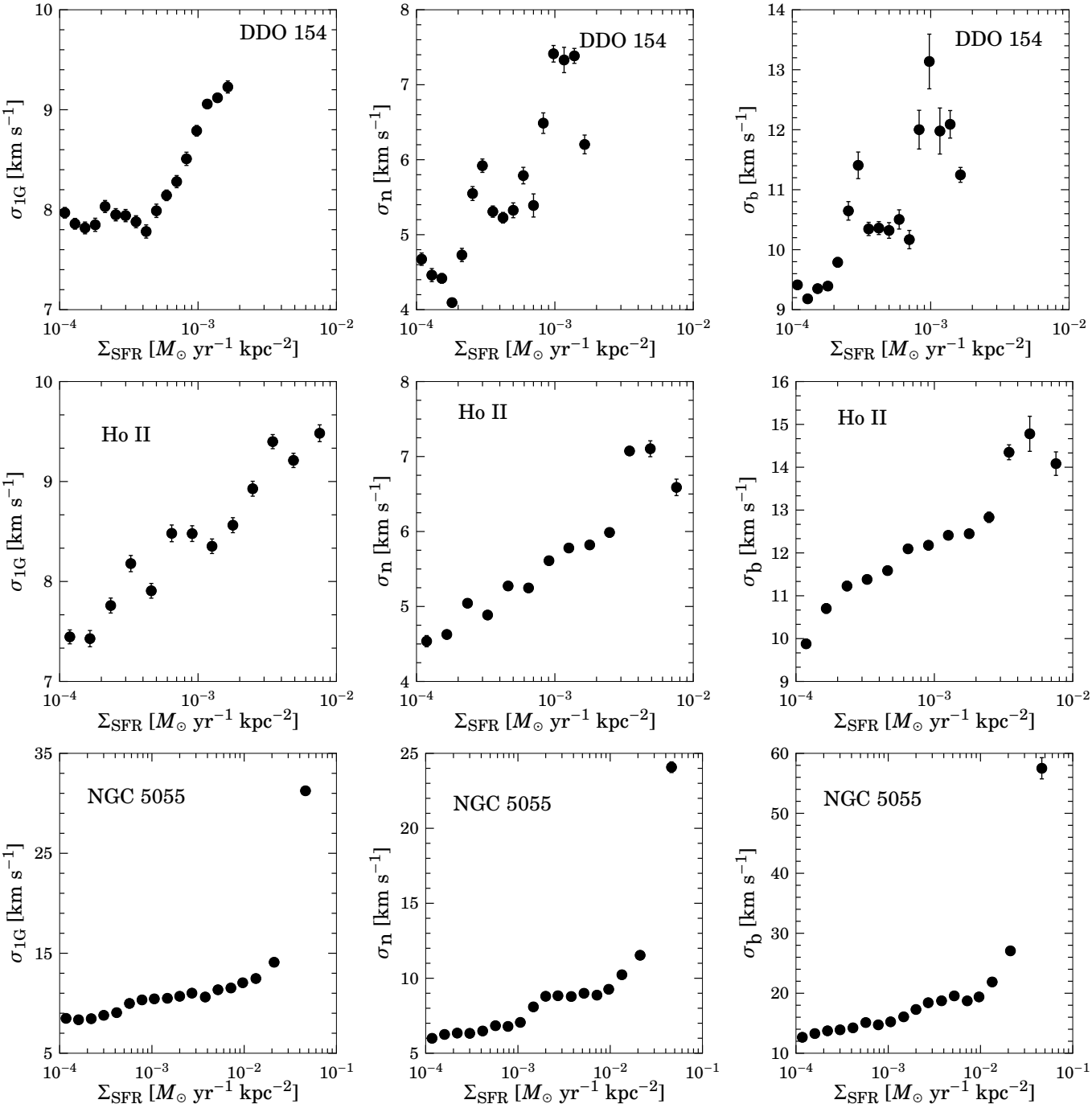

Figure 50: (Continued).

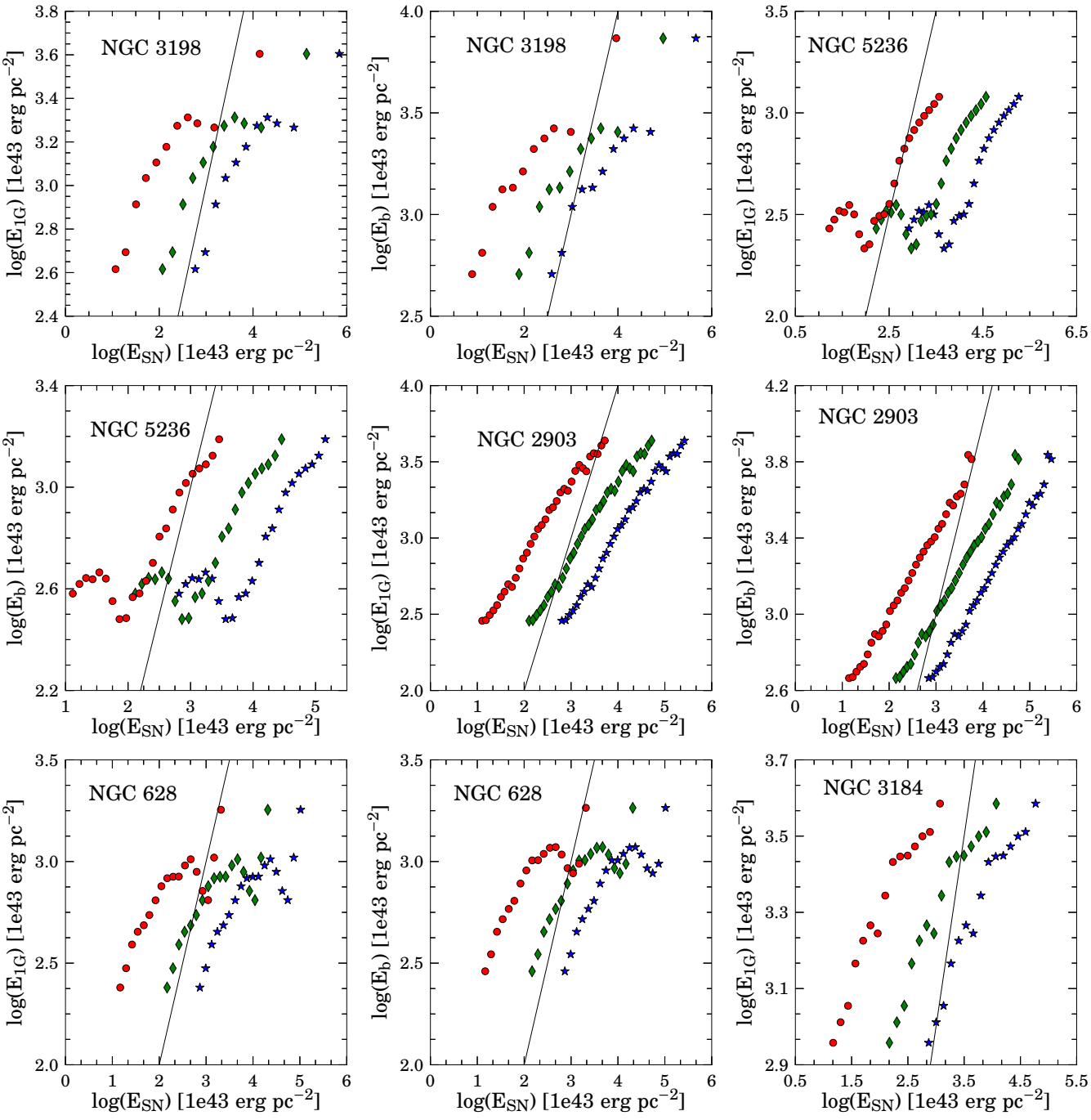

Figure 51: Turbulent HI energy as a function of supernova energy. The circle symbols represent a supernova efficiency, ε_{SN}=0.01; the diamond symbols represent ε_{SN}=0.1 and the star symbols correspond to ε_{SN}=0.5. The black solid line is a line of equality.

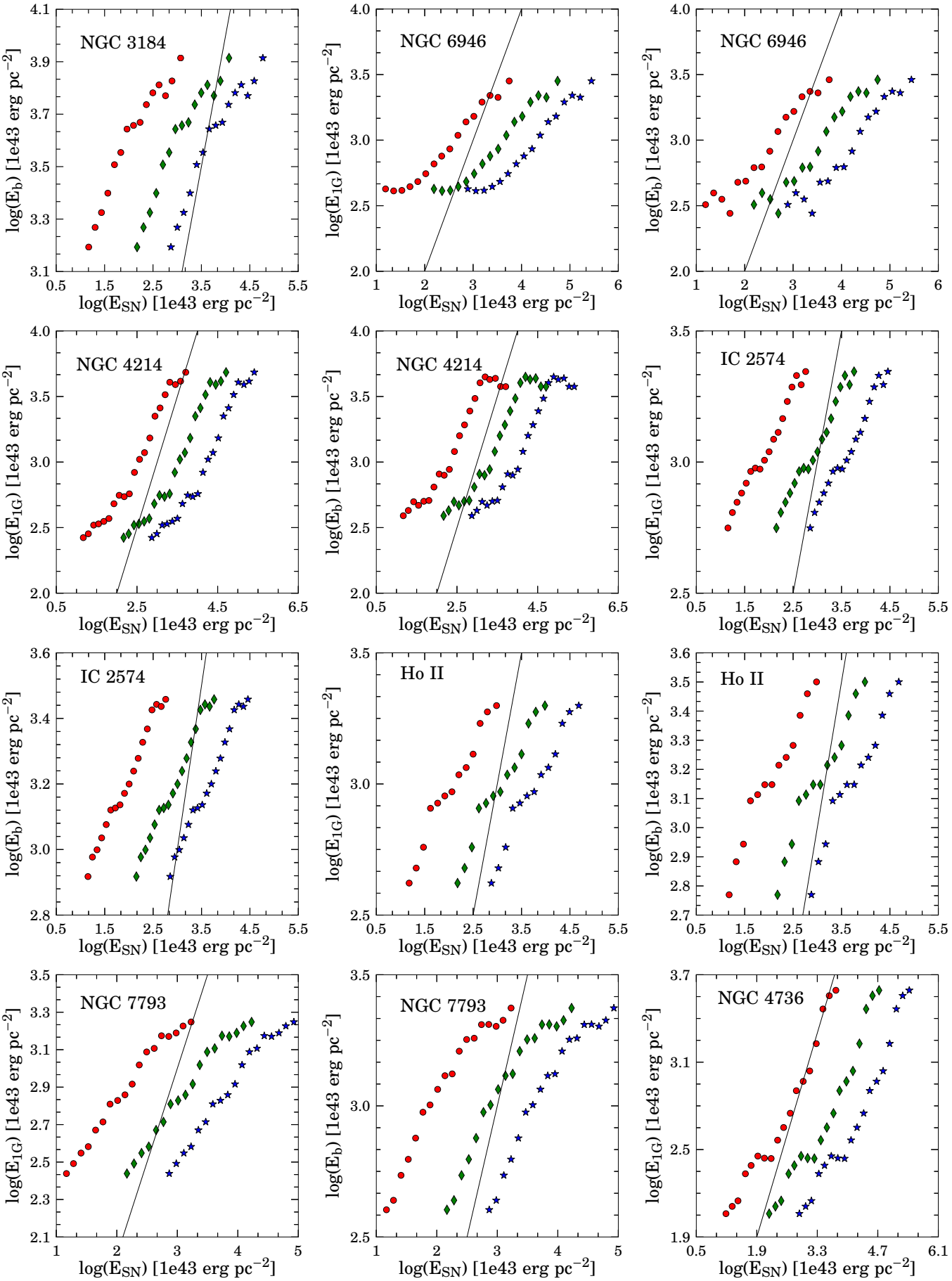

Figure 51: (Continued).

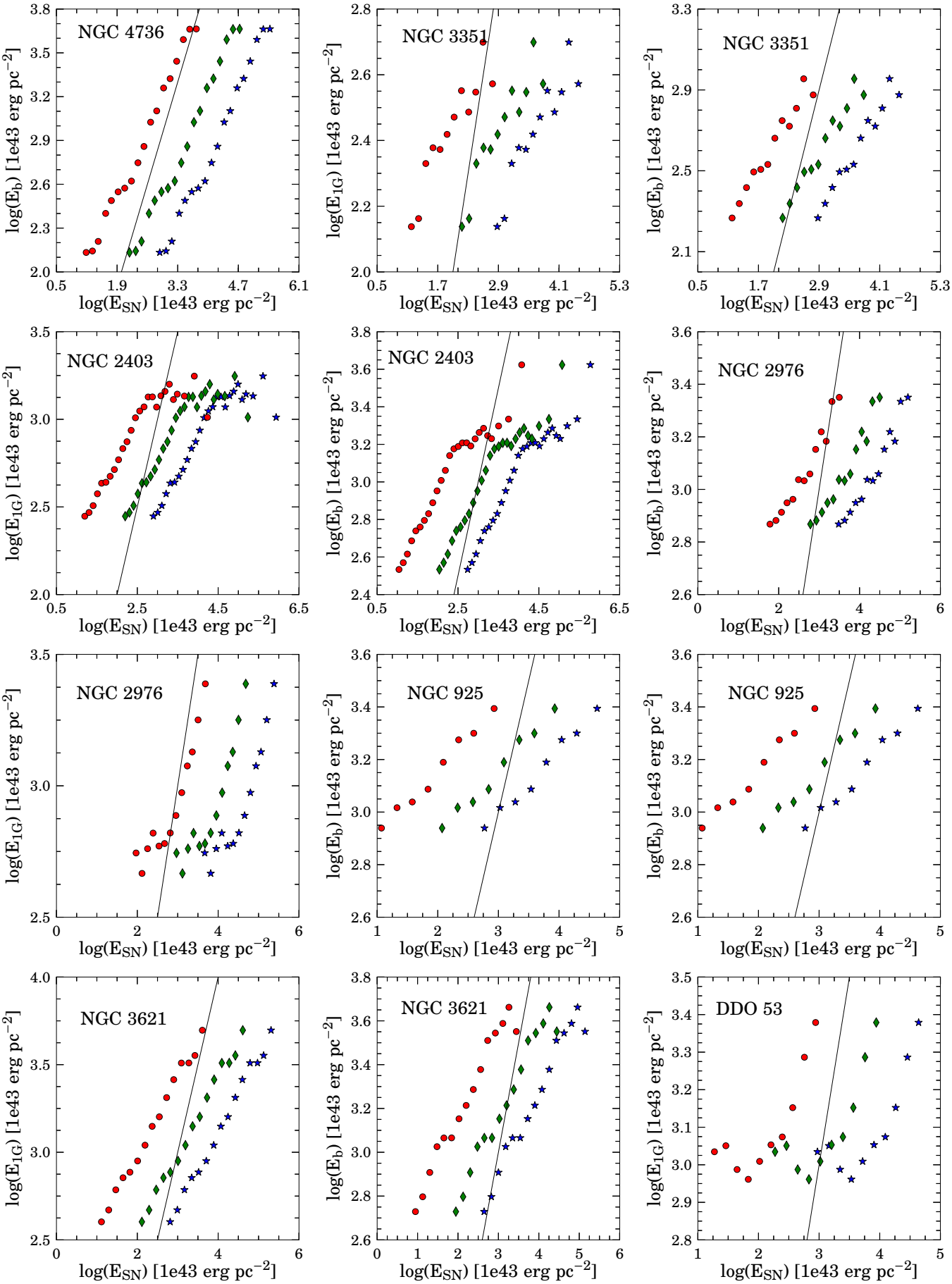

Figure 51: (Continued).

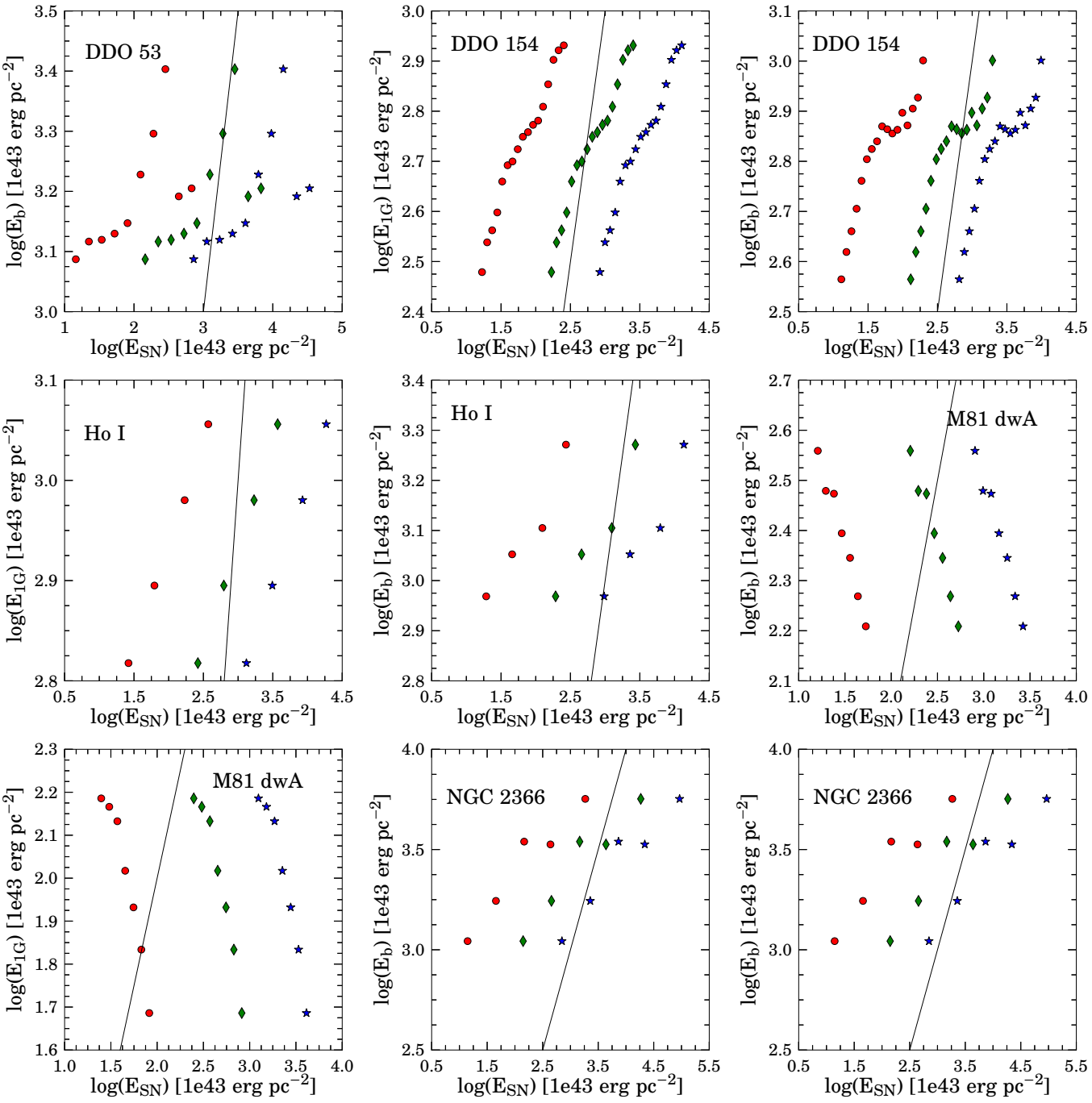

Figure 51: (Continued).

B.5 Radial profiles of turbulent HI energy, supernova energy and MRI energy

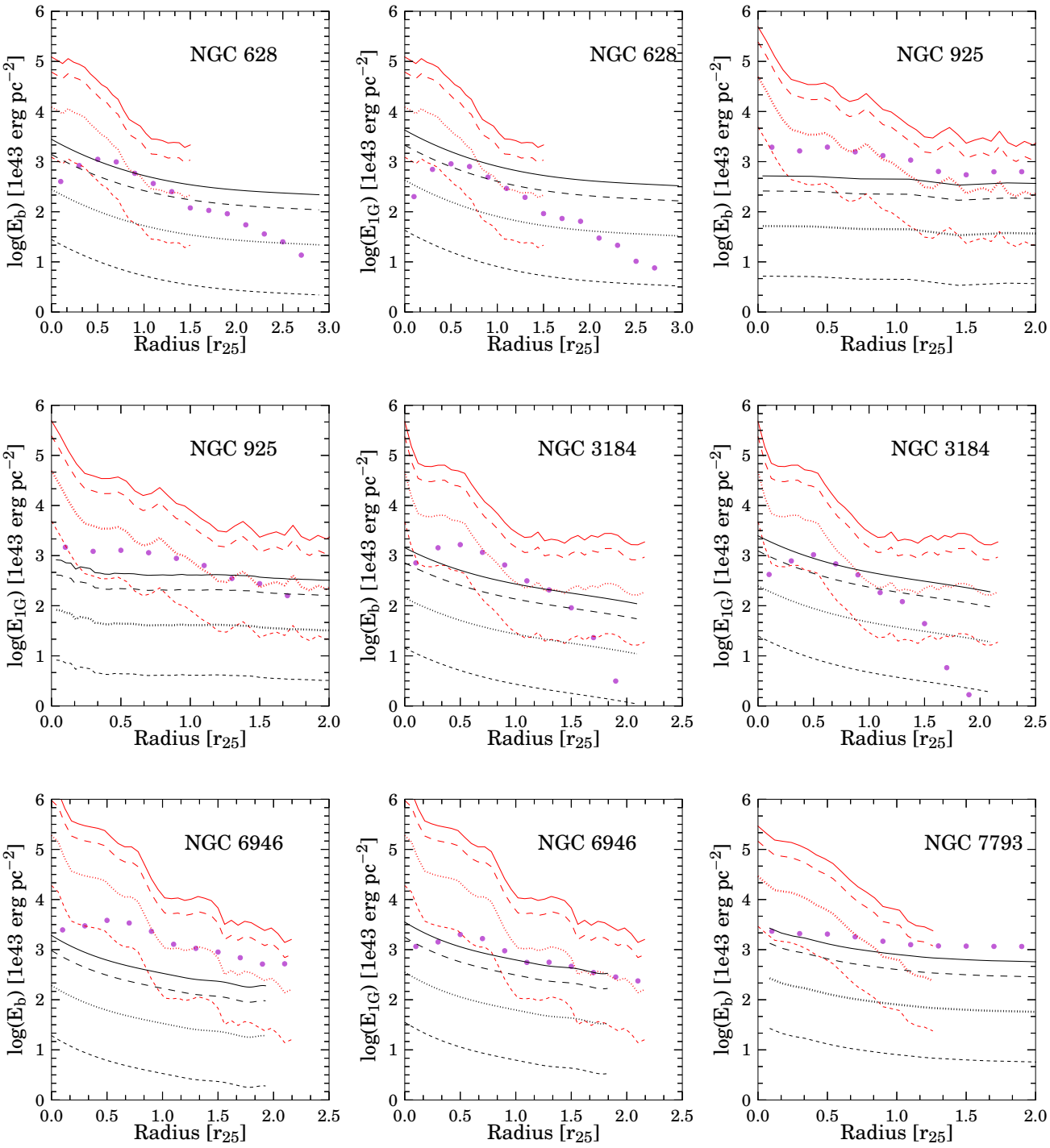

Figure 52: Comparison of turbulent energy inferred from the width of the super profiles with the turbulent energy from supernova (SN) and magneto-rotational instability (MRI). The solid circle symbols represent the turbulent energy inferred from the width of the super profiles; the black lines represent the MRI energy and the red lines represent the SN energy. The different line-styles represent different energy efficiency. The short-dashed lines represent an efficiency of 0.01; the dotted lines represent an efficiency of 0.1; the long-dashed lines represent an efficiency of 0.5 and the solid lines represent an efficiency of 1.

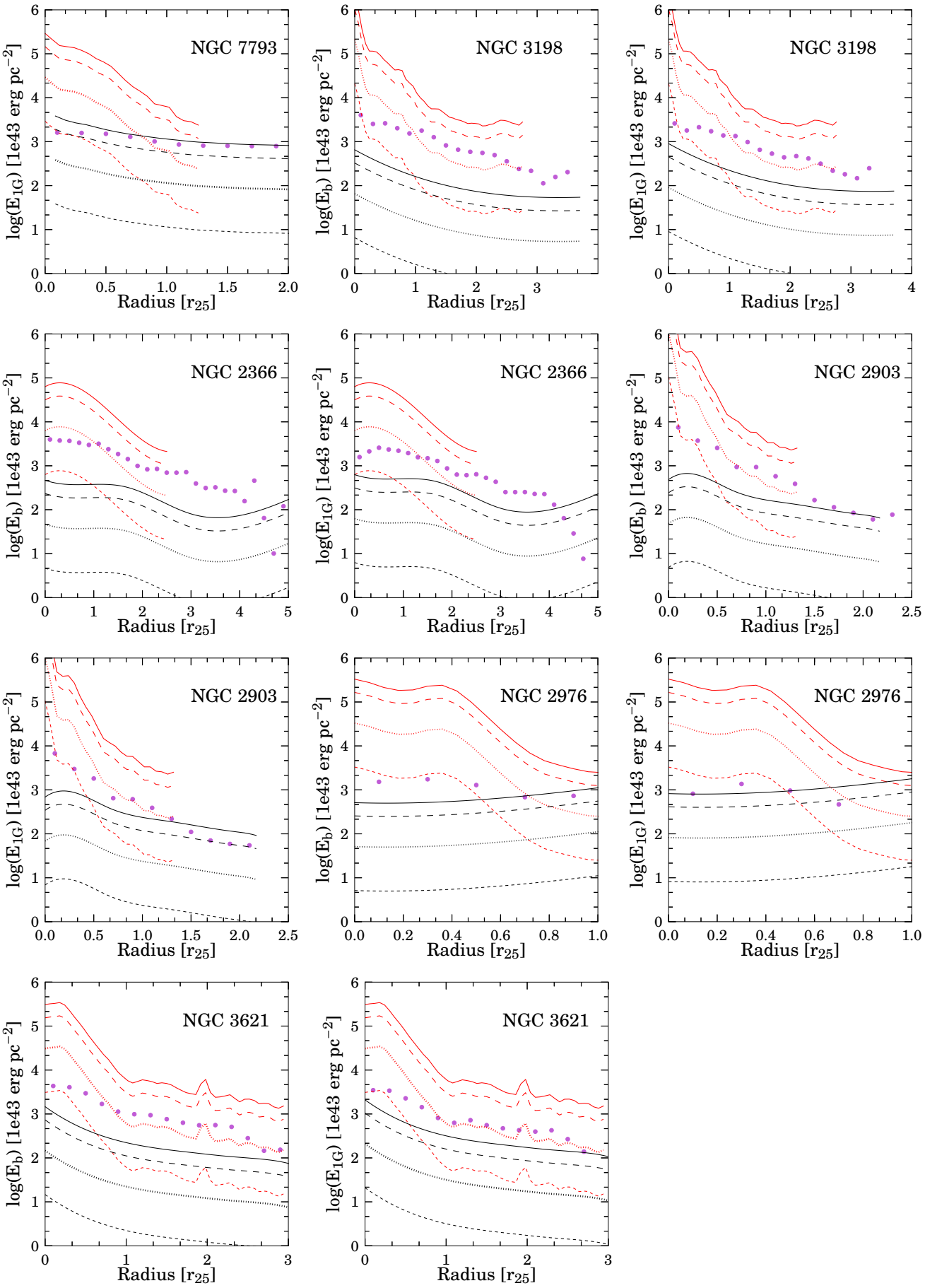

Figure 52: (Continued).

Bibliography

Bibliography

Adams, W. S. 1941, ApJ, 93, 11.

Balbus, S. A. and Hawley, J. F. 1991, ApJ, 376, 214.

Barnard, E. E. 1919, ApJ, 49, 1.

Barnes, D. G. et al. 2001, MNRAS, 322, 486.

Begum, A., Chengalur, J. N., Karachentsev, I. D., Sharina, M. E., and Kaisin, S. S. 2008, MNRAS, 386, 1667.

Begum, A., Chengalur, J. N., Karachentsev, I. D., Kaisin, S. S., and Sharina, M. E. 2006, MNRAS, 365, 1220.

Bell, M. B., Feldman, P. A., Travers, M. J., McCarthy, M. C., Gottlieb, C. A., and Thaddeus, P. 1997, ApJ, 483, 61.

Belloche, A., Garrod, R. T., Müller, H. S. P., Menten, K. M., Comito, C., and Schilke, P. 2009, A&A, 499, 215.

Bigiel, F., Leroy, A., Walter, F., Brinks, E., de Blok, W. J. G., Madore, B., and Thornley, M. D. 2008. "The Star Formation Law in Nearby Galaxies on Sub-Kpc Scales", AJ, 136, 2846.

Boomsma, R., Oosterloo, T. A., Fraternali, F., van der Hulst, J. M., and Sancisi, R. 2008, A&A, 490, 555.

Booth, R. S., de Blok, W. J. G., Jonas, J. L., and Fanaroff, B. 2009, *ArXiv e-prints*. arXiv: 0910.2935.

Bosma, A. 1981a, AJ, 86, 1791.

— 1981b, AJ, 86, 1825.

Boulanger, F. and Viallefond, F. 1992, A&A, 266, 37.

Braun, R. 1997, ApJ, 484, 637.

Caldú-Primo, A., Schruba, A., Walter, F., Leroy, A., Sandstrom, K., de Blok, W. J. G., Ianjamasimanana, R., and Mogotsi, K. M. 2013, AJ, 146, 150.

Calzetti, D. et al. 2007, ApJ, 666, 870.

Carruthers, G. R. 1970, ApJ, 161, 81.

Catinella, B., Schiminovich, D., Kauffmann, G., Fabello, S., Hummels, C., Lemonias, J., Moran, S. M., Wu, R., Cooper, A., and Wang, J. 2012, A&A, 544, 65.

Catinella, B. et al. 2010, MNRAS, 403, 683.

Catinella, B. et al. 2013, *ArXiv e-prints*. arXiv: 1308.1676.

Cazaux, S. and Spaans, M. 2004, ApJ, 611, 40.

Chung, A., van Gorkom, J. H., Kenney, J. D. P., Crowl, H., and Vollmer, B. 2009, AJ, 138, 1741.

Clark, B. G. 1965, ApJ, 142, 1398.

Dale, D. A. et al. 2009, APJ, 703, 517.

Davis Jr., L. and Greenstein, J. L. 1951, ApJ, 114, 206.

de Blok, W. J. G. and Walter, F. 2006, AJ, 131.

de Blok, W. J. G., Walter, F., Brinks, E., Trachternach, C., Oh, S.-H., and Kennicutt, Jr. R. C. 2008, AJ, 136, 2648.

Dewangan, L. K., Ojha, D. K., Anandarao, B. G., Ghosh, S. K., and Chakraborti, S. 2012, ApJ, 756, 151.

Dib, S., Bell, E., and Burkert, A. 2006, 638, 797.

Dickey, J. M., Hanson, M. M., and Helou, G. 1990, ApJ, 352, 522.

Douglas, A. E. and Herzberg, G. 1941, ApJ, 94, 381.

Draine, B. T. 2003, ARAA, 41, 241.

Drozdovsky, I. O. and Karachentsev, I. D. 2000, A&AS, 142, 425.

Duffy, A. R., Meyer, M. J., Staveley-Smith, L., Bernyk, M., Croton, D. J., Koribalski, B. S., Gerstmann, D., and Westerlund, S. 2012, MNRAS, 426, 3385.

Eddington, A. S. 1926, RSPSA, 111,424.

Elmegreen, B. G. 1995, MNRAS, 275.

Elmegreen, B. G., Rubio, M., and Hunter, D. A. 2013, Natur., 495, 487.

Fabello, S., Catinella, B., Giovanelli, R., Kauffmann, G., Haynes, M. P., Heckman, T. M., and Schiminovich, D. 2011, MNRAS, 411, 993.

Fraternali, F., van Moorsel, G., Sancisi, R., and Oosterloo, T. 2002, AJ, 123, 3124.

Freedman W. L., et al. No date, ApJ, 553, 47.

Giacconi, R., Gursky, H., Paolini, F. R., and Rossi, B. B. 1962, PhRvL, 9, 329.

Gil de Paz, A. et al. 2007, ApJS, 173, 185.

Giovanelli, R. et al. 2005, AJ, 130, 2598.

Griffiths, D. 2004. *Introduction to Quantum Mechanics*. 2nd edition. Prentice Hall. ISBN: 0131118927.

Guillard, P. et al. 2012, ApJ, 749.

Hall, J. S. and Mikesell, A. H. 1949, Science, 109, 166.

Hartmann, J. 1904, ApJ, 19, 268.

Heald, G., Józsa, G., Serra, P., Zschaechner, L., Rand, R., Fraternali, F., Oosterloo, T., Walterbos, R., Jütte, E., and Gentile, G. 2011, A&A, 526, 118.

Hiltner, W. A. 1949, ApJ, 109, 471.

Hummel, E. 1980, A&A, 89.

— 1981, A&A, 96.

Hunter, D. A., Elmegreen, B. G., and van Woerden, H. 2001, ApJ, 556, 773.

Hunter, D. A., Wilcots, E. M., van Woerden, H., Gallagher, J. S., and Kohle, S. 1998, ApJ, 495, 47.

Hunter, D. A. et al. 2012. “Little Things”, AJ, 144, 134.

Ianjamasimanana, R., de Blok, W. J. G., Walter, F., and Heald, G. H. 2012, AJ, 144, 96.

Jenkins, E. B. and Meloy, D. A. 1974, ApJ, 193, 121.

Jog, C. J. 1996, MNRAS, 278.

Jog, C. J. and Solomon, P. M. 1984, ApJ, 276.

Johnston, S. et al. 2008, Experimental Astronomy, 22, 151.

Kamphuis, J. and Briggs, F. 1992, A&A, 253, 335.

Kamphuis, J. and Sancisi, R. 1993, A&A, 273, 31.

Kanekar, N., Braun, R., and Roy, N. 2011, ApJL, 737, 33.

Karachentsev, I. D., Karachentseva, V. E., Huchtmeier, W. K., and Makarov, D. I. 2004, AJ, 127, 2031.

Karachentsev, I. D. et al. 2002, A&A, 383, 125.

Kennicutt, R. C. 1989, ApJ, 344.

Kennicutt, R. C. Jr. 1998, ApJ, 498, 541.

Kennicutt, R. C Jr. et al. 2003, PASP, 115, 928.

Kennicutt, R. C., Lee, J. C., Funes, J. G., Sakai, S., and Akiyama, S. 2008, ApJS, 178, 247.

Kennicutt, R. C., Roettiger, K. A., Keel, W. C., van der Hulst, J. M., and Hummel, E. 1987, AJ, 93.

Kerr, F. J. and Hindman, J. V. 1953, AJ, 58,218.

Kiepenheuer, K. O. 1950. “Cosmic Rays as the Source of General Galactic Radio Emission”, Phys.Rev., 79, 738.

Kobulnicky, H. A. and Kewley, L. J. 2004, ApJ, 617, 240.

Kroupa, P. 2001, MNRAS, 322, 231, pages 231–246.

Krumholz, M. R., Leroy, A. K., and McKee, C. F. 2011, ApJ, 731, 25.

Krumholz, M. R., McKee, C. F., and Tumlinson, J. 2009, ApJ, 693, 216.

Larson, R. B. 2003, RPPh, 66, 1651.

Lee, J. 2006, PhD thesis, Univ. of Arizona.

Lee, J. C. et al. 2011, ApJS, 192, 6.

Leonard D. C., et al. 2002, AJ, 124, 2490.

Leroy, A. K., Walter, F., Brinks, E., Bigiel, F., de Blok, W. J. G., Madore, B., and Thornley, M. D. 2008, AJ, 136, 2782.

Leroy, A. K. et al. 2009, AJ, 137, 4670.

Mac Low, M.-M. 1999, ApJ, 524, 169.

Mac Low, M.-M. and Klessen, R. S. 2004, Reviews of Modern Physics, 76, 125.

Macri, L. M., Stetson, P. B., Bothun, G. D., Freedman, W. L., Garnavich, P. M., Jha, S., Madore, B. F., and Richmond, M. W. 2001, ApJ, 559, 243.

Martin, C. L. and Kennicutt, Jr. R. C. 2001, ApJ, 555.

McCall, B. J. and Griffin, R. E. 2013, volume 469, 2151. Proc.R.Soc.A,.

McKellar, A. 1940, PASP, 52, 187.

Meyer, M. J. et al. 2004, MNRAS, 350, 1195.

Mouschovias, T. C. 1991, ApJ, 373, 169.

Moustakas, J. 2006, PhD thesis, Univ. of Arizona.

Moustakas, J., Kennicut, R. C., Tremonti, C. A., Dale, D. A., and Smith, J. 2010, ApJ, 190, 233.

Muãoz-Mateos, J. C. et al. 2009, ApJ, 703, 1569.

Mühle, S., Klein, U., Wilcots, E. M., and Hüttenmeister, S. 2005, AJ, 130, 524.

Muller, C.A. and Oort, J.H. 1951, Nature, 168, 357.

Myers, A. T., McKee, C. F., Cunningham, A. J., Klein, R. I., and Krumholz, M. R. 2013, ApJ, 766, 97.

Nan, R., Li, D., Jin, C., Wang, Q., Zhu, L., Zhu, W., Zhang, H., Yue, Y., and Qian, L. 2011, International Journal of Modern Physics D, 20, 989.

Oh, S.-H., de Blok, W. J. G., Walter, F., Brinks, E., and Kennicutt, R. C. 2008, AJ, 136, 2761.

Olling, R. P. 1995, AJ, 110, 591.

Oosterloo, T., Fraternali, F., and Sancisi, R. 2007, AJ, 134, 1019.

Ott, J., F., Walter, Brinks, E., D., Van Dyk S., Dirsch, B., and Klein, U. 2001, AJ, 122, 3070.

Ott, J., Stilp, A. M., Warren, S. R., Skillman, E. D., Dalcanton, J. J., Walter, F., de Blok, W. J. G., Koribalski, B., and West, A. A. 2012, AJ, 144, 123.

Parker, E. N. 1996, ApJ, 145, 811.

Petric, A. O. and Rupen, M. P. 2007, AJ, 134, 1952.

Pilyugin, L. S. and Thuan, T. X. 2005, ApJ, 631, 231.

Plaskett, J. S. and Pearce, J. A. 1930, MNRAS, 90, 243.

Price, D. J. and Bate, M. R. 2009, MNRAS, 398, 33.

Puche, D., D., Westpfahl, Brinks, E., and Roy, J. 1992, AJ, 103, 1841.

Radhakrishnan, V., Murray, J. D., Lockhart, P., and Whittle, R. P. J. 1972, ApJS, 24, 15.

Rafikov, R. R. 2001, MNRAS, 323.

Rich, J. W., de Blok, W. J. G., Cornwell, T. J., Brinks, E., Walter, F., Bagetakos, I., and Kennicutt, Jr. R. C. 2008, AJ, 136, 2897.

Rogerson, J. B., York, D. G., Drake, J. F., Jenkins, E. B., Morton, D. C., and Spitzer, L. 1973, ApJ, 181, 110.

Salim, S. et al. 2007, ApJS, 173, 267.

Sandstrom, K. M. et al. 2013, ApJ, 777, 5.

Schaye, J. 2004, ApJ, 609.

Schruba, A. et al. 2011, AJ, 142, 37.

Schruba, A. et al. 2012, AJ, 143, 138.

Schuster, K.-F. et al. 2004, A&A, 423, 1171.

Seifried, D., Banerjee, R., Klessen, R. S., Duffin, D., and Pudritz, R. E. 2011, MNRAS, 417, 1054.

Sellwood, J. A. and Balbus, S. A. 1999, ApJ, 511, 660.

Serra, P. et al. 2012, MNRAS, 422, 1835.

Shu, F. H. 1992. *The physics of astrophysics. Volume II: Gas dynamics.*

Skillman, E. D., Kennicutt, R. C., and Hodge, P. W. 1989, ApJ, 347, 875.

Solomon, P. M. and Sage, L. J. 1988, ApJ, 334.

Spitzer, L., Drake, J. F., Jenkins, E. B., Morton, D. C., Rogerson, J. B., and York, D. G. 1973, ApJ, 181, 116.

Stephan, M. E. 1877, CRAcad.Sci.Paris, 84, 64.

Sternberg, A. and Neufeld, D. A. 1999, ApJ, 516, 371.

Stilp, A. M., Dalcanton, J. J., Skillman, E., Warren, S. R., Ott, J., and Koribalski, B. 2013, ApJ, 773, 88.

Storchi-Bergmann, T., Calzetti, D., and Kinney, A. L. 1994, ApJ, 429, 572.

Swaters, R. A., Sancisi, R., and van der Hulst, J. M. 1997, ApJ, 491, 140.

Swaters, R. A., van Albada, T. S., van der Hulst, J. M., and Sancisi, R. 2002, AAP, 390, 829.

Swings, P. and Rosenfeld, L. 1937, ApJ, 86, 483.

Tamburro, D., Rix, H.-W., Leroy, A. K., Mac Low, M.-M., Walter, F., Kennicutt, R. C., Brinks, E., and de Blok, W. J. G. 2009, AJ, 137, 4424.

Tilanus, R. P. J. and Allen, R. J. 1993, A&A, 274, 707.

Toomre, A. 1964, ApJ, 139.

Trachternach, C., de Blok, W. J. G., Walter, F., Brinks, E., and Kennicutt, Jr. R. C. 2008, AJ, 136, 2720.

van der Hulst, J. M., Terlouw, J. P., Begeman, K. G., Zwitser, W., and Roelfsema, P. R. 1992. "The Groningen Image Processing SYstem, GIPSY", *Astronomical Data Analysis Software and Systems I*. Volume 25, 131. ASPC,.

van der Hulst, J. M., van Albada, T. S., and Sancisi, R. 2001, *Gas and Galaxy Evolution*. Volume 240, 451. ASPC.

van der Kruit, P. C. and Allen, R. J. 1978, ARA&A, 16, 163.

van Marle, A. J., Smith, N., Owocki, S. P., and van Veelen, B. 2010, MNRAS, 407, 2305, pages 2305–2327.

Verschuur, G. L. 1969, ApJ, 155, 155.

Wada, K., Meurer, G., and Norman, C. A. 2002, ApJ, 577, 197.

Walch, S., Wuensch, R., Burkert, A., Glover, S., and Whitworth, A. 2011, ApJ, 733, 47.

Walter, F., Brinks, E., de Blok, W. J. G., Bigiel, F., Kennicutt, Jr. R. C., Thornley, M. D., and Leroy, A. 2008, AJ, 136, 2563.

Walterbos, R. A. M. and Braun, R. 1996. "The Cool and Warm Phases of the Interstellar Medium in Spiral Galaxies", *The Minnesota Lectures on Extragalactic Neutral Hydrogen*. Volume 106, 1. Astronomical Society of the Pacific Conference Series.

Wang, B. and Silk, J. 1994, ApJ, 427.

Warner, P. J., Wright, M. C. H., and Baldwin, J. E. 1973, MNRAS, 163, 163.

Warren, S. R., Skillman, E. D., Stilp, A. M., Dalcanton, J. J., Ott, J., Walter, F., Petersen, E. A., Koribalski, B., and West, A. A. 2012, ApJ, 757, 84.

Weisberg, J. M., Cordes, J. M., Kuan, B., Devine, K. E., Green, J. T., and Backer, D. C. 2004, ApJ, 150, 317.

Wilson, R. W., Jefferts, K. B., and Penzias, A. A. 1970, ApJ, 161, 43.

Wolfinger, K., Kilborn, V. A., Koribalski, B. S., Minchin, R. F., Boyce, P. J., Disney, M. J., Lang, R. H., and Jordan, C. A. 2013, MNRAS, 428, 1790.

Wolfire, M. G., Hollenbach, D., McKee, C. F., Tielens, A. G. G. M., and Bakes, E. L. O. 1995, ApJ, 443, 152.

Wolfire, M. G., McKee, C. F., Hollenbach, D., and Tielens, A. G. G. M. 2003, ApJ, 587, 278.

Wong, O. I. et al. 2006. "The Northern HIPASS catalogue - data presentation, completeness and reliability measures", MNRAS, 371, 1855.

Xu, C., Sulentic, J. W., and Tuffs, R. 1999, ApJ, 512.

Yang, C.-C., Gruendl, R. A., Chu, Y.-H., Mac Low, M.-M., and Fukui, Y. 2007, ApJ, 671, 374.

Young, L. M., van Zee, L., Lo, K. Y., Dohm-Palmer, R. C., and Beierle, M. E. 2003, ApJ, 592, 111.

Zaritsky, D., Kennicutt, R. C. Jr., and Huchra, J. P. 1994, ApJ, 420, 87.

Zwaan, M. A. et al. 2004, MNRAS, 350, 1210.